Dissertation

submitted to the

Combined Faculties for the Natural Sciences and for Mathematics

of the Ruperto-Carola University of Heidelberg, Germany

for the degree of

Doctor of Natural Sciences

presented by

Diplom-Physicist Bernd Lang

born in: Jugenheim, Hessen

Oral examination: June 25th 2003

Initial Conditions
and Collapse of Prestellar Cores

Referees: Priv. Doz. Dr. Andreas Burkert
             Prof. Dr. Immo Appenzeller

Anfangsbedingungen und Kollaps Prästellarer Kerne

Prästellare Kerne entstehen durch die Interaktion von Gravitation und turbulenten Geschwindigkeitsfeldern. Obwohl die Turbulenz auf großen Skalen dem gravitativen Kollaps molekularer Wolken entgegenwirkt und ihn signifikant verzögert, können lokal durch konvergierende Flüsse stark verdichtete Strukturen entstehen, die durch ihre Eigengravitation gebunden sind und in diesem Sinne vom turbulenten Fluss entkoppelt sind. Dieser Mechanismus schafft somit die Anfangsbedingungen für die Entwicklung stellarer Objekte. Auf Grund der stochas-tischen Eigenschaft turbulenter Geschwindigkeitsfelder ist jeder prestellare Kern einzigartig in seiner Form und internen Dynamik. Dieser individuelle Charakter führt nach dem Kollaps auch zu individuellen Ergebnissen: Einzelsterne, Doppelsterne und Multisysteme. Das heißt, die statistischen Eigenschaften von Sternpopulationen werden wesentlich durch den individuellen Charakter der Anfangsbedingungen bestimmt. Es wurde eine Methode ent- wickelt, die die für Molekühlwolken typischen Geschwindigkeitsfelder nutzt um prästellare Kerne zu erzeugen. Zur numerischen Simulation des Gases wurde "Smoothed Particle Hydrodynamics" mit einer idealisierenden Beschreibung der erzeugten Protosterne verwendet. Die durchgeführten Sternentstehungssimulationen umfassen drei Phasen: Eine Präkollapsphase, die die Dichtestrukturen prästellarer Kerne nachbildet sowie deren Dichte- und Geschwindigkeits-Feld in ein dynamisches Gleichgewicht bringt, so dass eine natürliche und physikalisch konsistente Anfangsbedingung entsteht. In der eigentlichen Kollapsphase wurden Kontraktion und Fragmentation bis zum ersten protostellaren Objekt berechnet. In einer Postkollapsphase wurden Akkretion und Wechselwirkung der protostellaren Objekte untersucht. Ein Ensemble von 22 individuellen Simulationen wurde auf diese Weise erstellt und die resultierende Sternpopulation mit den aktuellen Beobachtungsdaten verglichen.

Initial Conditions and Collapse of Prestellar Cores

Prestellar Cores are created by the interaction of a turbulent velocity field and gravity. On large scales turbulence supports molecular clouds against gravity. But on small scales turbulence is able to create dense structures by locally converging flows. Eventually these structures may be captured by their own gravity and decouple from the turbulent flow. This mechanism creates the initial conditions for the formation of stellar objects. Due to the stochastic nature of turbulent velocity fields every prestellar core is unique in its shape and internal dynamics. This pecularity in the initial conditions is transformed via the collapse into an individuality of the resulting stellar systems: single stars, binaries and multiple systems. As a result, we expect the statistical features of stellar populations to be controlled by this peculiar properties of prestellar cores. I developed a method using the the typical turbulent velocity fields of molecular clouds to create prestellar cores. For the numeric simulations a 'Smoothed Particle Hydrodynamics' Code is used including a special simplified treatment for the created protostars. The hydrodynamical star formation simulation consists of three stages. The pre-collapse stage forms the prestellar cores and drives the velocity and density fields into dynamical equilibrium so that the resulting cores are physically consistent initial condition. During the collapse phase itself the contraction, fragmentation and heating of the gas is calculated. In the post-collapse phase accretion and the impact of interactions with other protostellar objects are analysed. In this way an ensemble of 22 individual simulations was analysed. The statistical characterisation of the resulting stellar population is consistent with the current observational data and yields a natural explanation for the second peak at the low mass end of the initial mass function.

Contents

Chapter 1

Introduction

Understanding the processes that lead to the formation of stars is one of the fundamental challenges in astronomy. It starts with the formation of molecular cloud complexes in a galaxy. The molecular clouds consists of molecular gas and dust composed of tiny grains the size of smoke particles. Even though the gas fills most of the volume of the clouds the dust is what makes them opaque. A small telescope resolves these clouds as either black regions on the sky where background stars are blocked out or as glowing nebula in the case of those clouds which had bright stars illuminating the scene e.g. the Coal Sack nebular eastward the southern cross or the nebular around the star η Carinae, see figure 1.1. Molecular clouds are the birth place of stars and the material within is the raw material from which stars are made. Since the clouds are mostly hydrogen, with some helium and trace amounts of other elements, hydrogen is what newly formed stars are principally composed of. The formation of a star begins with the formation of a self gravitating dense core out of the turbulent medium of the molecular cloud. It is about 1000 times denser than the surounding gas. This first phase of compression is mainly due to the supersonic turbulent motions driving the gas into a state where it can be captured by its own gravity. These bound structures are called *prestellar cores* and they are the direct progenitors of stars. Chapter 2 gives an overview of the star formation process, about the features of molecular clouds and a detailed observational characterization of prestellar cores. Chapter 5 then focuses on the transition of a turbulent, unbound gas region towards a bound structure. It analyses in detail how a self gravitating center is created out of a turbulent molecular gas environment. It is shown that this early compression phase is significantly different to the standard picture of an isothermal collapse phase and worth to be exposed as an additional independent phase of star formation. Once the absolute magnitude of gravitational energy exceeds the sum of thermal, turbulent, magnetic and rotational energy the collapse starts and proceeds until the central density and temperature exceed the threshold for nuclear fusion. This new energy source supports the gas against gravity and leads to an equilibrium state: a protostar is born. It is still embedded in a parental gaseous envelope which continues to collapse into the center. But conservation of angular momentum prevents the gas from falling directly towards the central object. Instead, it forms a rotationally supported disk and matter is able to reach the central object only after the removal of angular momentum through viscous transport or disk instabilities. In Chapter 3, I discuss the special features of the numerical modelling allowing the simulations to evolve far beyond the first star formation event. In Chapter 6 accretion histories and the formation mechanisms of single, binary and multiple stars are analysed in detail. Because

the formation of individual stars is subject to highly undeterministic statistical events the existence of a deductive theory is highly unlikely. However, we may be able to understand the star formation process from a statistical point of view, in terms of the mass spectrum, binary fraction, orbital parameters etc. of the resulting stellar systems. Therefore we have designed an ensemble of individual prestellar cores as initial conditions and performed the full collapse calculation for each realization plus the follow up calculation for the accretion phase after the first stellar object has formed. A detailed analysis of the resulting stellar systems is given in Chapter 6 and compared to the results from observations.
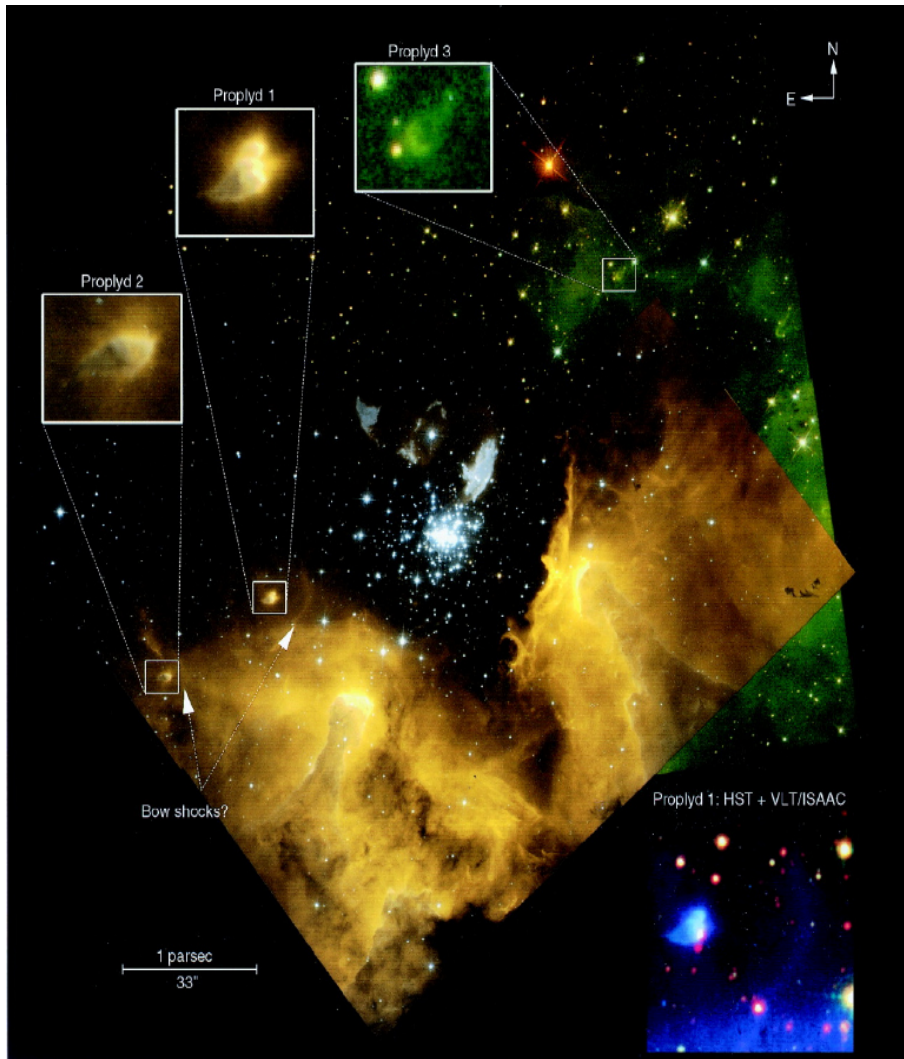
Figure 1.1: **Active star formation region in the η Carinae nebula. The stellar winds of a young cluster has blown a cavity into the surrounding molecular cloud. Above the cluster one sees a massive star which has allready expelled its outer shell seen as dumbbell shaped nebula. The three zoomed cut outs showing the dense envelope of young embedded protostars.**

Chapter 2

Observations and Models

2.1 The Different Stages of Star Formation

A theoretical point of view

The theoretical point of view is focused on the physical processes involved and how they influence or control the evolution of the contracting gas cloud. The classification in different collapse phases is motivated by the fact that there is no single self similar solution for the collapse from the prestellar core down to stellar densities. It's rather a cascade of distinct compression phases with a special type of physics going on controlling the scene.

turbulent compression phase: The formation of a star begins with the formation of self gravitating prestellar core out of the unbound turbulent gas of the molecular cloud. This first phase of compression is done by the ubiquitous supersonic turbulent velocity field driving the gas locally into a state where it can be captured by its own gravity. Prestellar cores preferently along the intersection lines of shock fronts, regions with more extended but still strong velocity gradient or in regions with extended converging flows.

isothermal collapse phase: For densities below $\rho < 5.0 \times 10^{-13} \, \text{g/cm}^3$ the mean free path of photons is much larger than the size of the prestellar core. So that the radiative cooling process is much faster than the heating by gravitational contraction. Therefore the temperature of the cloud and its fragments stays roughly constant.

adiabatic molecular collapse phase: For $\rho > 5.0 \times 10^{-13} \, \text{g/cm}^3$ the mean free paths of photons becomes shorter than the typical size of a fragment. This is called the 'opacity limit' due to the fact that at this density a typical fragment becomes opaque or optically thick resulting in a cooling timescale larger than the local free fall time. Therefor the fragment will behaves like adiabatic compressed molecular gas. The gas starts to heats up and the thermal pressure decelerates the collapse significantly. Resulting in the formation of slowly contracting hydrostatic cores which are accreeting isothermal low density gas from its envelope. This works up to the point where the molecules start to dissociate.

second collapse phase: After the gas has being compressed adiabatically over five orders of magnitude the central temperature exceeds about 2000 K and the hydrogen molecules

start dissociate. This process consumes a huge amount of thermal energy and further compression leads only to a weak increase in temperature. The pressure support can't compete with the ever growing gravitational forces. As a result the dissociation process allows for a second collapse phase and eventually further fragmentation. Energy is consumed now by the dissociation process resulting in a decreasing pressure support. This allows for a second collapse phase and eventually further fragmentation. This second collapse phase allows for an additional compression of the gas of about 4 orders o magnitude in density.

adiabatic atomic collapse phase: After all molecules were transformed into atomic gas the density reaches about 1.0×10^{-3} g/cm^3. Now the core behaves adiabatically again, but with a significantly higher adiabatic coefficient than for the molecular gas. This is because all the energy gain from the gravitational field is transformed into kinetic energy of the atoms, respective into thermal pressure. As a result the temperature increases again and a second hydrostatic core forms. As this core rapidly accretes material from the second collapse phase it's center is easily pushed towards stellar densities and nuclear fusion can ignite.

An observational point of view

An observer describes the star formation process in terms of how the object will appear on the sky. So the observational classification is based on the spectral energy distribution of the pre- or protostellar objects. A part of the young stellar objects radiation is absorbed and reprocessed depending on how much matter is hosted in the star's circumstellar disk and envelope. As a result a part of the stars energy will be shifted towards the infrared, far infrared and submm range depending on how the matter is distributed around the evolving star . Therefore the spectral energy distribution becomes an excellent indicator for the evolutionary state of the object, see figure 2.1

prestellar core: An 0.05   . . . 0.2 pc extended region can be detected by line emission of molecules, see figure 2.2. Estimated column densities are 100 times larger compared to the local environment and in the order of 10^{23} cm^{-2}. There is no central object detectable.

class 0: At this stage a central object has formed but is still low in mass. This stellar embryo is only a few ten thousand of years old. Most of the material that will eventually make up the star is still quite far from the core and is very cool $(10 - 20\,\text{K})$, producing emission only at millimeter wavelengths or in the far infrared, see figure 2.3.

class I: The protostar becomes visible in infrared, see figure 2.4 and is about 10^5 years old. There is still an significant amount of matter in the circumstellar envelope. Therefore the envelope is opaque to optical light and thus protostars are generally invisible to ordinary telescopes. Most of what we know about protostars comes from observations at infrared and millimeter wavelengths. The infrared emission from the disk and the envelope is dominated by the cooler material in the envelope. A few protostars have also been observed at X-ray wavelengths. X-ray emission may be an important source of ionization, allowing the star, disk and outflow to be coupled by magnetic fields. Such magnetic fields may also be responsible for squeezing the outflow, producing jets.

<u>class II:</u> The protostar star becomes visible in the optical (figure 2.5), and is known as a Classical T Tauri star. Classical T Tauri stars are about 1-10 million years old and are easily identified by their strong emission lines produced by the disk/star interaction. The infrared emission is dominated by the disk, since the envelope has mostly dissipated. Classical T Tauri stars are strong X-ray emitters and can also produce powerful winds.

<u>class III:</u> Once the circumstallar disk has dissipated enough so that it no longer interacts with the star, the emission lines are no longer present or very weak. Therefore the objects are called "Weak-lined" T Tauri stars. Weak-lined T Tauri stars are primarily found because they are bright X-ray sources. T Tauri stars produce X-rays in hot plasma trapped in magnetic fields above the stellar surface. This is similar to the process in which the Sun produces bright flares but 100-1000 times more powerful. X-ray imaging satellites, such as EINSTEIN, ROSAT and ASCA have discovered hundreds of Weak-lined T Tauri stars.
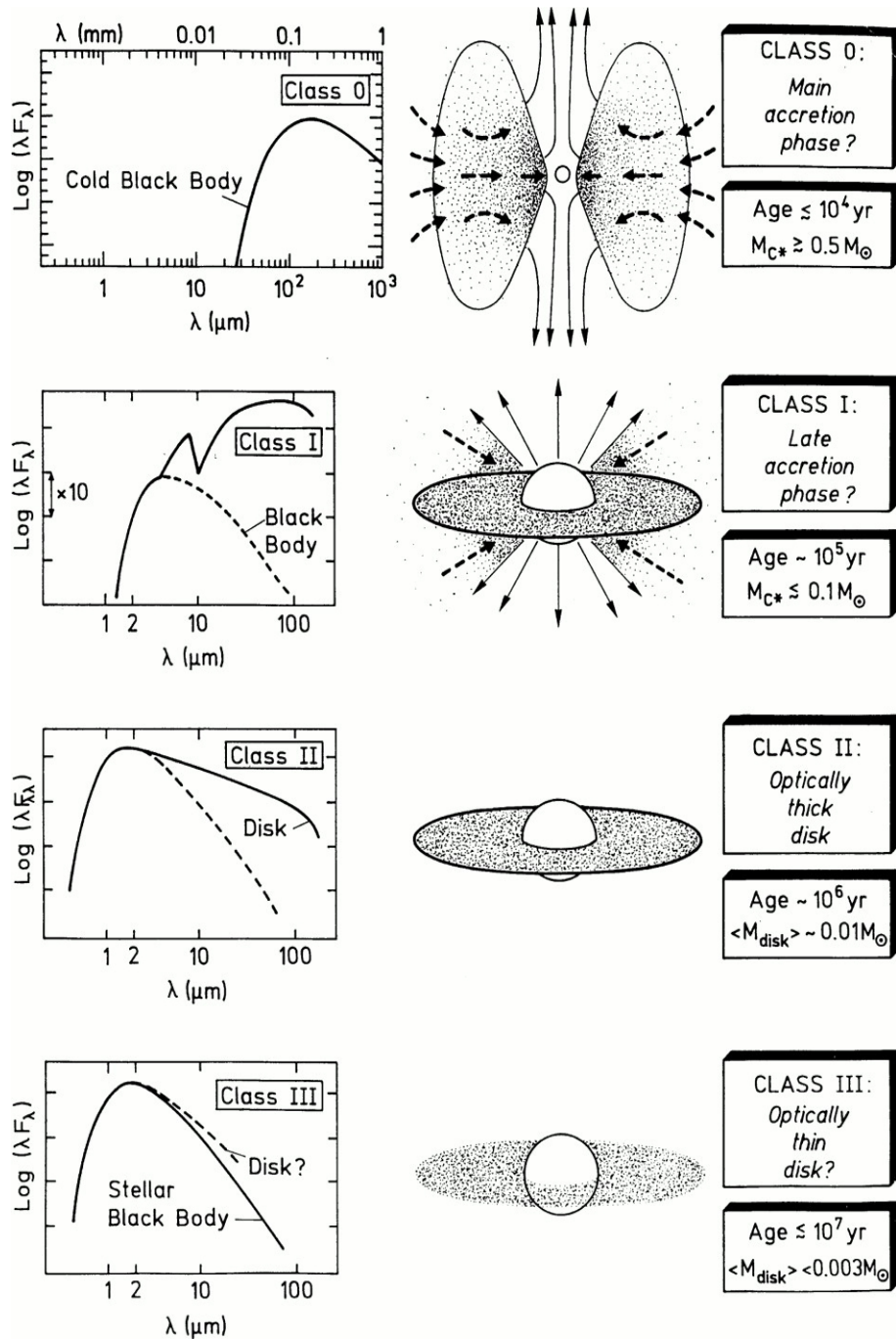
Figure 2.1: **Different stages of the star formation process and the expected spectral energy distribution as suggested by Andre and Montmerle (1994)**
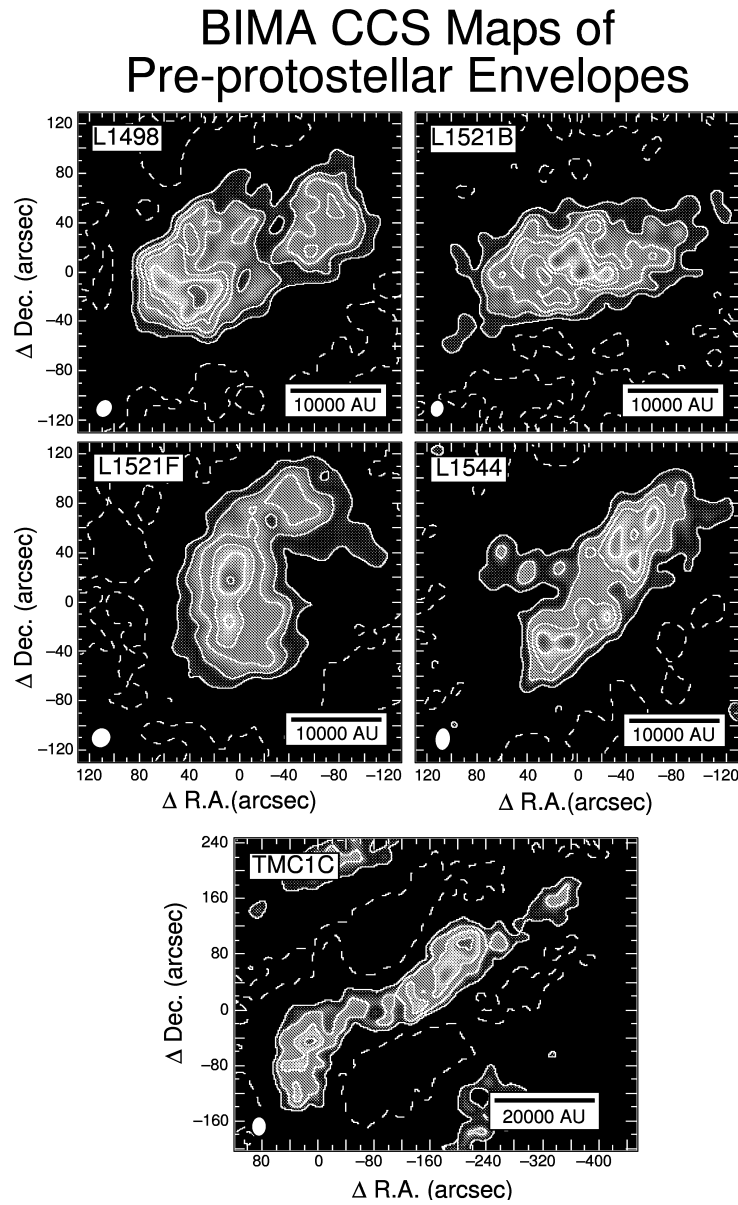
Figure 2.2: **Radio line observations of prestellar cores in CCS** $J_N = 3_2 - 2_1 (\lambda = 8.9mm)$. **Done with the Berkeley Illinois Maryland Array by Ohashi (1999)**

Figure 2.3: $C^{18}O$ total intensity maps of protostellar envelopes in Taurus. They are classified as class 0 (upper row) and class I objects (middle and lower row). The contour spacing is 2σ, starting at $\pm 2\sigma$. Crosses show the positions of the central sources while arrows show the directions of the associated outflows. Taken from Ohashi (1999)
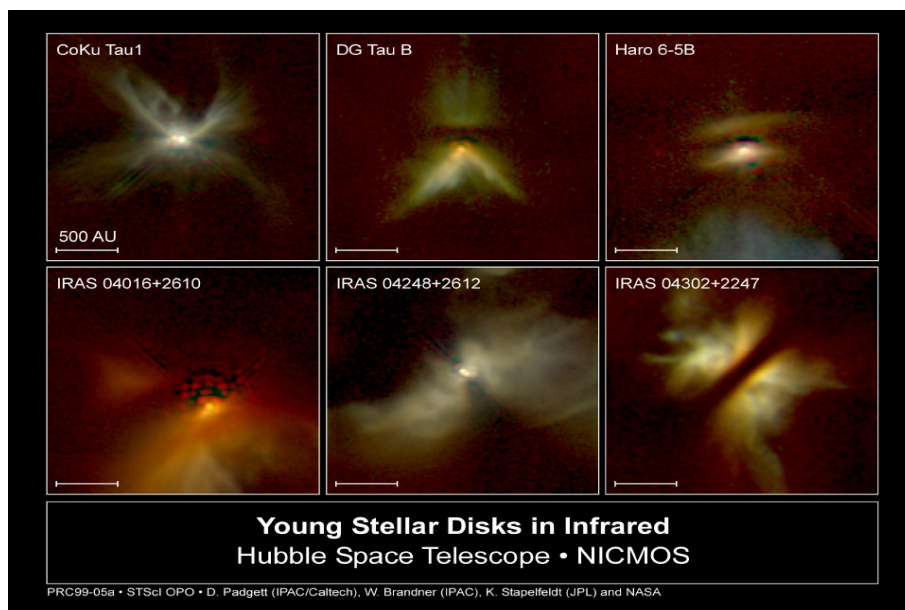
Figure 2.4: **Class I objects: Young Protostars still invisible in the optical as seen with the Near Infrared Camera Multi Object Spectrograph (NICMOS) of the Hubble Space Telescope. The sensitivity of NICMOS range from 0.8 to 2.5 microns.**
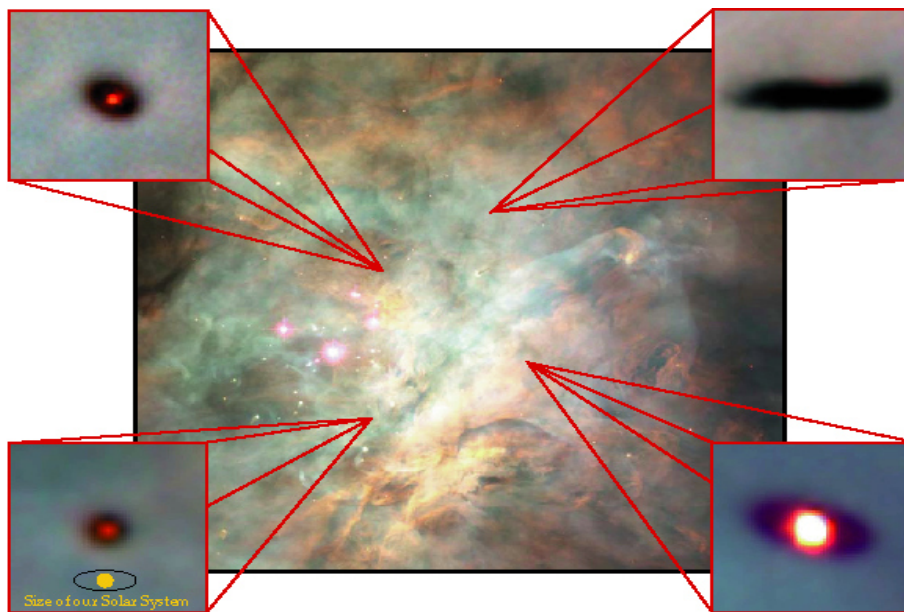
Figure 2.5: **Class II objects: Protostars just becoming visible in the optical. Here, in the lucky case of a bright background nebular also the massive disks around the Protostars are visible. The image shows the Trapezium Cluster in the Orion Nebular. The image was taken with the Wide Field Planetary Camera (WFPC) of the Hubble Space Telescope. The sensitivity of WFPC range from 0.17 to 0.85 microns**

2.2 Distribution of Molecular Gas in our Galaxy

All actual star formation takes place in dense molecular clouds and bok globules distributed along the spiral arms of our galaxy. Molecular clouds result from the compression of atomic gas entering the spiral arms. Figure 2.6 shows the Milky Way as observed in the 115 GHz line of carbon monoxide (CO), the best tracer of interstellar molecular clouds. These clouds are composed almost entirely of molecular hydrogen and atomic helium, both nearly impossible to detect.

In the top map the colors, from dark blue (weakest) to white (strongest), represent the CO line intensity summed up over all radial velocities, a measure of the total amount of molecular gas along the line of sight. The intense yellow-to-white horizontal strip at the center of the map is produced by the large number of molecular clouds in the inner spiral arms of the Galaxy, while elsewhere in the map individual nearby molecular clouds are prominent. The map shows impressively that the dense molecular gas is confined to a very narrow plane embedded in the galactic disk. The lower graphic shows a zoom out of a region around Perseus. Here the colors range from black (low intensity) to white (strong intensity). The conspicuous white structures to the right hand side are typical giant molecular clouds.

2.3 Properties of Molecular Clouds

Dense molecular clouds with active star formation are generally self-gravitating, magnetized, turbulent compressible fluids. They have sizes of about $10 - 30 \, \text{pc}$, densities of about 100 molecules per ccm and masses of $10^4 \quad \ldots 10^6 \, \text{M}_\odot$. Typical measured columndenisties are in the order of $10^{21} \quad \ldots 10^{22} \, \text{cm}^{-2}$. The clouds are opaque for ultra violette radiation and become translucent in the far infrared and radio band. So they cool down to temperatures of $10 \quad \ldots 20 \, \text{K}$.

2.3.1 Ingrediences

The chemical composition is dominated by molecular hydrogen and helium. Because the interstellar gas has been extensively reprocessed by stars and supernovae it is enriched which heavier elements like carbon, nitrogen, oxygen etc. A part of the heavy elements condenses into small dust grains. Then there are two main components of molecular clouds: gas and dust composed of tiny grains the size of smoke particles. The dust to gas mass ratio is of the order of 1:100. Even though the resulting dust to gas volume filling factor is 1:100000 the dust absorption dominates especially on short wavelengths. As a result molecular clouds are effectively shielded from ionizing UV photons to a large extend so that the degree of ionization is very low and in the order of $10^{-6} \ldots 10^{-8}$ (Bergin et al. (1999))

2.3.2 Structure

Molecular Clouds are built up of an hierarchical selfsimilar fractal like structure from large fragments to more and more small sub- and subsubfragments. This causes them to have a very high surface area which is important for several exchange processes with the diluted atomic or ionized gas in which they are embedded. At the end of this chain from large to small scales are the clumps and prestellar cores. Clumps and prestellar cores are the only gravitationally bound structures in molecular clouds. Clumps are massive ($M \sim 1000 \, \text{M}_\odot$)
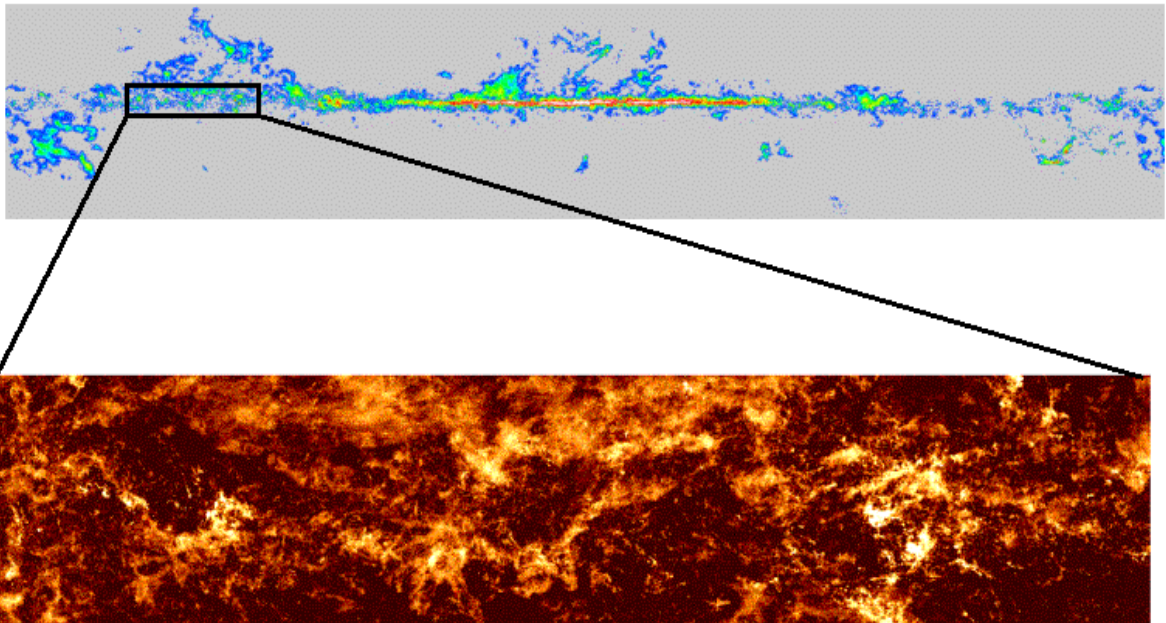
Figure 2.6: **Upper figure: The Milky Way as observed in the 115 GHz line of CO. Colors range from dark blue (weakest) to white (strongest), giving a measure of the total amount of molecular gas along the line of sight. Prepared by Dr. Tom Dame, Dr. Dap Hartmann and Prof. Patrick Thaddeus of the Center for Astrophysics. Lower figure: CO map of the 'Canadian Galactic Plane' survey covering an area of 40×8.5 degrees. Colors rage from black (low intensity) to white (strong intensity).**

accumulations of molecular gas about 100 times denser than the mean density of molecular clouds. Star forming clumps form star clusters. Even though clumps are bound structures the resulting star clusters are most times unbound at the end.

Figure 2.7 shows the detailed structure of a molecular cloud complex seen close to the tail of Scorpion. Inside this molecular cloud complex Motte et al. (1998) has found more that 40 dense prestellar cores.

2.3.3 Velocity Structure and Scaling Relations

The highly supersonic linewidths that are observed in molecular clouds probably imply turbulent motions. The turbulent motions are naturally expected to built up the fractal structures (Mandelbrot 1982). This means that molecular clouds are not static. Their fractal structure gets reprocessed at every time. This permanent rearrangement of mass efficiently prevents the molecular cloud from collapse and acts like an additional pressure. The fact that molecular clouds are supported not only by thermal pressure can also be seen from the observation that the star formation rate in our galaxy is very low. An order of magnitude estimation for the star formation rate based on the assumption that all the gas condensed in molecular clouds would collapse on their free fall time ($\sim 4 \times 10^6$ yrs) and transform into stars yields a value about 100 times larger than what is observed (Scalo 1986; Evans 1999). Even if we assume a more realistic star formation efficiency of 10 percent the life times of molecular clouds are still an order of magnitude larger than their free fall times. So its clear that the turbulence significantly controls the star formation, and it will come out in chapter 5 that it also plays a fundamental role in the star formation process itself. The turbulent velocity fields were extensively measured during the last three decades. One of the most interesting features is the linewidth-size correlation discovered by Larson (1969). It connects the turbulent line broadening to the size of the observed region:

$$\sigma[\text{km/s}] = 1.1 \, \text{L[pc]}^{\,0.38} \tag{2.1}$$

As the linewidths approach their thermal values on size scales of about $0.1 \, \text{pc}$, structures depart from self similar description. This departure may mark the boundary between cloud evolution and star formation. In the central regions of prestellar cores (as they can be resolved by radio or submm telescopes/arrays) the turbulent linewidths seem to be constant and in the order of $\sigma = 0.7 \, c_s$ (Goodman et al. (1998)). The linewidth-size relation obeyed by the giant molecular clouds ends with a maximum velocity dispersions of $\sigma_{cl} \sim 3 \quad \ldots 5 \, \text{km/s}$. This exceeds the thermal sound speed by a factor of 20. Such supersonic turbulence would dissipate on the crossing timescale of the molecular cloud:

$$t_{tc} = \frac{R_{cl}}{\sigma_{cl}} \quad = \quad 10^7 \, \text{yrs} \tag{2.2}$$

So there is the need of an efficient driving mechanism for the turbulence. Possible candidates are supernovas and stellar winds, the galactic sheer and magnetic fields.

2.4 Prestellar Cores

Prestellar cores are the smallest structures of molecular clouds. They are the final stage of cloud fragmentation and the source for intermediate and low mass star formation. Their
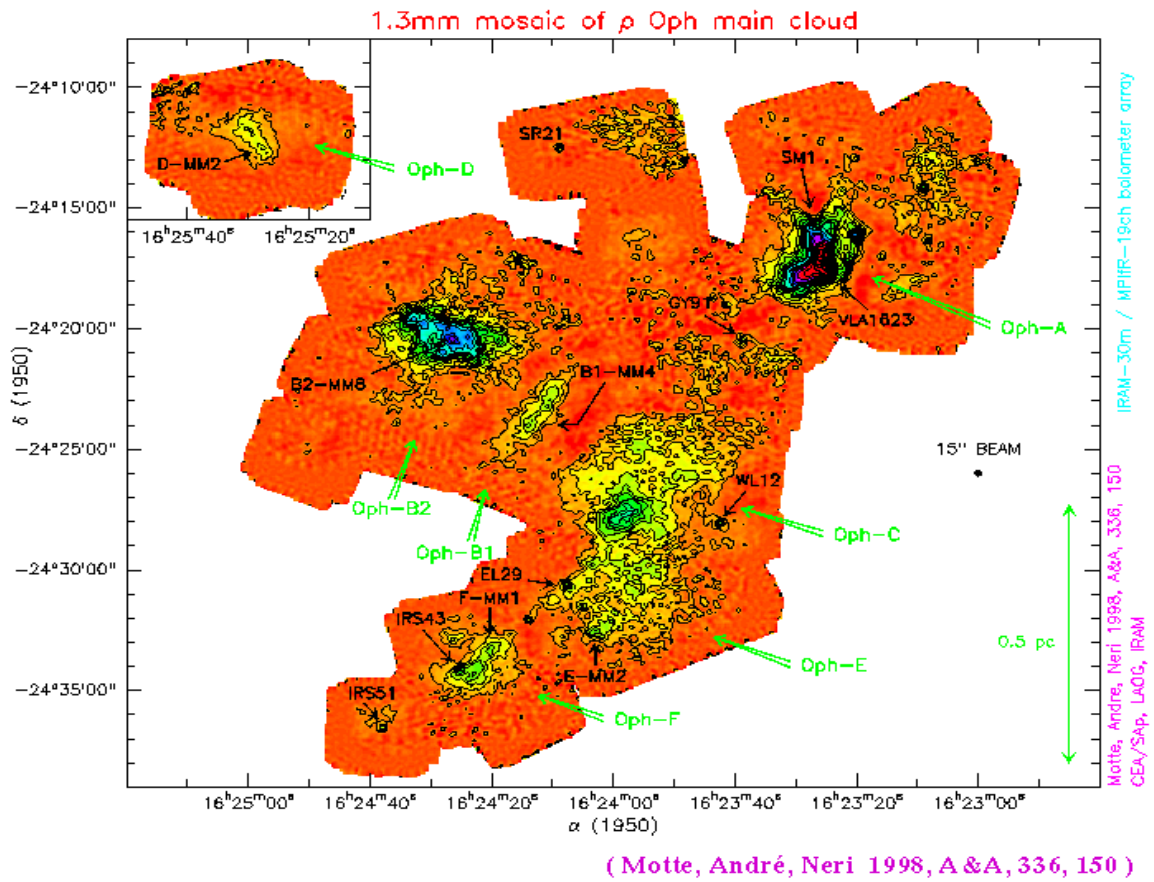
Figure 2.7: **1.3mm mosaic of the ρ Ophiuchus main cloud complex. Indicated are several dense clouds which are the host for clumps and dense prestellar cores.**

masses range from $0.1\,M_\odot$ to $10\,M_\odot$. The crucial feature, which let prestellar cores stand out against the large scale structures in molecular clouds is the fact that they are bound structures which are (most times) not disrupted by the turbulent environment. In this sense they are decoupled from the surrounding flow.

2.4.1 Geometrical Structure

Prestellar cores were born out of their supersonic turbulent environment. Therefore it's not surprising that their geometrical structure shows no symmetry at all, neither spherical nor cylindrical. Due to the statistical nature of the turbulent velocities every prestellar core is unique in its shape and internal velocity structure, see figure 2.2. Typical sizes of prestellar cores range from 10000 to 30000 AU (0.05 to 0.15 pc). Besides their individuality they show a typical radial density structure. Ward-Thompson et al. demonstrated that prestellar cores do not have density profiles which can be modelled by a single scale free power law. Instead they have flat inner radial density profiles steepening toward the edges. Modelling submm data assuming spherical symmetry results in radial density profiles of $\rho(r) \sim r^{-1.2}$ if $r < 4000\,\text{AU}$ and $\rho(r) \sim r^{-2}$ if $4000 < r < 15000\,\text{AU}$.

2.4.2 Rotational Properties

Radio observations of prestellar cores only have access to a two dimensional projection of the density and velocity structures in a prestellar core. This means that prestellar cores are seen in terms of column densities and radial velocities along a line of sight. Think of a sphere-like prestellar core rotating like a rigid body. In this simplified picture the rotation can be detected as a line of sight (LOS) velocity gradient if the rotation axis of the core is not parallel to the LOS. Due to the fact that no one knows the inclination between rotation axis and the line of sight the measured velocity gradient can only yield a lower limit for the real rotation speed.

With this picture in mind a lot of velocity gradient measurements were done to estimate the rotational properties of prestellar cores (e.g. Goodman et al. (1993), see figures 2.8, 2.9). In reality things are more complex. Prestellar cores are not rigid body rotators. They have internal subsonic turbulent velocity fields and, in addition, nonsymmetric shapes. One should keep in mind that rigid rotation is not the only possible way to induce velocity gradients in projection. There are several constellations of a turbulent velocity field leading to a LOS velocity gradients even though there is no rotational motion at all. This was demonstrated by Burkert and Bodenheimer (2000). They showed, that in general, the line-of-sight velocity gradient of an individual turbulent core does not provide a good estimate of its specific angular momentum and that in context with the 'rigid body rotator model' the intrinsic angular momentum is overestimated by a factor of $2 - 3$.
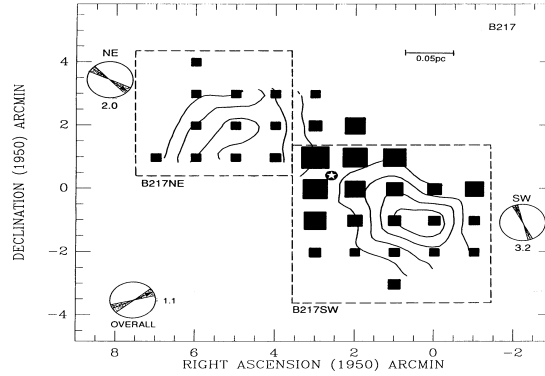
Figure 2.8: **Upper graph: Filled squares of varying size represent the LSR velocity of the peak of the NH_3 line profile at each position., and contours map the column density distribution. The small circle with an arrow indicates the direction of the velocity gradient. Velocity range (6.78 - 7.43 km/s). Lower Graph: Distribution of the measured velocity gradients. Taken from Goodman et al. (1993)**
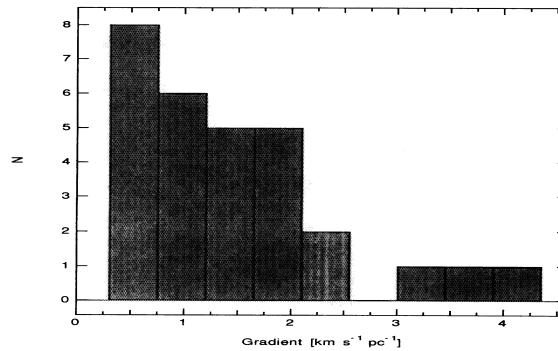
Figure 2.9: **Distribution of velocity gradients, measured in the sample of Goodman et al. (1993)**

Chapter 3

Physical Concepts and Numerical Techniques

3.1 The Hydrodynamic Equations

3.1.1 Euler and Lagrange representation

There are two different points of view, how hydrodynamic processes can be described. For the derivation of the total change of mass, momentum and energy in time it is advantageous to use the Euler representation. In this picture there is used a constant control volume V at a fixed point in space with a surface F and a corresponding unit vector n perpendicular to its surface. The variables of interest (mass, momentum, energy) are analysed inside this volume. The results then refer to points in space which are at rest! In practice, differential volume elements are used, so that the physical variables do not change inside a volume element.

In contrast to that the Lagrange picture uses small comoving volume elements of constant mass. Let us take f as an arbitrary physical variable of a comoving fluid element. To estimate the change in f at time t and at the position $r(t)$ of the volume element one has to calculate the values of f at the positions $r(t)$ and $r(t) + \delta t$ along the trajectory of the fluid element:

$$\frac{df}{dt} := \lim_{\delta t \to 0} \frac{f(r(t + \delta t), t + \delta t) - f(r(t), t)}{\delta t} \tag{3.1}$$

Using the Taylor expansion, the right hand side of (3.1) can be simplified into an expression which gives more physical insight:

$$\frac{df}{dt} = \frac{\partial f}{\partial t} + (v \cdot \nabla) f \tag{3.2}$$

Where $v = dr/dt$ is the velocity vector of the fluid element. Equation (3.2) defines the total derivative D/Dt and connects the Lagrange- and the Euler representation. The left hand side of equation (3.2) describes the total change of f in time as it would be seen in a volume element at rest, resp. the change of f in the Euler picture. The first term on the right hand side describes the change of f in time for a comoving coordinate system, resp. in the Lagrange picture. So that the second term on the right hand side can be interpreted as the advective change of f at some fixed position.

3.1.2   Continuity equation

The continuity equations describes the change of mass in a control volume V or to be more precise, the change of density at any point in space. Due to the conservation of mass, a change of mass in the control volume is always accompanied by a mass flux through the volume's surface.

$$\frac{\partial}{\partial t} \int_V \rho dV \quad = \quad \oint_F \rho(v \cdot n) dF \tag{3.3}$$

The Gaussian law yields the differential form in the Euler representation

$$\frac{\partial \rho}{\partial t} + \nabla(\rho v) = 0 \tag{3.4}$$

and with (3.2) this can be transformed into the Lagrange representation

$$\frac{d\rho}{dt} + \rho \nabla v \quad = \quad 0 \tag{3.5}$$

3.1.3   Equation of motion

In analogy to the continuity equation one can write down a balance equation for the momentum. This is done in consideration of Newton's law and the conservation of momentum. This means, the momentum inside the control volume can be changed by momentum in- or out-flow or by acting forces.

$$\frac{\partial}{\partial t} \int_V \rho v dV = \oint_F \rho v(vn) dF + \int_V \rho f dV - \oint_F pn dF + \oint_F Tn dF \tag{3.6}$$

The term on the left hand side of equation (3.6) is the change of momentum per time. The first term on the right hand side is the convective impulse flux through the surface of the control volume. The next three terms are the forces acting on the fluid. They can be divided into volume ($2^n d$ term) and surface ($3^r d$ and $4^t h$ term) forces. The volume force is written in general terms of a force density ρf. In the context of star formation gravity is the most important volume force which has to be taken into account.

$$f = -\nabla \Phi \tag{3.7}$$

$$\Delta \Phi = 4\pi G \rho \tag{3.8}$$

The surface forces are induced by the fluid outside the control volume. There are pressure forces acting perpendicular to the surface (3rd term) and forces transmitted due to the viscosity of the fluid acting tangential to the surface. These viscous tensions are represented by the stress tensor T (4th term). Using the Gaussian law, (3.6) can be transformed into a differential form

$$\frac{\partial(\rho v)}{\partial t} + [\nabla(\rho v)]v + \rho(v \cdot \nabla)v - \rho f + \nabla p - \nabla T = 0 \tag{3.9}$$

Euler Equation

The Euler equation is the equation of motion for an ideal fluid - a fluid with zero viscosity, no energy dissipation and no conduction of heat. This means that fluid layers of different velocity can slide upon each other without resistance and dissipation of kinetic energy. The Euler equation can be deduced from (3.9) merging the first two terms on the left hand side by inserting the continuity equation. What results is the Euler equation.

$$\frac{\partial v}{\partial t} + (v \cdot \nabla)v = -\frac{1}{\rho}\nabla + f \tag{3.10}$$

Using (3.2) this can be transformed into the Lagrange representation

$$\frac{dv}{dt} = -\frac{1}{\rho}\nabla p + f \tag{3.11}$$

Navier-Stokes Equation

To describe a real fluid we can transform (3.9) using the continuity equation (3.5)

$$\frac{\rho\partial v}{\partial t} + \rho(v \cdot \nabla)v = -\nabla p + \nabla T_{\alpha\beta} + \rho f \tag{3.12}$$

$$= \nabla T'_{\alpha\beta} + \rho f \tag{3.13}$$

$T'_{\alpha\beta} := -p\delta_{\alpha\beta} + T_{\alpha\beta}$ represents the stress tensor (Greek indices representing the three space coordinates and $\delta_{\alpha\beta}$ stands for the Kronecker-Delta). T and T' are tensors of second stage. Using the angular momentum balance in a control volume and inserting (3.9) and (3.4) yields the condition that the stress tensor has to be symmetric, $T_{\alpha\beta} = T_{\beta\alpha}$. To deduce the equation of motion for a real viscous fluid one has to estimate the general form of $T_{\alpha\beta}$.

Energy dissipation in viscous fluids can only take place if there are relative motions between different fluid parcels. During this process momentum is transfered from high velocity regions to regions of low velocity. In the case of a homogeneous velocity field there will be no dissipation at all. This means that the stress tensor will not depend on velocities, but on spatial derivatives of velocities and will be zero if there is a constant velocity field. If one assumes only small velocity gradients, T can be approximated to depend only on linear combinations of first derivatives. This means, in terms of the form $\partial v_\alpha/\partial x_\beta$. Fluids that can be described by this approximation are called 'Newtonian fluids'. In addition to that, T has to vanish if the fluid rotates as a whole like a rigid body. Given a velocity field $v = \omega \times r$, the only vanishing linear combinations are of the form $(\partial v_\alpha/\partial x_\beta + \partial v_\beta/\partial x_\alpha)$. So a general ansatz for the stress tensor which incorporates all conditions required above can be written in the form

$$T_{\alpha\beta} = \left(\frac{\partial v_\alpha}{\partial x_\beta} + \frac{\partial v_\beta}{\partial x_\alpha} - \frac{2}{3}\delta_{\alpha\beta}\sum_{\gamma=1}^{3}\frac{\partial v_\gamma}{\partial x_\gamma}\right) + \zeta\delta_{\alpha\beta}\sum_{\gamma=1}^{3}\frac{\partial v_\gamma}{\partial x_\gamma} \tag{3.14}$$

The term

$$\sigma_{\alpha\beta} = \left(\frac{\partial v_\alpha}{\partial x_\beta} + \frac{\partial v_\beta}{\partial x_\alpha} - \frac{2}{3}\delta_{\alpha\beta}\sum_{\gamma=1}^{3}\frac{\partial v_\gamma}{\partial x_\gamma}\right) \tag{3.15}$$

is called shear tensor and $\eta\sigma$ represents the trace free part of T. The coefficient of the shear viscosity η and the coefficient of the volume viscosity ζ are scalar variables due to the isotropy of the fluid. They are describing the individual features of the fluid depending on pressure and temperature. Because of the second law of thermodynamics only positive values are possible. Often, the volume viscosity can be neglected against the shear viscosity. This is because for a gas ζ is small and for an almost incompressible liquid the term Δv is nearly zero. Fluids with zero volume viscosity ($\zeta = 0$) are called Maxwell fluids. As a result of the kinetic gas theory, a monoatomic ideal gas exactly matches this condition.

Inserting (3.14) into (3.12) yields the equation of motion for a viscous fluid in Euler representation. This equation is called the Navier-Stokes equation. Transformed into the Lagrange picture and with component representation:

$$\rho\frac{dv_\alpha}{dt} \quad = \quad -\frac{\partial p}{\partial x_\alpha} + \frac{\partial T_{\alpha\beta}}{\partial x_\beta} + \rho f_\alpha \tag{3.16}$$

Here and in the following equations the summation convention of Einstein is used.

3.1.4   Energy Equation

The total energy of a moving fluid element is the sum of internal energy and kinetic energy. So one can express the total energy in the form

$$E_{tot} \quad = \quad \int_V \rho\left(\epsilon + \frac{1}{2}v^2\right)dV \tag{3.17}$$

Here ϵ denotes the specific internal energy, i.e., the internal energy per unit mass. To derive a energy balance equation, one can use the first law of thermodynamics which states, that the sum of all energies is conserved. Therefore a change in the total energy is always accompanied by an energy flux through the volume's surface, by a heat flux, radiative flux or mechanical work due to forces acting on the volume. Keeping all this in mind, the energy equation can be written in the form

$$\frac{\partial}{\partial t}\int_V \rho\left(\epsilon + \frac{1}{2}v^2\right)dV \quad = \quad -\oint_F \rho\left(\epsilon + \frac{1}{2}v^2\right)(v \cdot n)dF$$

$$+ \int_V \rho(f \cdot v)dV - \int_F p(n \cdot v)dF + \oint_F ((Tn) \cdot v)dF$$

$$- \oint_F (q \cdot n)dF + \int_V Q_{\text{rad}}dV \tag{3.18}$$

The left hand side of equation (3.18) describes the change of total energy inside the volume V. The first term on the right hand side stands for the convective energy flux through the volume's surface F. The next three terms in the second row of (3.18) represent the energy exchange due to mechanical work: the outer volume force (1st term), pressure force (2nd term) and viscous dissipation (3rd term). The energy exchange by heat flux and radiative flux is represented in the two terms of the third row of (3.18). Where q is the heat flux vector and Q_{rad} describes the absorbed, resp. emitted radiation per volume.

The energy equation (3.18) only holds if the chemical composition does not change in space

and time (i.e., there are no chemical reactions and no diffusive processes). It can be transformed by the Gaussian law into a differential representation:

$$\frac{\partial}{\partial t}\left[\rho\left(\epsilon + \frac{1}{2}v^2\right)\right] + \nabla\left[\rho\left(\epsilon + \frac{1}{2}v^2\right)\right] = \rho(f \cdot v) - [\nabla(\rho v)]v + \nabla(Tv) - \nabla q + Q_{rad} \tag{3.19}$$

The term on the left hand side of (3.19) can be simplified using the continuity equation (3.4):

$$\rho\frac{\partial}{\partial t}\left(\epsilon + \frac{1}{2}v^2\right) + \rho v \cdot \nabla\left(\epsilon + \frac{1}{2}v^2\right) = \rho(f \cdot v) - [\nabla(\rho v)]v + \nabla(Tv) - \nabla q + Q_{rad} \tag{3.20}$$

One can use the change of the internal specific energy to find an expression for the change of the specific entropy. Starting with the thermodynamical relation

$$dE = TdS - pdV \tag{3.21}$$

resp.

$$\begin{aligned} d\epsilon &= Tds - pd\left(\frac{1}{\rho}\right) \\ &= Tds + \frac{p}{\rho^2}d\rho \end{aligned} \tag{3.22}$$

From (3.22) it is straightforward to get an expression for the specific entropy:

$$T\frac{ds}{dt} = \frac{d\epsilon}{dt} + \frac{p}{\rho}\nabla v \tag{3.23}$$

Energy Equation for an ideal fluid

As defined above, in an ideal fluid there exists neither dissipation nor heat flux. So the stress tensor T and the heat flux vector q vanish. If we require in addition no absorption and emission of radiation ($Q_{rad} = 0$) then equation (3.20) can be simplified as follows:

$$\rho\frac{\partial}{\partial t}\left(\epsilon + \frac{1}{2}v^2\right) + \rho v \cdot \nabla\left(\epsilon + \frac{1}{2}v^2\right) = \rho(f \cdot v) - \nabla(\rho v) \tag{3.24}$$

Using (3.2) and the Euler equation in Lagrange representation we get

$$\begin{aligned} \rho\frac{\partial}{\partial t}\left(\frac{1}{2}v^2\right) + \rho v \cdot \nabla\left(\frac{1}{2}v^2\right) &= \rho\frac{d}{dt}\left(\frac{1}{2}v^2\right) \\ &= \rho v \cdot \frac{dv}{dt} \\ &= -v \cdot \nabla p + \rho(v \cdot f) \end{aligned} \tag{3.25}$$

(3.24) can be simplified further resulting in an equation for the specific energy in Lagrange representation:

$$\rho\frac{\partial \epsilon}{\partial t} + \rho v \cdot \nabla \epsilon = -p\nabla v \tag{3.26}$$

$$\frac{d\epsilon}{dt} = -\frac{p}{\rho}\nabla v \tag{3.27}$$

Energy Equation for a viscous fluid

In the case of a viscous fluid (3.20) already represents the general form of the energy equation. In analogy to (3.25), using (3.2) and the Navier-Stokes equation (3.16) one gets

$$\rho\frac{\partial}{\partial t}\left(\frac{1}{2}v^2\right) + \rho v \cdot \nabla\left(\frac{1}{2}v^2\right) \;=\; -v \cdot \nabla p + v \cdot (\nabla T) + \rho(v \cdot f) \tag{3.28}$$

Inserting (3.20) yields the equation for the specific energy for a viscous fluid:

$$\rho\frac{\partial \epsilon}{\partial t} + \rho v \cdot \nabla \epsilon \;=\; -p\nabla v + T_{\alpha\beta}\frac{\partial v_\alpha}{\partial x_\beta} - \nabla q + Q_{rad} \tag{3.29}$$

$$\frac{\partial \epsilon}{\partial t} = -\frac{p}{\rho}\nabla v + \frac{1}{\rho}T_{\alpha\beta}\frac{\partial v_\alpha}{\partial x_\beta} - \frac{1}{\rho}\nabla q + \frac{Q_{rad}}{\rho} \tag{3.30}$$

In a first approximation, the heat flux vector q can be replaced using Fourier's law, which states that the heat flux is proportional to the temperature gradient in the fluid:

$$q \;=\; -\kappa\nabla T \tag{3.31}$$

Here κ denotes the heat conduction coefficient. The negative sign keeps track of the fact that the heat flux it directed from warm to the cold regions. Inserting the energy equation (3.30) into the entropy equation (3.23) yields

$$T\frac{ds}{dt} \;=\; \frac{1}{\rho}T_{\alpha\beta}\frac{\partial v_\alpha}{\partial x_\beta} - \frac{1}{\rho}\nabla q + \frac{Q_{rad}}{\rho} \tag{3.32}$$

The term $T_{\alpha\beta}\partial v_\alpha/\partial x_\beta$ describing the fraction of dissipated energy can be transformed using the stress tensor in the representation (3.14). Because the shear tensor $\sigma_{\alpha\beta}$ is symmetric and traceless (see definition (3.15)) one can write

$$
\begin{aligned}
T_{\alpha\beta}\frac{\partial v_\alpha}{\partial x_\beta} \;&=\; \frac{1}{2}T_{\alpha\beta}\left(\frac{\partial v_\alpha}{\partial x_\beta} + \frac{\partial v_\beta}{\partial x_\alpha}\right)\\
&=\; \frac{1}{2}(\eta\sigma_{\alpha\beta} + \zeta\delta_{\alpha\beta}\nabla v)(\sigma_{\alpha\beta} + \frac{2}{3}\delta_{\alpha\beta}\nabla v)\\
&=\; \frac{1}{2}\eta\sigma_{\alpha\beta}\sigma_{\alpha\beta} + \frac{1}{2}(\zeta + \frac{2}{3}\eta)\delta_{\alpha\beta}\sigma_{\alpha\beta}\nabla v) + \frac{1}{3}\zeta\delta_{\alpha\beta}\delta_{\alpha\beta}(\nabla v)^2\\
&=\; \frac{1}{2}\eta\sigma_{\alpha\beta}\sigma_{\alpha\beta} + \zeta(\nabla v)^2 \geq 0
\end{aligned}
\tag{3.33}
$$

Using this we can write down the change in the specific entropy:

$$\rho T\frac{ds}{dt} \;=\; \frac{1}{2}\eta\sigma_{\alpha\beta}\sigma_{\alpha\beta} + \zeta(\nabla v)^2 - \nabla q + Q_{rad} \tag{3.34}$$

One sees, taking into account equation (3.33) that the viscosity induced friction evokes always an increase of internal energy resp. of the entropy. This fact can also be depicted in another way: With the assistance of the continuity equation (3.4) we can convert (3.28)

$$\frac{\partial}{\partial t}\left(\frac{1}{2}\rho v^2\right) \;=\; -\nabla\left[\left(\frac{1}{2}\rho v^2 + p - T\right)v\right] + p\nabla v + \rho(v \cdot f) - T_{\alpha\beta}\frac{\partial v_\alpha}{\partial x_\beta} \tag{3.35}$$

This is an expression for the change of the energy density per time. Integrating over the whole fluid volume, applying Gauss's theorem and neglecting surface terms at infinity yields an equation for the evolution of the total kinetic energy:

$$\frac{\partial E_{kin}}{\partial t} \quad = \quad \int p \nabla v \, dV + \int \rho(v \cdot f) dV - \int T_{\alpha\beta} \frac{\partial v_\alpha}{\partial x_\beta} dV \tag{3.36}$$

The first volume integral on the right hand side denotes the change in kinetic energy due to the compressibility of the fluid. The second one considers the external volume force resp. the corresponding potential energy. And the last integral represents the viscosity of the fluid. Because of (3.33), the last term is always negative, i.e. the kinetic energy can only decline with time. That means, the viscosity dissipates kinetic energy, resp. transforms it into heat.

3.1.5 The Equation of state

The system of equations built up so far (continuity equation, equation of motion and energy equation) is not closed regarding the variables in use. In addition one needs to specify, besides the coefficients for the viscosity, the properties of the matter. To close this system of equations one needs an equation of state which connects pressure p, density ρ and temperature T. This equation will provide the missing relations of e.g. $p = p(\rho, \epsilon)$ and $T = T(\rho, \epsilon)$

3.1.6 The ideal gas

In the context of star formation the ideal gas equation plays a fundamental role, because it is simple and valid for a large range in density and temperature. One has to be careful to not confuse the terms 'ideal gas' and 'ideal fluid' because viscous fluids (like molecular hydrogen gas) can behave like an ideal gas.
The ideal gas equation is of the form

$$p \quad = \quad \frac{k_b T}{\mu m_u} \rho \tag{3.37}$$

where k_b is the Boltzmann constant, μ is the molecular weight and $m_u = 1/N_A = 1.66 \times 10^- 24g$ is the atomic mass unit. To have some numbers, $\mu = 1.24$ for the solar gas composition, $\mu = 2.36$ for the gas in cold molecular clouds and $\mu = 0.5$ for completely ionized hydrogen gas.
In the case of an ideal gas the specific internal energy is connected to the temperature as follows:

$$\epsilon \quad = \quad \frac{1}{(\gamma - 1)} \frac{k_b T}{\mu m_u}$$
$$= \quad c_v T \tag{3.38}$$

γ is known as the polytropic index or adiabatic exponent. It is concatenated to the degrees of freedom

$$\gamma \quad = \quad \frac{2}{f} + 1 \tag{3.39}$$

The most common case during the early and still cold phase of star formation is a mixture of diatomic molecular gas: $f = 5 \longrightarrow \gamma = 7/5$. Or, in a later phase, when all molecules have

already dissociated into a composition of atoms: $f = 3 \longrightarrow \gamma = 5/3$. Using the heat capacity coefficients for constant volume c_v and constant pressure c_p we can write

$$\gamma = \frac{c_p}{c_v} \quad \Longrightarrow \quad \frac{k_b}{\mu m_u} = c_p - c_v \tag{3.40}$$

There is also the possibility to express the specific internal energy in terms of pressure and density. By doing so one can eliminate the temperature from the system of equations (The only temperature dependence then remains in the viscosity coefficients η and ζ).

$$\epsilon \;\; = \;\; \frac{1}{\gamma - 1} \frac{p}{\rho} \tag{3.41}$$

In general it is assumed that the fluid is in a local equilibrium. This means that $\epsilon(\rho, p)$ is locally of the same form as in the case of thermodynamic equilibrium.

3.2   Stability of Self-Gravitating Fluids

The first and usually sufficient approach to determine the stability properties of physical fluids is to analyze the linearized set of equations. In general, an equilibrium system is described by a time independent solution of the Boltzmann equation

$$\frac{df}{dt} \;\; = \;\; \frac{\partial f}{\partial t} + \dot{q} \nabla_q f + \dot{p} \nabla_p f \tag{3.42}$$

$$= \;\; \frac{\partial f}{\partial t} + p \nabla_q f + F \nabla_p f \tag{3.43}$$

a distribution function $f_0(q, p)$ with $df_0/dt = 0$. Small perturbations to this equilibrium state can be written as

$$f(q, p, t) = f_0(q, p) + \epsilon f_1(q, p, t) \tag{3.44}$$

with $\epsilon \ll 1$. This can be substituted into the Boltzmann equation (3.42). The terms independent of ϵ sum to zero because they are the equilibrium solution. In a first order approach, terms of order ϵ^2 and higher are neglected since $\epsilon \ll 1$. What remains is a linearized set of equations governing the time evolution of the perturbation. Deriving a dispersion relation, the properties of growing and decaying modes can be studied. The linearized set of equations for an isothermal, selfgravitating fluid are

$$\frac{\partial \rho_1}{\partial t} + \rho_0 \nabla \cdot v_1 \;\; = \;\; 0 \tag{3.45}$$

$$\frac{\partial v_1}{\partial t} \;\; = \;\; -\nabla c_s^2 \frac{\rho_1}{\rho_0} - \nabla \phi_1 \tag{3.46}$$

$$\triangle \phi_1 \;\; = \;\; 4 \pi G \rho_1 \tag{3.47}$$

Here the viscosity effects are neglected ($\eta = \zeta = 0$). The equilibrium state is characterized by $\rho_0 = const$ and $v_0 = 0$. From the definition of the isothermal sound speed $p = c_s^2 \rho$ it follows that $p_1 = c_s^2 \rho_1$ Furthermore, we make the ad hoc assumption that Poisson's equation describes only the relation between the perturbed potential and the perturbed density. In this case, $\phi_0 = 0$ can be chosen. This is, what is called the Jeans swindle (Binney, Tremaine

1987). By taking the time derivative of equation (3.46) and the divergence of (3.47) and by eliminating v_i and ϕ_1, the equations can be combined into a wave equation for the density perturbation ρ_1,

$$\frac{\partial^2 \rho_1}{\partial t^2} - c_s^2 \nabla^2 \rho_1 - 4\pi G \rho_0 \rho_1 \quad = \quad 0 \tag{3.48}$$

Since the equilibrium state is homogeneous, the coefficients of the partial derivatives in (3.48) are independent of position and time. The solution of this type of partial differential equation is known to be a superposition of plane waves,

$$\rho_1(r,t) \quad = \quad \int d^3 k A(k e^{i[kr - \omega(k)t]} \tag{3.49}$$

The waves follow the dispersion relation

$$\omega^2 \quad = \quad c_s^2 k^2 - 4\pi G \rho_0 \tag{3.50}$$

If the density ρ_0 or the wave length $\lambda = 2\pi/k$ are small, the dispersion relation (3.50) reduces to that of a sound wave, $\omega^2 = c_s^2 k^2$. With increasing wave length or density, the frequency decreases and will eventually become negative. When $\omega^2 < 0$, say $\omega^2 = -\kappa^2$, the time dependence of the solution is proportional to $exp(\pm\kappa t)$, corresponding to exponential growth or decay. The existence of a growing solution implies that the system is unstable. Hence, from equation (3.50) it follows that modes will collapse for wave numbers

$$k^2 < k_J^2 \quad = \quad \frac{4\pi G \rho_0}{c_s^2} \tag{3.51}$$

The critical wave number k_J is called the Jeans wave number. In terms of the wave length, a perturbation is unstable if the wave length exceeds the Jeans length $\lambda_J = 2\pi/k_J$, that is, if

$$\lambda^2 > \lambda_J^2 \quad = \quad \frac{\pi c_s^2}{G \rho_0} \sim \frac{T}{\rho_0} \tag{3.52}$$

Assuming the perturbation is spherical with diameter λ_J, this corresponds to a critical mass contained inside the perturbed volume. So the well known Jeans mass is

$$M_J = \frac{4\pi}{3} \rho_0 \left(\frac{1}{2}\lambda_J\right)^3 \quad = \quad \frac{1}{6}\pi \rho_0 \left(\frac{\pi c_s^2}{G \rho_0}\right)^{\frac{3}{2}} \tag{3.53}$$

For isothermal gases substituting the sound speed by its dependence on the temperature, $c_s^2 = RT$, the critical mass can be expressed in terms of density and temperature:

$$M_J = \frac{\pi^{\frac{5}{2}}}{6}\left(\frac{R}{G}\right)^{\frac{3}{2}} \cdot \rho^{-\frac{1}{2}} T^{\frac{3}{2}} \quad \sim \quad \sqrt{\frac{T^3}{\rho_0}} \tag{3.54}$$

Using the ideal gas equation and plugging it in 3.54 the Jeans mass can be expressed in terms of the number density of the hydrogen molecules $n(H_2)$, the temperature T and the molecular weight μ,

$$M_J[M_\odot] \quad = \quad 49.5\,M_\odot \cdot \frac{1}{\mu^2} \cdot \sqrt{\frac{T^3}{n(H_2)}} \tag{3.55}$$

Inserting the typical mean molecular weight $\mu = 2.36g\ cm^{-3}$ one gets

$$M_J[M_\odot] \quad = \quad 8.9\,\mathrm{M_\odot} \cdot \sqrt{\frac{\mathrm{T}^3}{\mathrm{n(H_2)}}} \qquad\qquad (3.56)$$

The following table gives an overview of critical Jeans masses occurring in molecular clouds and prestellar cores:

	T=5K	T=10K	T=20K	T=50K	T=100K
$n(H_2) = 10^1 cm^{-3}$	31.5 M$_\odot$	89.0 M$_\odot$	251.7 M$_\odot$	995.1 M$_\odot$	2814.4 M$_\odot$
$n(H_2) = 10^2 cm^{-3}$	10.0 M$_\odot$	28.1 M$_\odot$	79.6 M$_\odot$	314.7 M$_\odot$	890.0 M$_\odot$
$n(H_2) = 10^3 cm^{-3}$	3.1 M$_\odot$	8.9 M$_\odot$	25.2 M$_\odot$	99.5 M$_\odot$	281.4 M$_\odot$
$n(H_2) = 10^4 cm^{-3}$	1.0 M$_\odot$	2.8 M$_\odot$	8.0 M$_\odot$	31.5 M$_\odot$	89.0 M$_\odot$
$n(H_2) = 10^5 cm^{-3}$	0.3 M$_\odot$	0.9 M$_\odot$	2.5 M$_\odot$	10.0 M$_\odot$	28.1 M$_\odot$
$n(H_2) = 10^6 cm^{-3}$	0.1 M$_\odot$	0.3 M$_\odot$	0.8 M$_\odot$	3.1 M$_\odot$	8.9 M$_\odot$
$n(H_2) = 10^{10} cm^{-3}$	0.001 M$_\odot$	0.003 M$_\odot$	0.008 M$_\odot$	0.03 M$_\odot$	0.089 M$_\odot$

The critical mass for a perturbation to collapse, scales as $M_J \sim T^{3/2}\rho_0^{1/2}$, i.e., it decreases with increasing density and decreasing temperature. The Jeans instability has a simple physical interpretation. The energy density of a sound wave is positive. However, its gravitational energy is negative, because the enhanced attraction in the compressed regions outweighs the reduced attraction in the diluted regions. The instability sets in at the wavelength λ_J where the net energy density becomes negative. The perturbation will grow allowing the energy to decrease even further. In isothermal gas, there is no mechanism that prevents the a complete collapse.

In reality, during the collapse of a molecular gas clump, the opacity increases and at densities of $n(H_2) > 10^{10} cm^{-3}$, the equation of state for the collapsing gas becomes adiabatic. So the collapse is decelerated, the Jeans mass remains roughly constant even though the contraction still goes on. When the temperature exceeds $3000K$ at densities of $n(H_2) > 10^{16} cm^{-3}$ thermal energy is used up by dissociation of the hydrogen molecules and the collapse accelerates again. Finally at a central density of $n(H) \approx 10^{24} cm^{-3} \Leftrightarrow \rho \approx 1g/cm^3$ the fusion process sets in. This energy source stops the collapse process and leads to a new equilibrium (e.g. Tohline (1982))

density	temperature	molecular weight	Jeans mass
10^{-13} g/cm^3	$10K$	2.36 g/mol	1.8×10^{-3} M$_\odot$
10^{-8} g/cm^3	$2500K$	2.36 g/mol	2.2×10^{-2} M$_\odot$
10^{-2} g/cm^3	$10000K$	1.18 g/mol	7.1×10^{-4} M$_\odot$
10^0 g/cm^3	$60000K$	0.57 g/mol	4.5×10^{-3} M$_\odot$

3.3 The Role of Turbulence

Almost all known star formation takes place in molecular clouds. Compared to the stability analysis of self gravitating gaseous systems (section 3.2) molecular clouds exceed vastly the critical mass for gravitational collapse. One would therefore expect that they form stars on their free fall timescale

$$t_{ff} = \sqrt{\frac{3\pi}{32G\rho_0}} \quad = \quad 1.4 \cdot 10^6 \,\text{yrs}\sqrt{\text{n}[10^3\text{cm}^{-3}]} \tag{3.57}$$

For a typical molecular cloud with a mean density of 10^2cm^{-3} this is about 4×10^6 yrs. Taking into account the mass of gas condensed in molecular clouds ($2 \times 10^9 \,\text{M}_\odot$) this would imply a star formation rate of about $500\,\text{M}_\odot/\text{yr}$. This exceeds the currently observed rate by a factor of ~ 100 (Scalo (1986), Evans (1999)). Even if the star formation efficiency is only less than 10 percent the life time of molecular clouds should be an order of magnitude larger than their free fall time scale to be consistent with the observed star formation rates. It should be mentioned that this is subject to a controverse discussion. Another hint, that molecular clouds do not simply collapse on their free fall timescale is the fact that star formation is not accompanied by the collapse of the whole molecular cloud. Instead, stars form in very localized regions distributed in an apparently stable cloud (Williams et al. (2000)). But what prevents molecular clouds from global collapse? One good candidate are the supersonic turbulent motions that are present almost everywhere in molecular clouds (Larson (1981)). Turbulence is a crucial common feature of molecular clouds and provides an additional support against gravitational collapse. But numerical simulations of turbulent self gravitating media (Mac Low et al. (1998a), Klessen et al. (2000)) have shown that turbulence decays on timescales of the free fall time. So to prevent molecular clouds from collapse turbulence has to be driven. There are several potential driving mechanisms for turbulence: galactic sheer motions, supernova events, solar winds, bipolar outfrows and jets etc. It is worth noting the ambivalent action of turbulence on the gas. On the one hand it acts like an additional pressure but on the other hand it is the source of density fluctuations. So it is the large scale turbulent motion which builds up the seeds for prestellar collapse and star formation by locally compressing the gas into a Jeans unstable state.

3.4 Smoothed Particle Hydrodynamics (SPH)

The aim of the SPH method is to solve numerically the hydrodynamical equations. Technically this is a system of coupled partial differential equations. The core of the SPH method is the transformation of the coupled partial differential equations with continuous field variables into a system of coupled normal (common) differential equations with variables at discrete mesh points in space. In contrast to the classical grid methods the SPH code uses mesh points neither fixed in space nor ordered in a grid. The SPH method is a Lagrangian method. So one can think of the mesh points as buoys drifting with the flow and measuring the state of the fluid at these positions. The formalism by which this transformation is done can be divided in two steps:

1. Kernel smoothing. Here all space dependent functions are convolved by a kernel function

2. Monte-Carlo-Integration of the convolution integrals and discertization

In a last step it is now possible to numerically solve the system of common differential equations and integrate it forward in time. For a space dependent function $f(r)$ its value at position r can be approximated by the convolution with an appropriate kernel function:

$$\langle f(r)\rangle \quad = \quad \int\limits_{V(h)} f(r+r')W(r',h)dV' \tag{3.58}$$

The convolution of f with the kernel function W results in a weighted mean for the values of f around the position r. The kernel length h controls the spatial extent from which the weighted mean is taken. It defines the scale over which forces and physical fluid properties are smoothed out. Independent of h the kernel function has to be normalized:

$$\int\limits_{V} W(r',h)dV' \quad = \quad 4\pi\int\limits_{0}^{\infty} W(r',h)r'^2 dr' = 1 \tag{3.59}$$

It follows for the limit $h \to 0$ that

$$\langle f(r)\rangle \longrightarrow f(r) \tag{3.60}$$

For h becoming infinitely small, the kernel $W(r,h)$ approaches the Dirac delta function $\delta(r)$. For simplicity, most authors use spherical symmetry in the smoothing and averaging process, i.e. the kernel reduces to an isotropic function of the interparticle distances. This constraints the achievable resolution, especially when dealing with huge density gradients along a preferred axis like in shocks, filamentary and sheet like structures or accretion disks. To circumvent this disadvantage one can introduce a tensor description of the smoothing method and use anisotropic kernels to account for anisotropies in the particle distribution. Although this approach has considerable advantages over spherical averaging, it is more complicated and expansive in computing time so that we preferred here the fast spherical kernel. For consistency, we use the spherical averaging procedure throughout the entire computational scheme.

The prevalent spherical kernel function used in most SPH codes is the spline kernel of Lattanzio et al. (1985). This is also the kernel used for the simulations presented here. It is defined on a compact support, and therefore only a small number of neighbouring particles have to be summed over to calculate the SPH quantities.

$$W(r,h) = \frac{\sigma}{h^\nu} \begin{cases} 1 - \frac{3}{2}v^2 + \frac{3}{4}v^3 & \text{if } 0 \le v < 1 \\ \frac{1}{4}(2-v)^3 & \text{if } 1 \le v < 2 \\ 0 & \text{otherwise} \end{cases} \tag{3.61}$$

Here $v := r_i - r_j$ represents the distance between two SPH particles.

In the following I want to present a short collection of useful mathematical identities for the SPH quantities. According to equation (3.60) the kernel function can be interpreted as an approximation to the delta function for finite h. Hence, the averaged function $\langle f(r)\rangle$ can be expanded into a Taylor series for the smoothing length h. If the kernel is an even function the first order term vanishes and the errors up to second order are given by,

$$\langle f(r)\rangle \quad = \quad f(r) + \mathcal{O}(h^2) \tag{3.62}$$

For the spherical kernel used in the SPH code here, equation 3.62 reads

$$\langle f(r) \rangle = f(r) + K \frac{h^2}{6} \nabla^2 f(r) + \mathcal{O}(h^3) \tag{3.63}$$

with the constant K being independent of h. The approximation of $f(r)$ by $\langle f(r) \rangle$ is therefore of second order in h. Since the term in h^2 is multiplied by the gradient of f, this implies perfect equality for constant or linear functions. Furthermore, for the term in h^2 to be small, the function f should not be discontinuous or have too large gradients over the size of the kernel. This causes problems in the treatment of strong shock fronts, see chapter 3.5.1.
The smoothing process itself is linear with respect to summation and multiplication,

$$\langle f(r) + g(r) \rangle = \langle f(r) \rangle + \langle g(r) \rangle \tag{3.64}$$

$$\langle f(r) \cdot g(r) \rangle = \langle f(r) \rangle \cdot \langle g(r) \rangle \tag{3.65}$$

The first equation is an identity following from the linearity of integration with respect to summation, and the second one is true to second order in h. It furthermore follows for the time derivative and the gradient

$$\frac{d}{dt} \langle f(r) \rangle = \left\langle \frac{d}{dt} f(r) \right\rangle \tag{3.66}$$

$$\nabla \langle f(r) \rangle = \langle \nabla f(r) \rangle \tag{3.67}$$

Because the state of the fluid is evaluated only at discrete points (the positions of the SPH particles) the convolution integral of (3.58) reduces to a sum over the N neighbouring SPH particles r_j inside $2h$ around the particle r_i :

$$\langle f(r_i) \rangle = \sum_{j=1}^{N} \frac{m_j}{\rho(r_j)} f(r_j) W(r_i - r_j, h) \tag{3.68}$$

The term $m_j / \rho(r_j)$ simply results from the normalization of the kernel function and represents an expansion of the number density:

$$\langle n(r_j) \rangle = \frac{\rho(r_j)}{m_j} \tag{3.69}$$

Equation (3.68) is the fundamental equation for the SPH method, as it allows one to find smoothed approximations to the physical quantities of the fluid.
The smoothing mechanism also provides a very advantageous way to compute gradients of fluid properties. By definition

$$\langle \nabla f(r) \rangle = \int_{V(h)} \nabla f(r') W(r - r', h) dV' \tag{3.70}$$

Integrating by parts yields

$$\langle \nabla f(r) \rangle = \int_{S(h)} f(r') W(r - r', h) n \, da + \int_{V(h)} f(r') \nabla W(r - r', h) dV' \tag{3.71}$$

The surface term can be neglected due to the fact that the kernel function vanishes beyond $2h$. Neglecting the surface terms the integral equation can be transformed into a summation for a discrete number of points, as done before:

$$\langle \nabla f(r_i) \rangle \quad = \quad \sum_{j=1}^{N} \frac{m_j}{\rho(r_j)} f(r_j) \nabla W(r_i - r_j, h) \tag{3.72}$$

Using this and the SPH base equation (3.68) any fluid property and its local gradient can be evaluated as long as ∇W does not vanish (which is the case inside a radius of $2h$).
Note that the Nabla operator now acts only on the a priori known kernel function. In practice the kernel and its gradients are tabulated so that they can be accessed every time which saves a crucial amount of computing time.

3.4.1   The Hydrodynamic Equations in SPH notation

Armed with base equation (3.68) and equation (3.72) describing the handling of the gradients it is now possible to transform the set of hydrodynamic equations into the SPH representation. First one can find an expression for the density at particle position r_i by simply replacing the arbitrary function $f(r_i)$ by the density $\rho(r_i)$:

$$\langle \rho(r_i) \rangle \quad = \quad \sum_{j=1}^{N} m_j W(r_i - r_j, h) \tag{3.73}$$

Continuity Equation

Now the continuity equation is exemplarily transformed into the SPH representation to sketch how the SPH method is applied to a differential equation. First the continuity equation is expanded

$$\frac{d\rho}{dt} \quad = \quad -\nabla(\rho v) + (v \cdot \nabla)\rho \tag{3.74}$$

Now the kernel softening is applied providing the approximated values:

$$\langle \frac{d\rho}{dt} \rangle \quad = \quad \langle -\nabla(\rho v) + (v \cdot \nabla)\rho \rangle \tag{3.75}$$

Using the algebraic rules inherent to the SPH method one gets

$$\frac{d\langle \rho \rangle}{dt} \quad = \quad -\langle \nabla(\rho v) \rangle + \langle v \rangle \cdot \langle \nabla \rho \rangle \tag{3.76}$$

For further details all around SPH I want to recommend the doctor thesis of Roland Speith (http://www.tat.physik.uni-tuebingen.de/ speith/lopubl.html) which gives a comprehensive description of the SPH method. Discretization of (3.76) and subsequent application of the SPH representation for gradients (3.72) yields

$$\frac{d\langle \rho_i \rangle}{dt} \quad = \quad -\sum_{j=1}^{N} \frac{m_j}{\rho_j} \rho_j v_j \cdot \nabla W(r_i - r_j, h) + v_i \left(\sum_{j=1}^{N} \frac{m_j}{\rho_j} \rho_j \nabla W(r_i - r_j, h) \right) \tag{3.77}$$

so that the continuity equation in the SPH notation can be written in the form

$$\frac{d\rho_i}{dt} = \sum_{j=1}^{N} m_j (v_i - v_j) \cdot \nabla_i W(r_i - r_j, h) \tag{3.78}$$

The essential alternative to the SPH continuity equation is to estimate the density directly by equation (3.73). This is exactly what is done in the SPH code used here.

Euler Equation

$$\frac{dv_i}{dt} = \sum_{j=1}^{N} m_j \left(\frac{p_i}{\rho_i^2} + \frac{p_j}{\rho_j^2} \right) \nabla_i W(r_i - r_j, h) \tag{3.79}$$

Navier-Stokes Equation plus Gravity

$$\frac{dv_i}{dt} = \sum_{j=1}^{N} m_j \left(\frac{p_i}{\rho_i^2} + \frac{p_j}{\rho_j^2} + \Pi_{ij} \right) \nabla_i W(r_i - r_j, h) - G \frac{m_j}{r_{ij}^2} \cdot \frac{r_{ij}}{|r_{ij}|} \tag{3.80}$$

Artificial Viscosity

There are two main reasons to implement viscosity into the SPH method. The first is simply to solve the general Navier-Stokes equation of a real fluid. The second has to do with the fact that in most astrophysical problems the molecular viscosity is very small and dissipation of kinetic energy should occur only in shocked regions. Therefore, one is able to neglect the explicit treatment of physical viscosity. Nevertheless, there is the need to introduce at least an artificial viscosity to treat shock fronts correctly because the process of energy dissipation can not be described by an ideal fluid. Besides the effects of numerical diffusivity and dissipation inherent to every discretization of the hydrodynamical equations, in the SPH method one needs to prevent particle interpenetration in strong shocks. The only way to enforce this is to especially smear out the shock interface and introduce terms to allow dissipation of kinetic energy in regions with strong velocity divergence. The standard formulation for the artificial viscous pressure is

$$p_\alpha = \Pi_\alpha \rho^2 = -\alpha \rho l c_s (\nabla \cdot v) \qquad \text{bulk viscosity} \tag{3.81}$$

$$p_\beta = \Pi_\beta \rho^2 = -\beta \rho l^2 (\nabla \cdot v)^2 \qquad \text{Neumann-Richtmyer viscosity} \tag{3.82}$$

The free parameters α and β control the strength of the viscous terms, and l is the scale over which the shock is smeared out, typical values are $l \approx 3h$. Equation (3.81) is a bulk viscosity. Its primary purpose is to dampen post-shock oscillations. Equation (3.82) is a second order von Neumann-Richmyer viscosity needed to avoid particle interpenetration in high Mach number shocks. Typical values for the free parameters are $\alpha \approx 1$ and $\beta \approx 2$ which guarantee adequate treatment of shocks up to Mach numbers of 10 (Bate 1995 PhD thesis). Implemented into the SPH formalism the viscous force acting on particle i is then

$$\langle F(r_i)^{visc} \rangle = \sum_{j=1}^{N} m_j \Pi_{ij} W(r_i - r_j, h_{ij}) \tag{3.83}$$

Where Π_{ij} is the viscosity tensor:

$$\Pi_{ij} = \begin{cases} \dfrac{-\alpha\frac{1}{2}(c_{s,i}+c_{s,j})\mu_{ij}+\beta\mu_{ij}^2}{\frac{1}{2}(\rho_i+\rho_j)} & \text{if } (v_i - v_j)(r_i - r_j) < 0 \\ 0 & \text{if } (v_i - v_j)(r_i - r_j) > 0 \end{cases} \tag{3.84}$$

with

$$\mu_{ij} = \frac{h(v_i - v_j) \cdot (r_i - r_j)}{(r_i - r_j)^2 + \epsilon h^2} \tag{3.85}$$

if a constant smoothing length is used. In the case of a time dependent individual smoothing length for each particle, the constant variable h of equation (3.85) has to be replaced by $\frac{1}{2}(h_i + h_j)$. Because the artificial viscosity should be active only in shocks and otherwise the gas should behave like an ideal fluid Π_{ij} is zero for positive divergence of the velocities $\nabla_i v_i \geq 0$.

Energy Equation

Ideal fluid:

$$\frac{d\epsilon_i}{dt} = \sum_{j=1}^{N} m_j \left(\frac{p_i}{\rho_i^2} + \frac{p_j}{\rho_j^2} \right) (v_i - v_j)\nabla_i W(r_i - r_j, h) \tag{3.86}$$

Real fluid: In the case of a real fluid energy is transformed by viscous dissipation into heat and so there has to be added another 'source term' in the energy equation:

$$\frac{1}{2}\sum_{j=1}^{N} m_j \Pi_{ij}(v_i - v_j) \cdot \nabla_i W(r_i - r_j, h) \tag{3.87}$$

Now the energy equation for a real fluid can be written

$$\frac{d\epsilon_i}{dt} = \sum_{j=1}^{N} m_j \left(\frac{p_i}{\rho_i^2} + \frac{p_j}{\rho_j^2} + \Pi_{ij} \right) (v_i - v_j)\nabla_i W(r_i - r_j, h) \tag{3.88}$$

3.4.2 Adaptive Smoothing Length

Using a grid code, the spatial resolution of its calculations are proportional to the distance of the grid points. The same holds for the SPH method with the crucial difference that the SPH points (SPH particles) are moving with the flow. Here roots the big advantage of SPH for astrophysical purposes. If there is a converging flow, also the SPH particles will converge resulting in a SPH particle density proportional to the fluid density. So the SPH method intrinsically adapts its resolution guided by the density distribution of the fluid.

On the other hand the resolution is limited in principal by the smoothing length h, because physical fluid properties are smoothed out on its length scale. Thus, if the ability of SPH to vary its resolution is to be used to its greatest advantage, it is important to vary the smoothing length in space and time. But there are several points to consider. The first is the

error introduced by spatially varying smoothing lengths. The same process used to obtain the errors inherent in the SPH method can be applied to the equation 3.58

$$\langle f(r) \rangle \quad = \quad \int\limits_{V} f(r + r')W(r', h)dV' \tag{3.89}$$

where h now varies depending on the density of the SPH particles. It is found by several authors (Lattanzio et al. (1985), Hernquist and Katz (1989)) that the errors introduced by a varying smoothing length are again of second order in h, and hence of the same order as the errors inherent in the SPH method. An important consideration when introducing a variable smoothing length is the effect on forces between particles. Because gradient calculations are affected by the smoothing length, one crucial point is that the smoothing length be used in the calculation of the force on particle i from particle j is the same as in the calculation of the opposite force. If this is not done, momentum is not conserved. The method for this symmetrization used here (Evrard (1988), Benz (1990)) is simply to replace h in all SPH equations by

$$h_{ij} \quad = \quad \frac{h_i + h_j}{2} \tag{3.90}$$

Thus, the use of variable smoothing lengths, allows the advantages of the Lagrangian nature of SPH and the lack of a fixed grid to be used to resolve high and low-density regions simultaneously to their fullest extent. To achieve an optimum adapted smoothing length it has to be evolved in time for each SPH particle individually according to the particle's density evolution so that the number of neighbours is approximatelly constant. But what is the appropriate number of neighbours? A large number of neighbours results in a low statistical error for the smoothed quantities but causes a large computing time and low resolution because the smoothing length has to be increased. On the other side, a low number of neigbour particles causes large statistical errors but the computation is fast and the spatial resolution is high. It turns out, that (in three dimensions) a minimum of 50 neighbours is required to accurately calculate SPH quantities (Bate and Burkert (1997)) The SPH code used here tries to maintain the number of neighbours for each particle to between 5-10, 20-35, and 30-70 for one, two and three dimensions respectively. The scaling law to find the new smoothing length h required to keep the number of particles constant originally is

$$h = h_0 \left(\frac{\rho_0}{\rho} \right)^{\frac{1}{\nu}} \tag{3.91}$$

where ρ_0 and h_0 are the densities and smoothing lengths at the initialization, and ν is the number of dimensions. The problem with this scaling law is that one needs the new smoothing length to determine ρ. This dilemma can be avoided by taking the derivative of equation (3.91) to obtain

$$\frac{dh}{dt} = -\frac{1}{3}\frac{h}{\rho}\frac{d\rho}{dt} \tag{3.92}$$

Replacing the time derivative of ρ by the continuity equation yields

$$\frac{dh_i}{dt} = \frac{1}{3}h\nabla \cdot v_i \tag{3.93}$$

This equation for the change of the smoothing length can then be evolved in time as all the other physical quantities.

3.4.3   SPH Resolution Limit for selfgravitating fluids

The resolvable mass of an SPH calculation is of the order of the mass inside one smoothing length. In order to follow the fragmentation process of a collapsing cloud core properly, the local Jeans mass at every timestep and at every point of the simulation area has to be larger than twice the mass inside one smoothing length (Bate and Burkert (1997)). This condition can be used together with the formula for the Jeans mass

$$M_J = \frac{\pi^{\frac{5}{2}}}{6} \left(\frac{R}{G} \right)^{\frac{3}{2}} \left(\frac{T^3}{\rho} \right)^{\frac{1}{2}} \tag{3.94}$$

to deduce a formula for the maximum allowed density:

$$\rho_{crit} = \frac{15}{32\pi} \left(\frac{RT}{\mu G} \right)^3 \left(\frac{N}{N_{neigh} M} \right)^2 \tag{3.95}$$

Here, N is the number of SPH particles used in the simulation, N_{neigh} is the number of neighbouring particles inside the smoothing length and M is the total mass. In the case of an isothermal equation of state one can follow the collapse evolution up to density contrasts of $\nabla \rho / \rho = 10^9$ if 10^5 SPH particles are used. It is worth noting, that in the case of an adiabatic compression the Jeans mass is roughly constant. Here the SPH method is able to handle even larger density contrasts because the only limiting factor is to resolve the local Jeans mass. This is crucial for star formation calculations because the contracting gas cloud evolves through extended phases of adiabatic compression. Exhausting this advantageous feature of SPH one can follow up the collapse of a prestellar cloud with initial densities of 10^{-18}g/cm^3 over 17 orders of magnitude in density down to stellar densities of 0.01g/cm^3 as it was demonstrated by Bate (1998a).

3.5   Special features and extensions to SPH

3.5.1   Supersonic motions and Shocks

The SPH method is able to give good reproduction of shocks. The quality of the shock reproduction does not depend on the dimension of the calculation, nor is there a significant dependence on the particle distribution, as long as the particles are equally distributed along each dimension and particle interpenetration does no occur. Instead the reproduction of the shock depends mainly upon the smoothing length h of the particles, and hence in the case of variable smoothing lengths, on the particle density, as this controls the smoothing length. For values of $\alpha = 1$ and $\beta = 2$ the shock is spread over about $3h$. This spread grows further if the viscosity is increased. If the smoothing length becomes large compared to the real physical shock width, the shock is smoothed out to much and does not attain the correct conditions. As expected from how the artificial viscosity is designed, the α-viscosity is the bulk viscosity in shocks, which reduces particle velocity oscillations in the shocked gas, and hence the related oscillations in density and thermal energy. In general, to provide acceptable bulk viscosity for three dimensional simulation in which shocks can occur $\alpha \geq 1$ should be used. This results in suppressed particle velocity oscillations of no more than a few percent of the sound speed in shocks up to Mach 10. In contrast the β-viscosity is ineffective in reducing this oscillations. It becomes important at the edges of shocks where

relative particle velocities are close to the sound speed or greater and particle penetration can occur. In cases of particle interpenetration, there is a significant velocity dispersion of particles in the shock and density calculations are incorrect. All together, if particles penetrate right through the shock, the shock reproduction breaks down completely. So it is a fundamental step to adjust the β-viscosity in such a way that particle interpenetrations are suppressed sufficiently. In three dimensions a value of $\beta \geq 2$ is sufficient to stop most particle interpenetrations in adiabatic and isothermal shocks up to Mach 10. The treatment of shocks by the SPH method depending on α (bulk viscosity), β (Neumann-Richtmyer viscosity) and the dimensionality of the simulation was extensively tested by Bate1995. The tests where performed on a precursor of the code used here which is equivalent to a test of the code used here because the hydrodynamical part is identical to that of the precursor.

3.5.2 Sink particles

The opacity limit results in the formation of pressure-supported roughly spherical accreting hydrostatic cores. As these cores accrete, their central density increases, and it becomes computationally impractical to follow their internal evolution until they undergo the second collapse to form stellar cores because of the short dynamical time-scales involved. Therefore, when the central density of a pressure-supported fragment exceeds $\rho_s = 10^{-11}$ g/cm^3, a sink particle is inserted into the calculation Bate et al. (1995).

In the calculation presented here, a sink particle is formed by replacing the SPH gas particles contained within $r_{acc} = 14$ AU of the densest gas particle in a pressure-supported fragment by a point mass with the same mass and momentum. Any gas that later falls within this radius is accreted by the point mass if it is bound and its specific angular momentum is less than that required to form a circular orbit at radius r_{acc} from the sink particle. Thus, gaseous discs around sink particles can only be resolved if they have radii ≥ 15 AU. Sink particles interact with the gas only via gravity and accretion.

Since all sink particles are created from pressure-supported fragments, their initial masses are ≈ 10 M$_J$, as given by the local Jeans mass at the opacity limit for fragmentation. Subsequently, they may accrete large amounts of material to become higher-mass brown dwarfs (≤ 75 M$_J$) or stars (≥ 75 M$_J$), but *all* the stars and brown dwarfs begin as these low-mass pressure-supported fragments.

The gravitational interaction between two sink particles is Newtonian for radii $r \geq 4$ AU and is softened within this radius using spline softening. In the simulations presented here sink particles are not allowed to merge.

Replacing the pressure-supported fragments with sink particles is necessary in order to evolve the calculations far beyond the initial free fall time. However, it is not without an element of risk. If the fragments are followed up all the way down to stellar densities (as it was done by Bate (1998a)) we might find that a few of the objects that we have replaced with sink particles fragment further in the second collapse phase or merge together or are disrupted via dynamical interactions. We have tried to exclude such events by insisting that the central. density of the pressure-supported fragments exceeds ρ_s before a sink particle is created. This is two orders of magnitude higher than the density at which the gas is heated and ensures that the fragment is self-gravitating, centrally-condensed and, in practice, roughly spherical before it is replaced by a sink particle. This ensures that the fragment has evolved into a self-gravitating, centrally-condensed, roughly spherical and pressure supported core before it is replaced by a sink particle.

In theory, it would be possible for a long collapsing filament to exceed this density over a large distance, thus making the creation of one or more sink particles ambiguous. However, the structure of the collapsing gas that results from the turbulence prohibits this from occurring; no long, roughly uniform-density filaments with densities $\approx \rho_s$ form during the calculation. Furthermore, each pressure-supported fragment must undergo a period of accretion before its central density exceeds ρ_s and it is replaced by a sink particle. For example, it is common in the calculation to be able to follow a pressure-supported fragment that forms via gravitational instability in a disc for roughly half an orbital period before it is replaced. Thus, the fragments do have some time in which they may merge or be disrupted.

3.5.3   Variable Equations of State

In SPH simulations a density dependent adiabatic coefficient $\gamma(\rho)$ can be used to mimic the effects of radiative transfer and chemical reactions (Bate 1998). For densities below $\rho < \rho_1 = 5.0 \times 10^{-13}$ g/cm^3 the mean free path of photons is much larger than the size of the core. In that case radiative cooling is much faster than heating by gravitational contraction and so we can use $\gamma = 1$ (isothermal equation of state).

For $\rho > \rho_1$ the mean free paths of photons becomes shorter than the typical size of a fragment. This is called the 'opacity limit' due to the fact that at this density a typical fragment becomes opaque or optically thick resulting in a cooling timescale larger than the local free fall time. Therefor the fragment will behaves like adiabatic compressed molecular gas, $\gamma = 1.4$.

This works up to the point where the molecules start to dissociate: $\rho > \rho_2 = 6.0 \times 10^{-8}$ g/cm^3. Thermal energy now is consumed by the dissociation process resulting in a decreasing pressure support. This allows for a second collapse phase and eventually further fragmentation. Laboratory experiments suggest an adiabatic coefficient of $\gamma = 1.15$ in the dissociation regime.

After all molecules are transformed in atomic gas ($\rho > \rho_3 = 1.0 \times 10^{-3}$ g/cm^3) the core behaves adiabatically again, but now with the adiabatic coefficient for atomic gas, $\gamma = 1.15$.

Its worth noting that this approximation assumes implicitly a unique $T(\rho)$ dependence. In reality $T(\rho)$ depends also on the size and shape of the core but there is good coincidence with one dimensional frquency dependent radiative transfer calculations (figure 3.1).
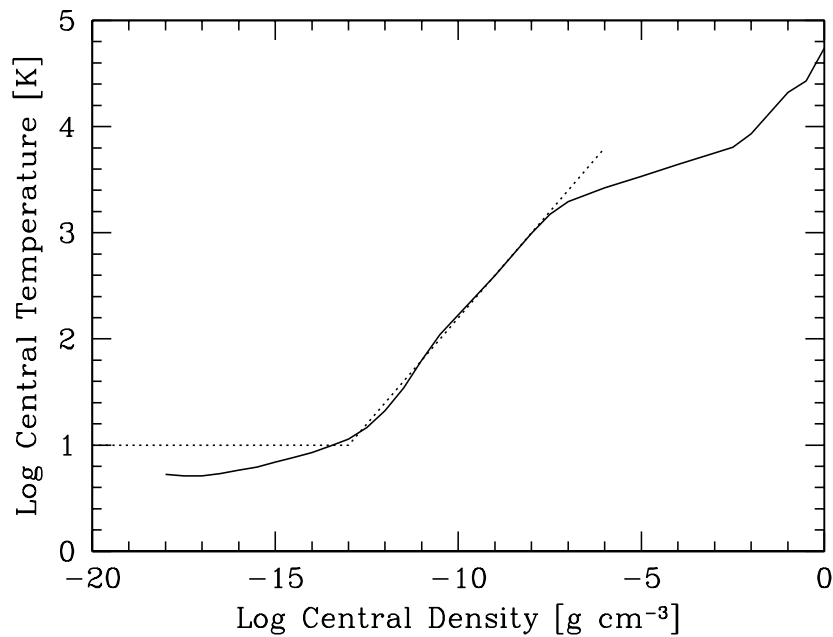
Figure 3.1: **Comparison of our variable equation of state (dotted line) with the temperature-density relation resulting from a spheric symmetric collapse calculation with frequency dependent radiative transfer (solid line; Masunaga and Inutsuka (2000). Because Masunaga and Inutsuka (2000) start with a gas sphere intially at 5K the curved differ for densities less than 10^{-14} g/cm^3. However, in the range of 10^{-13} g/cm^3 the parametrization fits the radiative transfer result very well. The second collapse phase occurs if the density exceeds 5×10^{-8} g/cm^3.**

Chapter 4

Selfconsistent Initial Conditions for prestellar cores

4.1 Artificial initial conditions

In most collapse simulations done so far artificial initial condition are used, artificial in the sense that some kind of analytical description is used to set up an initial density or velocity distribution which then directly starts to collapse. Examples are Gaussian density distributions, isothermal spheres, various polytropes, Bonnor-Ebert spheres etc. In almost all collapse calculations spherical or cylindrical symmetry is introduced at least in the initial conditions. A symmetry which is not seen in nature, see e.g. Barranco and Goodman (1998), Bacmann et al. (1998).

Even for the same density distribution and total angular momentum a different setup for the initial velocities can drive the system into a completely different collapse history. For example a supercritical Bonnor-Ebert sphere built up with static non moving gas collapses from inside out (Shu (1977)). If one adds a spherical velocity field directed inward the collapse evolves from outside in (Hennebelle et al. (2002)).

So if one wants to understand how prestellar cores evolve through the collapse phase, one has to keep in mind the large variety of prestellar core realizations in nature. The aim should be to take over nature's way of creating initial conditions as far as we known from observations (Section 2.4). One crucial feature of natural initial conditions are that they are *individual*! In the following sections I want to present a method for building up appropriate initial conditions which match typical common features of prestellar cores, but also have its individual shape and internal dynamic.

4.2 Two methods to built up Initial Conditions

We have developed and investigated two independent methods to built up initial conditions which match the observed properties of prestellar cores. The main ingredient for both methods is a velocity field which shows the typical features of turbulent flows around and in prestellar cores. This velocity field is used to built up an individual density structure out of an initially homogeneous gas distribution.

The crucial point is to inhibit the collapse long enough so that the system is able to reach a dynamical equilibrium between the evolving density and velocity structures. Both, density

and velocity structure are then consistent with each other and it is in this sense that we call this state a 'selfconsistent initial condition'. This can be reached in two ways:

- Switch of gravity, and evolve the pure hydrodynamic equations forward in time. This is easy because we only have to wait up to the point when dynamical equilibrium has been reached and the system resembles hopefully the appropriate density distribution. Unfortunately there is introduced an unphysical discontinuity when gravity switched on for the subsequent collapse calculation .

- Evolve the hydrodynamic equations with gravity, but use the turbulent velocity field itself to prevent the system from collapse for the first time. This is more advanced because here the setup has to be finetuned in a way that the collapse is inhibited at least long enough for the system to reach its dynamical equilibrium and eventually longer to adjust the resulting initial condition in a optimum way before the collapse sets in.

We have tested both methods with several random realizations for the initial velocity field but identical setup conditions. Even though the first method seem to be attractive because its easy to apply it is found to be improper. By switching on gravity in a later stage destroys the dynamical equilibrium of density and velocity field. This is simply because structures evolve essentially different with and without gravity. The second method comes out to be the more promising. Besides the big advantage of the second method that no unphysical intervention is needed to initiate the collapse it comes out that the second method reproduces the typical features of prestellar cores much better. To apply this second approach one needs a quantitative measure of turbulent support against gravity.

4.3 Appropriate Setup Conditions

The following requirements have to be fulfilled by the initial turbulent velocity field:

- the collapse does not set in before a dynamical equilibrium between density structure and velocity field has been reached

- it is consistent to the non thermal velocity dispersions and linewidth size relations observed in the vicinity of prestellar cores

- the density structures emerging during the pre collapse phase are consistent with the observed structures of prestellar cores

The fine tuning can be done by using an extended Jeans stability criteria. Following the classical jeans criteria (see section 3.2) a homogeneous density sphere of radius r and mass m is stable against small density perturbations as long as $m_{tot} \leq m_J$. But a turbulent velocity field yields an additional support against gravitational collapse. So one can define a turbulent Jeans mass by adding geometrically microscopic thermal and macroscopic turbulent velocities:

$$v_{\text{all}}^2 = v_{\text{therm}}^2 + v_{\text{turb}}^2 = v_{\text{therm}}^2(1 + M^2) \tag{4.1}$$

The Mach number M is the root mean square velocity of the turbulent motions in units of the sound speed. Interpreted as an additional internal energy

$$T_{\text{eff}} = T(1 + M^2) \qquad (4.2)$$

we can rewrite the classical equation for the jeans mass:

$$m_{\text{J,turb}} = 2.74 \sqrt{\frac{\frac{4}{3}\pi r^3 T^3}{m_{\text{tot}}}} (1 + M^2)^{\frac{3}{2}} \qquad (4.3)$$

Here r is the radius of the initial setup sphere and T the thermal gas temperature. The sphere becomes supercritical if $m_{\text{J,turb}} \leq m_{\text{tot}}$. Solving equation (4.3) for $m_{\text{J,turb}} = m_{\text{tot}} = x$ yields:

$$x = 3.16 r T (1 + M^2) \qquad (4.4)$$

Inserting typical values for prestellar cores , $M = 0.7$ (Goodman et al., 1998), $r = 0.06\,\text{pc}$ (Bacmann et al., 1998) and $T = 10\,\text{K}$ (Barranco and Goodman, 1998) one gets $x = 3\,\text{M}_\odot$. Or the other way around:

A gas sphere of $x = 3\,\text{M}_\odot$, $r = 0.06\,\text{pc}$ and $T = 10\,\text{K}$ becomes unstable if the Mach number of its turbulent velocity field drops below $M = 0.7$.

The features of our initial condition resulting from this analysis are summarized in the following table:

radius	$r = 0.06\,\text{pc}$
mass	$m = 3\,\text{M}_\odot$
temperature	$T = 10\,\text{K}$
Mach number at the onset of collapse	$M = 0.7$
thermal Jeans mass	$m_{\text{J,therm}} = 1.2\,\text{M}_\odot$
turbulent Jeans mass at the onset of collapse	$m_{\text{J,turb}} = 3.0\,\text{M}_\odot$

This resembles the scale, mean density, mass and velocity structure of a typical low mass star forming core, see Section 2.4. This analysis gives us the possibility to control the physical parameters of our initial conditions. But it is still unclear how much turbulent energy we need at the beginning to inhibit the collapse long enough. Therefore we need a method to check for the dynamical equilibrium between density and velocity field. This is described in detail in section 4.4. But first I want to focus on the principal features of turbulent velocity fields because they are one of the essential ingredients of our initial conditions. Observations of molecular clouds and prestellar cores (Larson (1969), Mac Low and Ossenkopf (2000), Ossenkopf and Mac Low (2002)) and the analysis of turbulent phenomena in general (Kolmogorov (1941)) providing strong restrictions on the structure of this velocity field.

4.3.1 The Kolmogorov Law

Think of a fluid in the limit of a very large Reynolds number or, equivalently near zero viscosity. In the case of isotropic stationary turbulence forced at a rate ϵ in a spectral range around

the wave number k_i, the energy flux from large to small scales is independent of k and equal to ϵ for $k > k_i$. As a result ϵ being also the viscous dissipation rate. This shows that ϵ is an important parameter which controls the energy flux from the large scales (small k) where the energy it is injected to the small scales where it is dissipated by viscosity. This scheme of progressive energy cascade from large to smaller and smaller sized velocity structures are nicely described by a little poem of Richardson in 1922:

Big whirls have little whirls,
which feed on their velocity,
and little whirls have lesser whirls,
and so on down to viscosity.

Kolmogorov's theory assumes that the energy at wave numbers greater than k_i depends only on ϵ and k. Due to this selfsimilar feature of the turbulent velocity field one expects the energy spectrum $E(k)$ to be a power law depending on ϵ^α and k^β:

$$E_k = \sum_{\alpha,\beta} \epsilon^\alpha k^\beta \tag{4.5}$$

A dimensional analysis can be used to find the values for the exponents α and β. One looks for exponents α and β such that the product $\epsilon^\alpha k^\beta$ has the dimension of a kinetic energy spectrum:

$$k = [L]^{-1}; E(k) = [L]^3[T]^{-2}; \epsilon = [L]^2[T]^{-3}\epsilon^\alpha k^\beta = [L]^{2\alpha-\beta}[t]^{-3\alpha} = [L]^3[T]^{-2} \tag{4.6}$$

[L] and [T] are dimensions of space and time respectively. There is only one possible solution for the pair (α, β):

$$\alpha = \frac{2}{3} \quad , \quad \beta = -\frac{5}{3} \tag{4.7}$$

With equation 4.11, this induces a power spectrum $P(k) \sim k^{-\frac{11}{3}}$ defining the distribution of the amplitudes of the velocity fluctuations on different wavelengths. This is confirmed by a wide range of turbulent phenomena on earth (e.g. Gargett et al., 1984) and in space. Myers and Gammie (1999a) suggest that most observed line width-size relations of molecular clouds and prestellar cores can be reproduced by a spectral energy law $E(k) \sim k^{-2}$ corresponding to a power spectrum $P(k) \sim k^{-4}$. Burkert and Bodenheimer (2000) also show that such a power law can reproduce the observed projected rotational properties of molecular cloud cores. These results guide the way on how we create the initial velocity fields for our calculations.

4.3.2 Gaussian Random Fields

We realize the initial turbulent velocity field of the prestellar core using Gaussian random fields. Gaussian random fields can be fixed by their mean value, in our case the root mean square (rms) velocity $\sqrt{v^2}$, and the power spectrum $P(\vec{k})$ with respect to the wave number k. The power is defined as the absolute value of the Fourier coefficients in k-space and thus determines the distribution of the amplitudes among the different wavelengths of the turbulent perturbations in $\vec{r}$-space. In the following, we will assume that the power spectrum is isotropic and follows a power law, see section 4.3.1.

Each velocity component $v_j(\vec{r})$ can be described using the Fourier expansion

$$v_j(\vec{r}) = \frac{1}{(2\,\pi)^3} \int \hat{v}_j(\vec{k})\,e^{i\,\vec{k}\vec{r}}\,d^3k \tag{4.8}$$

For $v_j(\vec{r})$ to be real, $v_j(\vec{r}) = v_j^*(\vec{r})$, the complex conjugate must obey $\hat{v}_j^*(\vec{k}) = \hat{v}_j(-\vec{k})$. The convolution theorem for Fourier transformations gives the connection between the autocorrelation function and the power spectrum $P(\vec{k}) = |\hat{v}_j(\vec{k})|^2$:

$$\int v_j(\vec{r}\,')\,v_j(\vec{r}\,' + \vec{r})\,d^3r' = \frac{1}{(2\,\pi)^3} \int P(\vec{k})\,e^{-i\,\vec{k}\vec{r}}\,d^3k \tag{4.9}$$

A measurable quantity for molecular clouds is the velocity dispersion, which is directly connected to the mean kinetic energy per mass

$$\mathcal{E}_{\text{kin}} = \frac{1}{2\,V} \int v_j(\vec{r}\,')\,v_j(\vec{r}\,')d^3r' \tag{4.10}$$

Using the above convolution theorem with $\vec{r} = 0$ and assuming an isotropic power spectrum $P(\vec{k}) = P(|\vec{k}|)$, we get

$$\mathcal{E}_{\text{kin}} = \frac{1}{2\,V} \frac{1}{(2\,\pi)^3} \int 4\,\pi\,k^2\,P(k)\,dk \tag{4.11}$$

If one measures the spectral energy, that is the energy of all the modes in the spherical shell in k-space between k and $k + dk$, the connection to the power spectrum will be given by $\hat{\mathcal{E}}(k) \sim k^2\,P(k)$.
For a realization of a Gaussian random field, we use the discretized Fourier transformation (see Equation 4.8)

$$v_j(\vec{r}) = \frac{L^3}{(2\,\pi)^3} \sum_{\vec{k}} \hat{v}_{j,\vec{k}}\,e^{i\,\vec{k}\vec{r}} \tag{4.12}$$

and assume that real and imaginary part of the Fourier coefficients $\hat{v}_{j,\vec{k}} = u_{j,\vec{k}} + i\,v_{j,\vec{k}}$ are Gaussian distributed with variance $\sigma^2 = P(k)$:

$$\mathcal{P}(u, v) = \frac{1}{2\,\pi P(k)}\,e^{-\,(u^2+v^2)/2P(k)} \tag{4.13}$$

Variable transformation to spherical coordinates gives a uniform probability density function for the phase ϕ

$$\mathcal{P}(\phi) = \frac{1}{2\,\pi} \tag{4.14}$$

and the Rayleigh distribution for the amplitudes w of the Fourier coefficients $\hat{v}_{j,\vec{k}} = w(\cos\phi + i\,\sin\phi)$:

$$\mathcal{P}(w) = \frac{w}{P(k)}\,e^{-\,w^2/2\,P(k)} \tag{4.15}$$

This leads to the probability function $\mathcal{P}(X < w) = \int_{-\infty}^{w} \mathcal{P}(w)$ or

$$\mathcal{P}(X < w) = e^{-\,w^2/2\,P(k)} \tag{4.16}$$

with maximum at $w = \sqrt{P(k)}$. While ϕ is equally distributed between $[0, \ldots, 2\pi]$, the discrete values for w can be derived by throwing a dice to get random numbers $\mathcal{P}(X < w)$ with $0 < \mathcal{P}(X < w) < 1$ and using

$$w = \sqrt{-2 \ln(\mathcal{P}(X < w))\, P(k)} \tag{4.17}$$

4.3.3 Boundary Conditions

We have tested two different types of boundary conditions in combination with our homogeneous density sphere setup condition:

- Reflective constant volume boundaries with ghost particles

- Constant pressure boundaries. Beyond the margins of the initial gas sphere there is added a virtual pressure, equivalent to the thermal pressure inside the homogeneous sphere. To escape from the original sphere the SPH particles have to overcome this virtual pressure potential.

To apply the stability criteria described in section 4.3 it is necessary that the the mass is restricted to some well known area. This is not the case when we use constant pressure boundaries. The setup mean kinetic energy is at least twice as large as at the onset of the collapse. So that a part of the gas (about 20 percent) is splattered out of the initial sphere. This causes an additional stabilisation of the cloud and it is not possible any more to define a global stability parameter. So its hard in combination with constant pressure boundaries to predict if and when the collapse sets in. Therefore it comes out, that the constant volume boundaries are the appropriate boundary condition for our purposes because they allow a easy way to control the stability conditions.

4.4 A Test for Selfconsistency

As already mentioned in section 4.3 we have to check for the dynamical equilibrium between density and velocity field. If we start our calculations with a setup condition as described in section 4.3 then in the beginning density fluctuations are built up by the turbulent velocity field, see figure 4.1. This corresponds to a flow of kinetic energy into potential energy. After some time the system reaches a dynamical equilibrium between the energy stored in density fluctuations and the energy stored in the turbulent velocities. Here the density fluctuations $\Delta\rho/\rho$ reach a local maximum.

At this point a consistency between energy and velocity field has been reached so that they are naturally connected to each other. It is in this sense that we call this constellation selfconsistent. As a result the decay of the velocities decelerates significantly because now the velocity field looses energy only by dissipation so that density fluctuations and velocities decay simultaneously. After some time the decay of density fluctuations stops, indicating that the evolved structure becomes unstable and start to collapse. In figure 4.1 the wavelength of the largest mode of the turbulent velocity field is one fifth ($0.24\,\mathrm{pc}$) of the spheres diameter. This results in a shorter timescale for the viscous dissipation. One can easily see the 'built up phase' and 'selfconsistent dissipation phase' separated by a maximum in $\Delta\rho/\rho$. For a more realistic run the largest mode should have the same size as the setup sphere. In this case

the viscous timescale is much larger and there will be no maximum in $\Delta\rho/\rho$. What remains is a plateau like phase between the gain of dynamical equilibrium and the onset of collapse, compare figure 5.1. So that it is still possible to check for the selfconsistency.

Figures 4.2 and 4.3 showing the evolution of $\Delta\rho/\rho$ for initial Mach numbers 1.0, 1.5, 2.0, 2.5, 3.0 and 4.0. One sees that there is only a weak depencence of the local maximum of $\Delta\rho/\rho$ on the initial Mach number. This implies that the dynamical equilibrium is reached always routhly at the same time. In contrast to that the onset of collapse is significantly delayed from 130000yrs for an initial Mach number of $M_0 = 1.0$ to 165000yrs for $M_0 = 4.0$.

But there is an additional interesting feature in the time evolution of $\Delta\rho/\rho$ concerning its local minimum. This local minimum is reached when the $\Delta\rho/\rho$ amplification by gravity start to overbalance the damping by viscosity. By looking carefully on the minimum values of $\Delta\rho/\rho$ for the six panels in figure 4.2 and 4.3 one sees that it is growing from $\Delta\rho/\rho = 0.6$ when an initial Mach number of $M_0 = 1.0$ is used to $\Delta\rho/\rho = 0.95$ for $M_0 = 4.0$. This is surprising because our initial condition was designed to become instable only when $M(t) < 0.7$. In addition density and velocity fields were checked to be in an dynamical equilibrium.

To solve this puzzle we looked for the actual Mach numbers $M(t = t_{\Delta\rho/\rho|_{min}})$ when the minimum in $\Delta\rho/\rho$ is reached. It comes out that also the Mach numbers $M(t = t_{\Delta\rho/\rho|_{min}})$ tend to be larger if the initial Mach number $M(t = 0)$ is increased. This means that the amplitudes of the density fluctuations from which the core evolves into the collapse phase must be larger if the initial Mach number is increased. In prinziple, there is a large variety of marginaly stable constelations. Strong density condensations need more turbulent pressure to be supported. As a result they collapse earlier. This implies, that in the case of high initial Mach numbers more kinetic energy is conveyed into the isothermal collapse process. This increases the probability for fragmentation events and a higher frequency of multiple systems is expected.
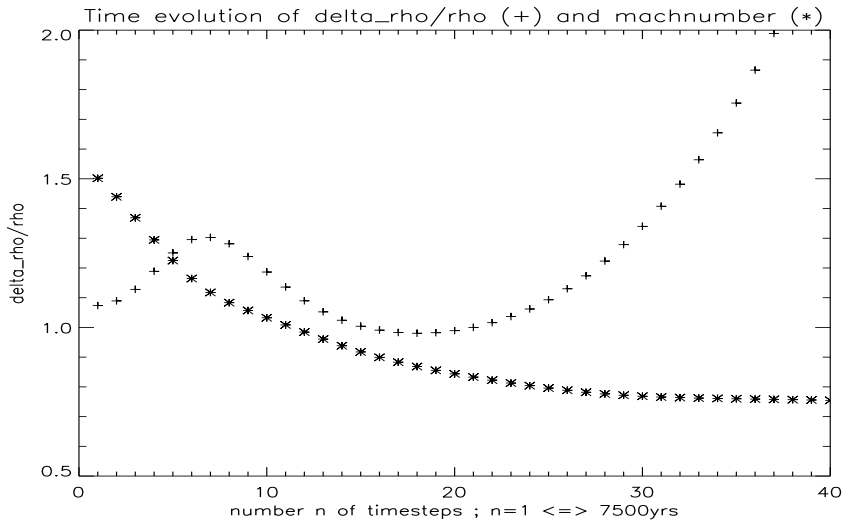
Figure 4.1: **Time evolution of the density fluctuations $\Delta\rho/\rho$ (crosses) and the Mach number M (stars) for an initial Mach number of $M_0 = 1.5$. The wavelength of the largest mode of the turbulent velocity field is one fifth $(0.24\,\mathrm{pc})$ of the spheres diameter.**

- $t < 0.7 \times 10^5\,\mathrm{yrs}$: density fluctuations are built up by the turbulent velocity field

- $t = 0.7 \times 10^5\,\mathrm{yrs}$: selfconsistency has been reached

- $t < 1.5 \times 10^5\,\mathrm{yrs}$: turbulence and density fluctuations are decaying simultaneously

- $t = 1.5 \times 10^5\,\mathrm{yrs}$: the core becomes supercritical $(M = 0.85)$

- $t > 1.5 \times 10^5\,\mathrm{yrs}$: the core runs into an isothermal collapse
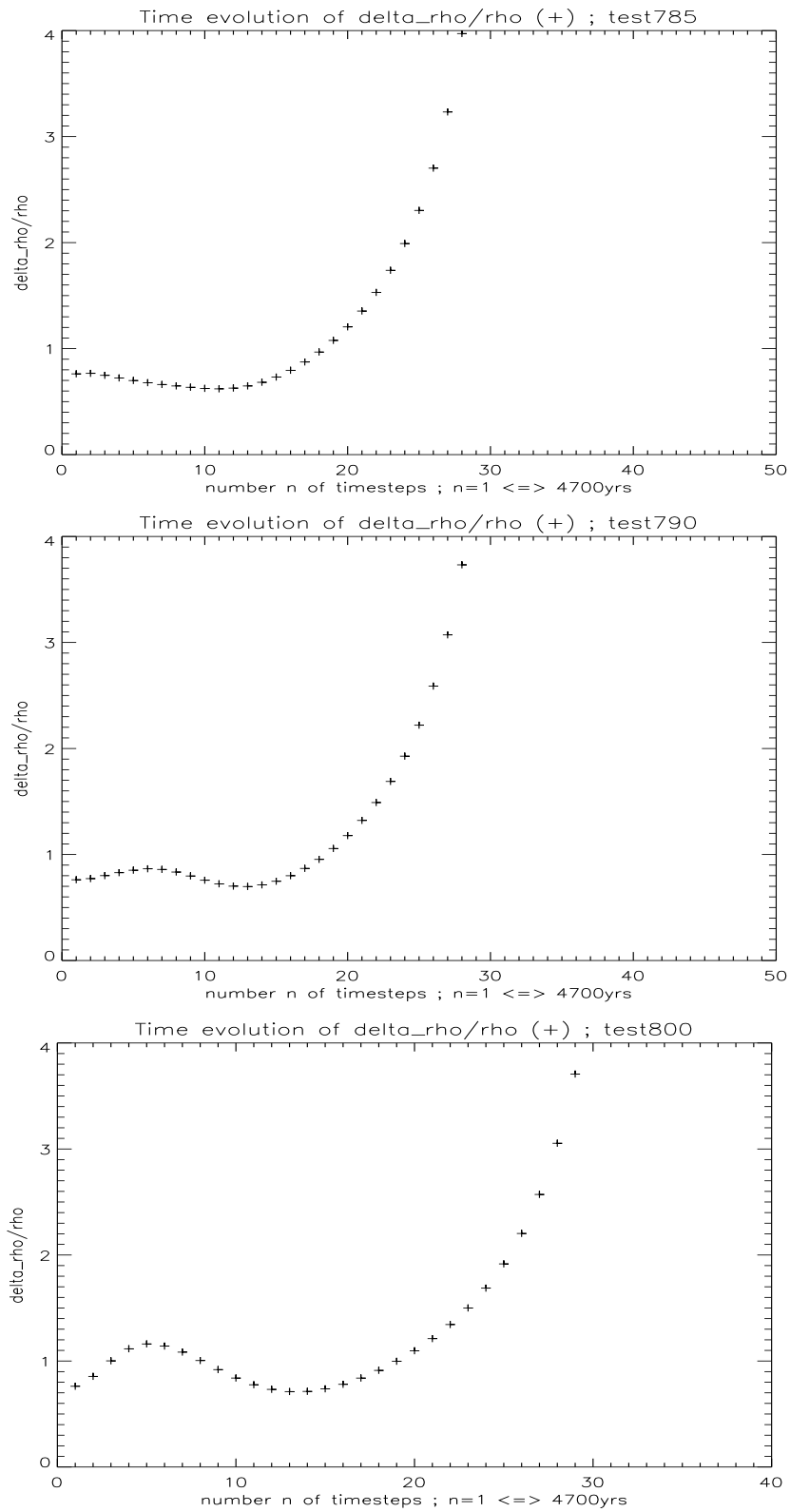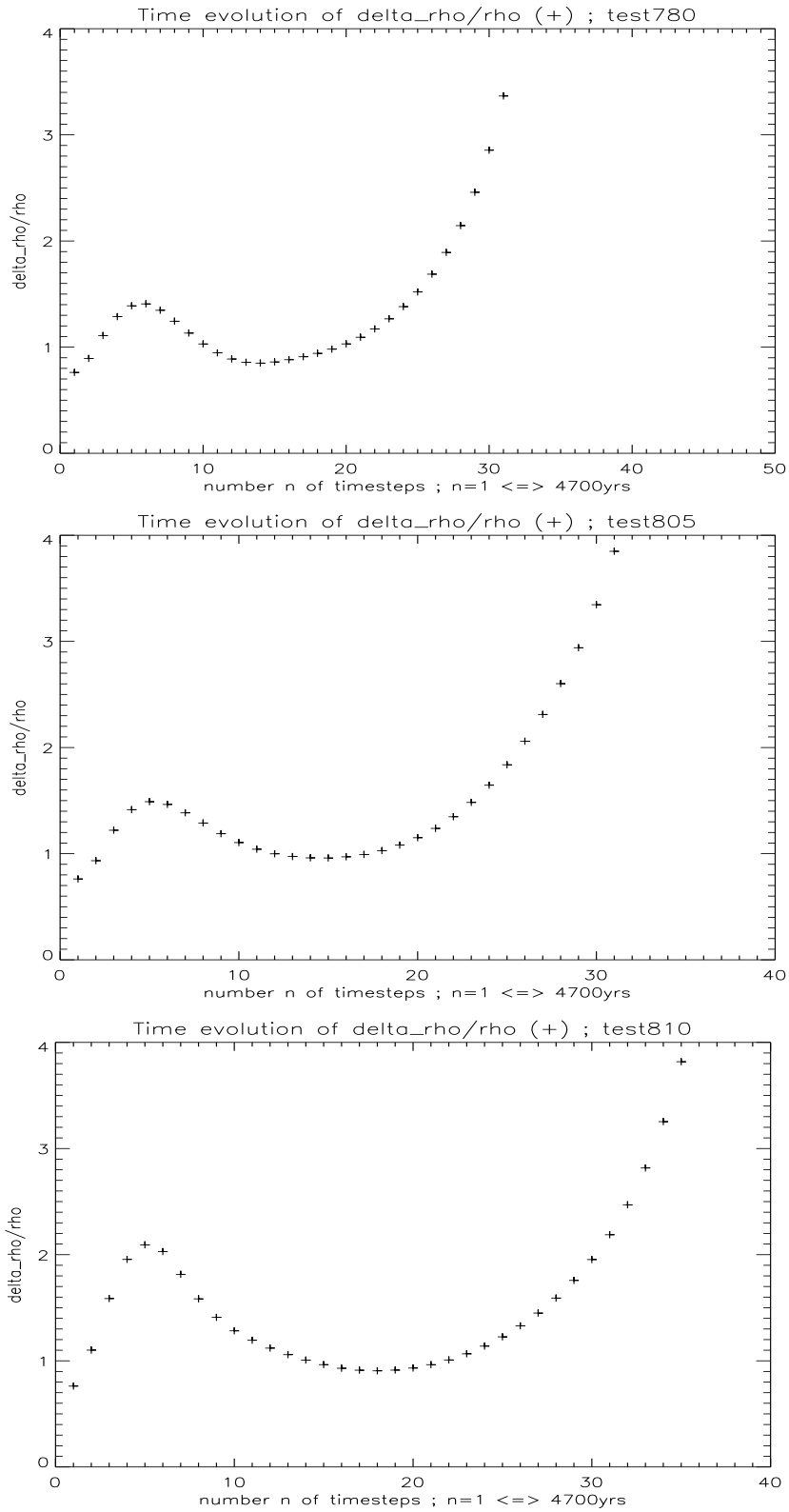
Figure 4.2: **Time evolution of $\Delta\rho/\rho$ for initial Mach numbers of $M_0 = 1.0$ (top panel),** $M_0 = 1.5$ **(middle panel) and** $M_0 = 2.0$ **(lower panel). The wavelength of the largest mode of the turbulent velocity field is one fifth** $(0.24\,\mathrm{pc})$ **of the spheres diameter.**

Figure 4.3: **Time evolution of** $\Delta\rho/\rho$ **for initial Mach numbers of** $M_0 = 2.5$ **(top panel),** $M_0 = 3.0$ **(middle panel) and** $M_0 = 4.0$ **(lower panel). The wavelength of the largest mode of the turbulent velocity field is one fifth** $(0.24\,\mathrm{pc})$ **of the spheres diameter.**

Chapter 5

How Turbulence Creates a Gravitating Center

We have studied in detail how a gravitationally bound structure emerges in a turbulent media. In the first 40000-60000 yrs density fluctuations are built up until a dynamical equilibrium is reached between the turbulent energy on the one side and the potential energy of the density fluctuations on the other side (section 4.3). In this sense, a selfconsistent state is reached in which density and velocity field are naturally related to each other. After this first growth phase the value for the maximum density stays roughly constant over 80000-100000 yrs. Whereas the amount of mass accumulated in over-dense regions increases rapidly. Roughly 150000 yrs after the initialization the maximum density starts to increase rapidly and the core evolves into a runaway collapse.

5.1   Evolving Structures: Global Features

To get a first global impression on how turbulence and gravity distributes matter one can look up the SPH particles density distribution. Therefore the standard deviation $\Delta\rho$ in units of the mean density $\langle\rho\rangle$ is used:

$$\frac{\Delta\rho}{\rho} \quad = \quad \frac{\sqrt{\langle\rho^2\rangle - \langle\rho\rangle^2}}{\langle\rho\rangle} \tag{5.1}$$

To get an impression on how gravity change things in the regime where turbulence supports the gas against collapse the evolution of two identical setups were compared (figure 5.1). The first (upper panel) was evolved with gravity, the second (lower panel) without gravity. One sees, that during the first 40000 yrs the evolution of $\Delta\rho/\rho$ is nearly the same for both runs. If gravity is present $\Delta\rho/\rho$ is always growing but with a clear and extended plateau phase of only weakly growing density maxima. Without gravity density fluctuations start to decay when the dynamical equilibrium is reached. In contrast to the simulations shown in section 4.4 the largest mode of the initial turbulent velocity field has the same size as the setup sphere.

Figure 5.3 gives a direct impression how much mass is accumulated in over-dense regions. Shown is the number of SPH particles exceeding some certain density threshold as a function of time for run410. The uppermost line corresponds to a density threshold of 20. For the next lower line the threshold is increased by 10 units and so on for the other lines. Thick lines mark density thresholds of 50,100 and 150. The initial mean density is $\rho_0 = 3$ which corresponds to
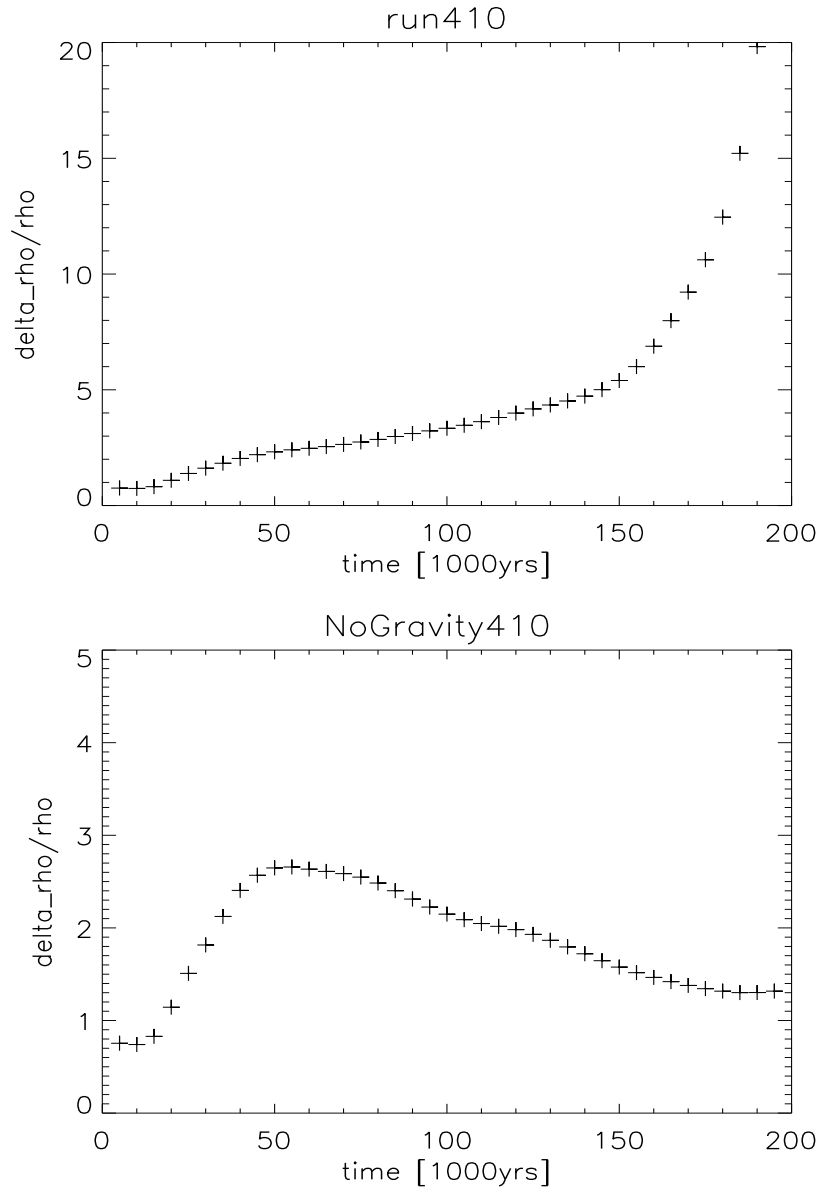
Figure 5.1: **Time evolution of $\frac{\Delta\rho}{\rho}$. Upper panel: density fluctuations as a function of time for an individual run with gravity and an initial Mach number $M = 2$. Lower panel: the same calculation as in the upper panel but without gravity.**

2×10^{-19} g/cm^3 resp. 5×10^4 molecules/cm^3. For comparison the same analysis is shown for the calculation without gravity. In this reference simulation the mass sited in 10:1 over-dense regions reaches a maximum 40000 yrs after initialization. At this time only about $0.03\,M_\odot$ (1 percent of the total mass) is hosted in this condensations. The corresponding local Jeans mass for an $10\,\rho_0$ condensation is about $0.4\,M_\odot$ which is at least one order of magnitude more than the available high density gas. In other words, the turbulent velocity field at its own is not able to drive the system into a supercritical state. This means, even if the system is strong subcritical, gravity must influence significantly the growth of density structures. Otherwise it would be impossible to evolve the low mass condensation into a supercritical core collapsing on its free fall time scale. After 100000 yrs almost all 10:1 fluctuations are gone. The dissipation results in a loss of mass for all shown density thresholds. Not surprising, high density contrasts vanish faster than the others.

Gravity affects also the velocity field. This can be seen in figure 5.5. Again there is compared run410 and the reference simulation without gravity. It shows the evolution of the Mach number in time. The Mach number concerning all SPH particles of a simulation is given by the (+) signs. The Mach number of a local subsample of SPH particles less than 1000 AU around the density maximum is indicated by the thin line (upper panel). Note that in this case the velocity of the density maximum is subtracted form the particles individual velocities because this velocity component can't contribute to a turbulent pressure on this local scale. After 1.6×10^5 yrs the acceleration of the SPH particles is clearly visible. For the total sample of particles this effect is already seen after 100000 yrs.

Comparing the global Mach numbers for the upper and lower panel, one sees that the kinetic energy decays faster in the simulation without gravity, at least 40000 yrs after the initialization the effect is obvious. In the regime $t < 60000$ yrs density fluctuations $\Delta\rho/\rho$ are a bit larger for the run without gravity. One may argue that in this case more kinetic energy is used up to built up the density fluctuations. But the opposite is the case when the dynamical equilibrium has been reachen. In the regime $t > 60000$ yrs density fluctuations *and* Mach numbers are larger if gravity is present. This can be understand by looking on how we have designed the setup conditions of the runs (section 4.3). The thermal Jeans mass of our set up is $1.2\,M_\odot$ - only about 40 percent of the total mass so that this state is Jeans unstable and would immediately collapse without turbulent pressure support. This means that every deviation from the homogeneous distribution of matter is accompanied by a decrease in potential energy. Density fluctuations are in this case a *source* of kinetic energy even though the system is still supported against gravity!

Because the over-dense regions are for the first time significantly less massive than the local Jeans mass they are supported against gravity by thermal pressure and further compression is suppressed for the first time. This can be seen in figure 5.2 where we have plotted the time evolution of the density maximum of an individual condensation and the total density maximum of the whole simulation area. One sees that the total density maximum increases only about a factor of two in the epoch between 30000 yrs and 150000 yrs after the initialization. While the condensations are supported by thermal pressure on small scales the large scale structure is already Jeans unstable and only supported by the turbulent pressure. This cooperation of thermal pressure support on small scales and turbulent support on the large scales results in a slow accumulation of mass onto the initial low mass condensations. This

behavior is in some sense similar to the adiabatic collapse phase beyond the opacity limit. In both cases there is a pressure supported core like structure on small scales which increases only slowly its density while significantly growing in mass.

In addition there is another significant difference compared to the classical isothermal collapse phase. During the isothermal collapse phase the Jeans mass decreases and a single initial object eventually fragments into two ore more objects. During the turbulence dominated contraction phase things are vice versa. The initially separated low mass condensations grow in mass, merge and form an extended over-dense object (figure 5.4). This yields a naturally explanation for the flat inner parts of prestellar cores as they are observed in turbulent star forming regions (section 2.4.1).

Altogether the turbulence dominated contraction phase has to be established as an important additional collapse phase where things are essentially different than in the isothermal collapse phase.

The turbulent kinetic energy results in a turbulent pressure increasing the amount of mass supported against gravity (section 4.3):

$$m_{\mathrm{J,turb}} = 2.74 \sqrt{\frac{T^3}{\rho}} (1 + M^2)^{\frac{3}{2}} \tag{5.2}$$

Here the density is given in units of $1\,\mathrm{M_\odot/pc^3}$ and a mean molecular weight $\mu = 2.36$ is assumed. So we can expect that mass accumulations would not fragment below $m_{\mathrm{J,turb}}$. Given a minimum Mach number of $M = 1.5$ (figure 5.5) and a density enhancement of 10, $m_{\mathrm{J,turb}}$ comes out to be $2.2\,\mathrm{M_\odot}$ which is a bit less then the total mass but still enough to prevent fragmentation during the turbulence dominated contraction phase. Once an extended over-dense region has formed the turbulent energy is dissipated on the local dynamical timescale which is about 50000 yrs and significantly shorter than in the surrounding low density regions. The turbulent pressure support breaks down and the over-dense region evolves into a rapid isothermal collapse.

To be sure, that this behavior is not a feature of an individual run we have calculated an evolutionary mean for 10 independent runs with individual initial conditions (figure 5.6). The physical parameters of the initial conditions are identical. Only the random seeds for the velocity fields were chanced. When the dynamical equilibrium is reached (roughly 40000 yr after the initialization) only less than 1 percent of the total mass is accumulated in regions with densities of more than $10\,\rho_0$. About 10^5 yrs ($0.6\,\mathrm{tff}$) later the amount of mass in the over-dense regions is at least 10 times larger and in the range of 10 to 20 percent of the total mass. At the same time the amplitude of the fluctuations stays roughly constant or increases weakly but always less than a factor of two.

The action of the turbulent pressure support results in the fact, that the Jeans instability evolves from outside in. This is shown in figures 5.7, 5.8, 5.9, 5.10. There was compared the accumulated mass inside a sphere of radius r around the density maximum (thick line) with the corresponding local Jeans mass as calculated from the mean density inside this sphere (thin line). All this is shown as a function of time. The accumulated mass inside the sphere starts to exceed the local Jeans mass when the thick line crosses the thin line. This happened first for the largest sphere and last for the smallest sphere.

The times at which the different sized spheres becomes Jeans unstable are plotted as a function of the radius r in figure 5.10. This clearly shows that the Jeans instability is created for the first time on a size scale equivalent to the size of the whole over-dense region and then evolves inward. In this sense one can say that during the turbulence dominated contraction phase the matter collapses from outside in resulting in a density distribution with a flat inner part.

This interpretation is confirmed by the radial net acceleration of the gas - the difference between the inward directed gravitational force and the outward directed pressure gradient force. Both forces were calculated in shells around the density maximum. this is shown in figures 5.11 and 5.12. One sees that there is a net outward acceleration for $t \leq 120000$ yrs for the innermost 0.004 pc. This outward acceleration becomes overbalanced by the rampressure of inward streaming gas (section 5.3) so that the center is slowly increased in density. The region of the strongest inward acceleration evolves from *outside in* (figure 5.12). At the onset of the isothermal collapse phase it reaches the center.
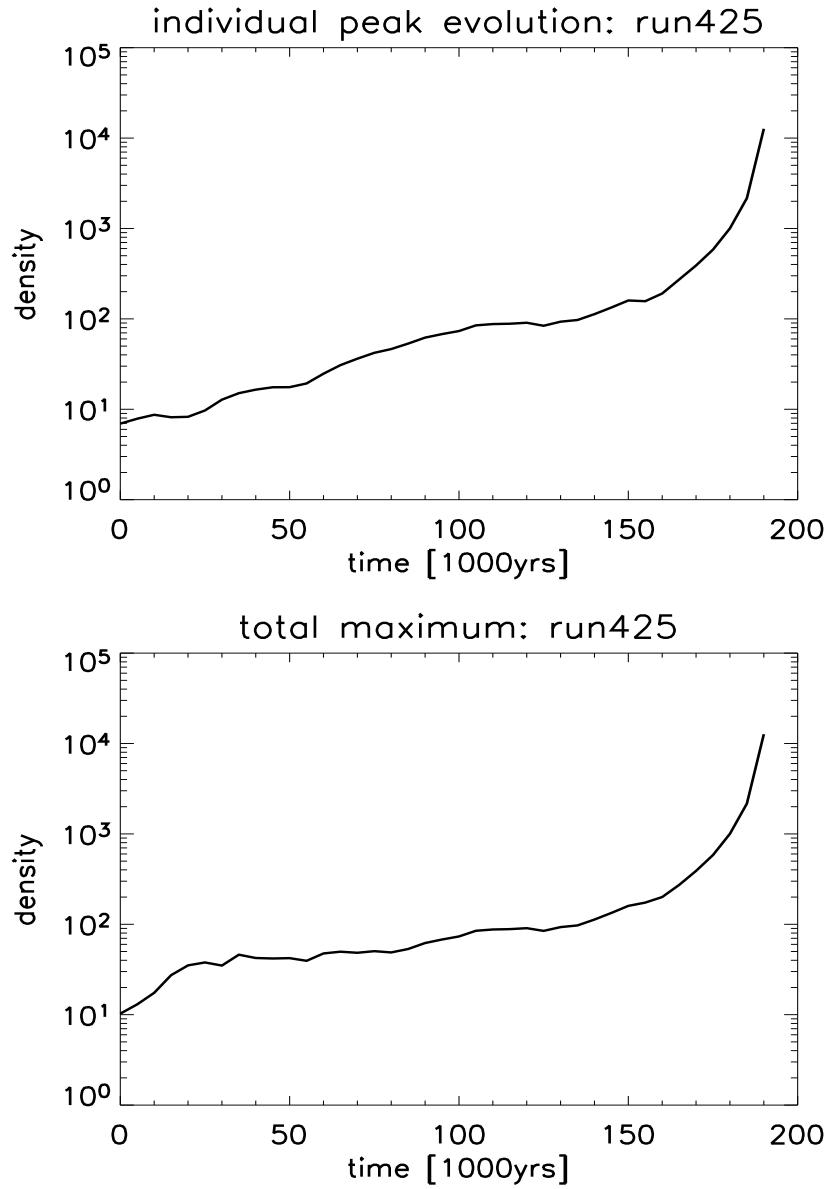
Figure 5.2: **Time evolution of the density maximum of an individual condensation evolving into collapse (upper panel) and the total density maximum in the whole simulation area. 10^5 yrs after the initialization both curves are identical.**
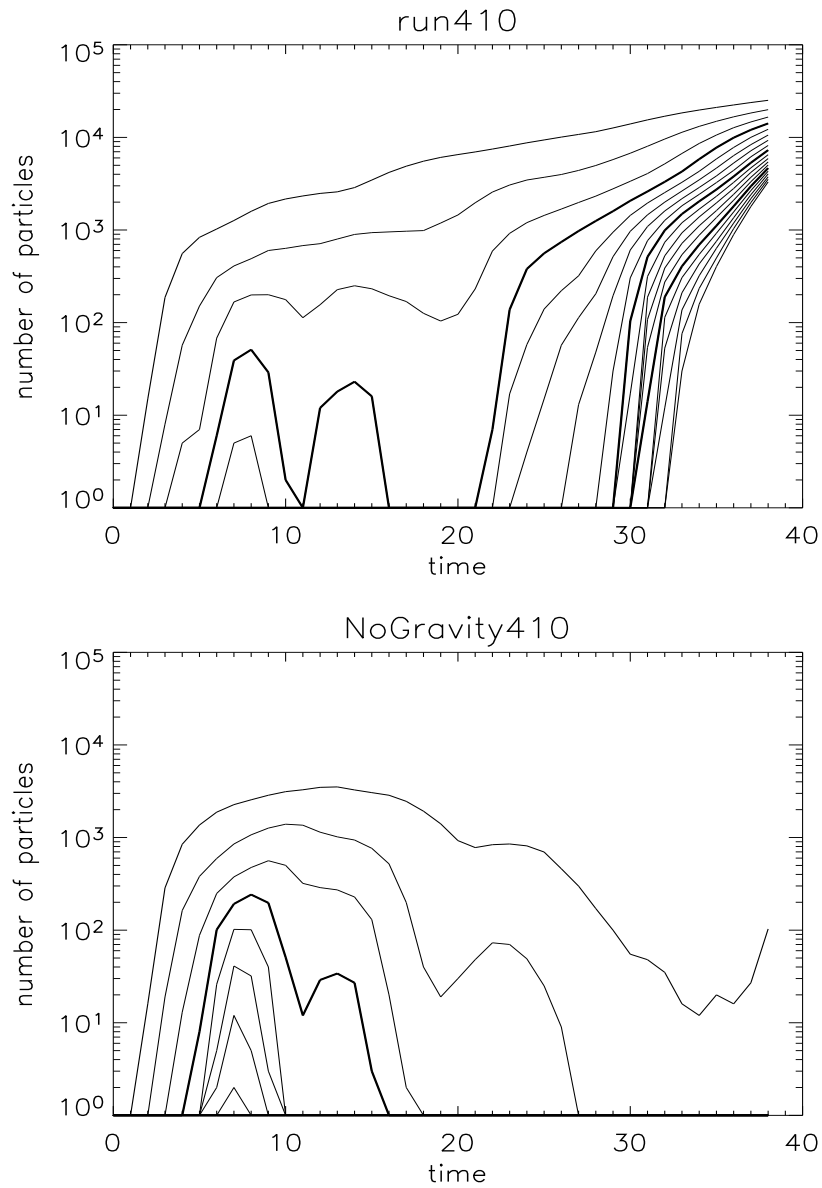
Figure 5.3: **Upper panel: Time evolution of the number of SPH particles exceeding some certain density threshold for an individual run. The uppermost line corresponds to a density threshold of 20. For the next lower line the threshold is increased by 10 units and so on for the next lines. Thick lines mark density thresholds of 50,100 and 150. The initial mean density is 3 which corresponds to 2×10^{-19} g/cm^3 resp. $5 \cdot 10^4$ molecules/cm^3. Lower panel: Comparative calculation without gravity. The initial conditions are identical to that of run410 in the upper panel.**
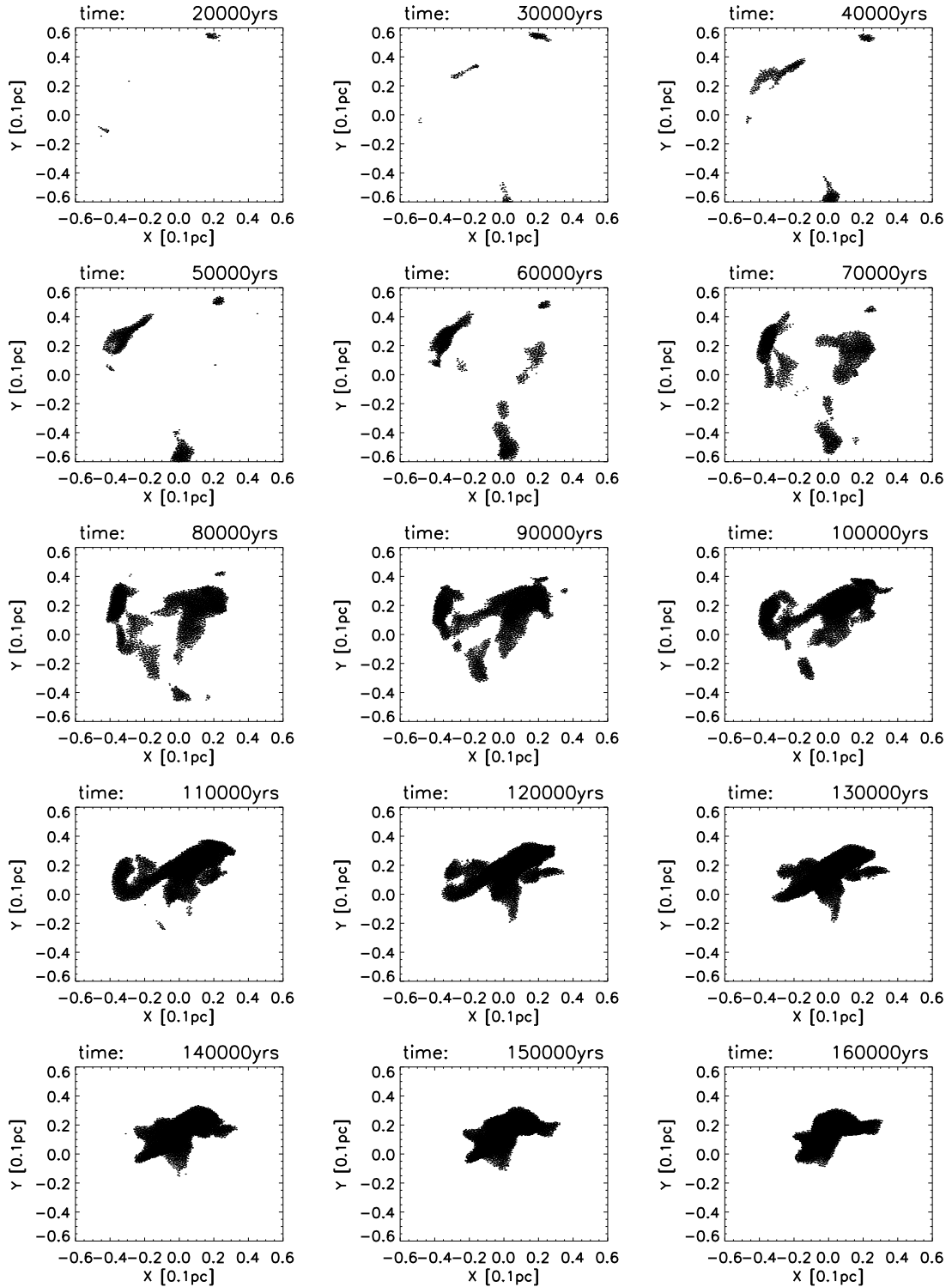
Figure 5.4: **Spatial distribution of the SPH particles exceeding a density threshold of 20 respective** $1.3 \times 10^{-18}\,\mathrm{g/cm^3}$ **, compare with figure 5.3 uppermost line. Time increases from left to right and from top to bottom. During the epoch from** $50000\,\mathrm{yrs}$ **to** $150000\,\mathrm{yrs}$ **the maximum density increases only by a factor of two while the number of particles exceeding the threshold increases by a factor of at least 10.**
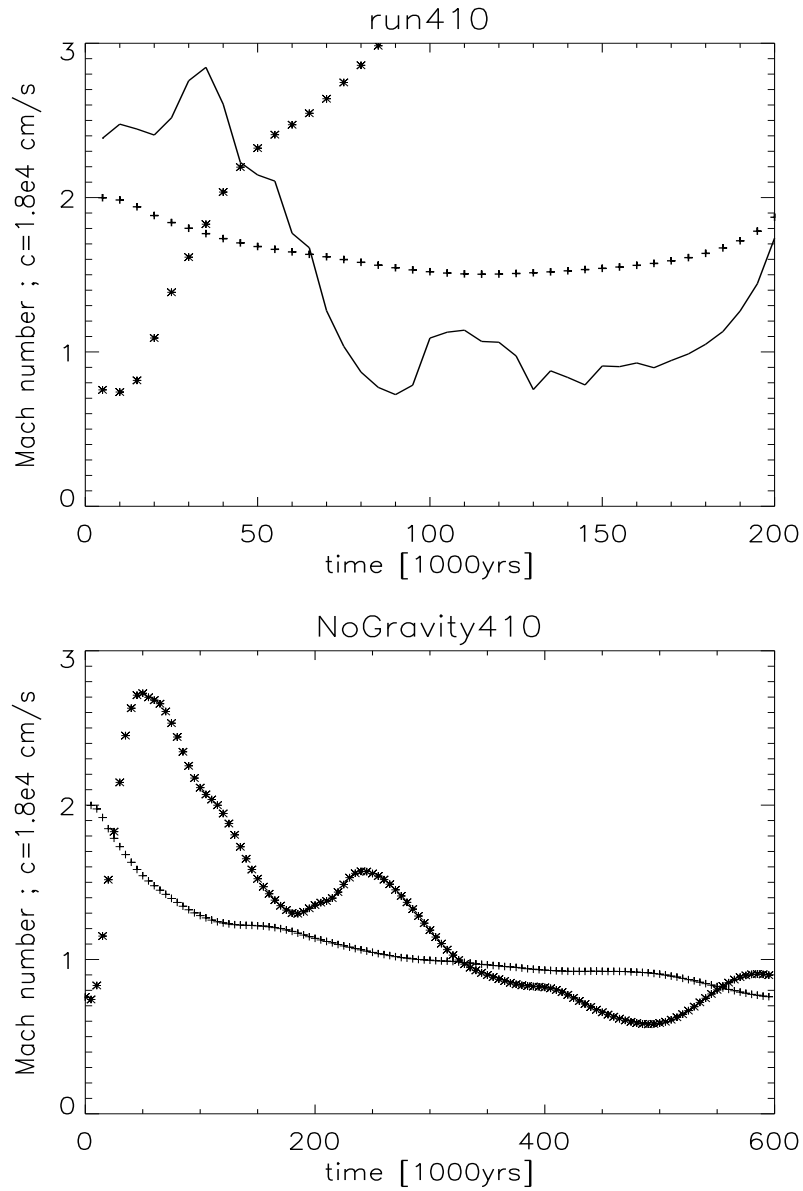
Figure 5.5: **Upper panel: Evolution with gravity. Mach number based on all particles of the simulation (+), Mach number of all SPH particles inside a sphere of** $1000\,\mathrm{AU}$ **around the density maximum (thin line) and density fluctuations** $\Delta\rho/\rho$ **(∗). Lower panel: Evolution without gravity. Mach number based on all particles of the simulation(+) and density fluctuations** $\Delta\rho/\rho$ **(∗).**
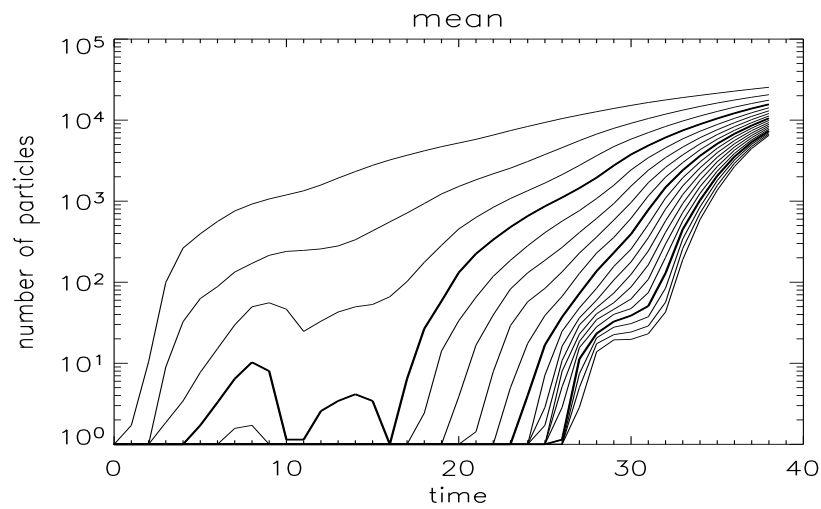
Figure 5.6: **Time evolution of the number of SPH particles exceeding some certain density threshold. Plotted is the evolutionary mean value of 10 independent runs with individual turbulent velocity field but identical physical parameters. The uppermost line corresponds to a density threshold of 20. For the next lower line the threshold is increased by 10 units and so on for the next lines. Thick lines mark density thresholds of 50, 100 and 150. The initial mean density is 3 which corresponds to $2 \times 10^{-19} \, \text{g/cm}^3$ resp. $5 \times 10^4 \, \text{molecules/cm}^3$.**
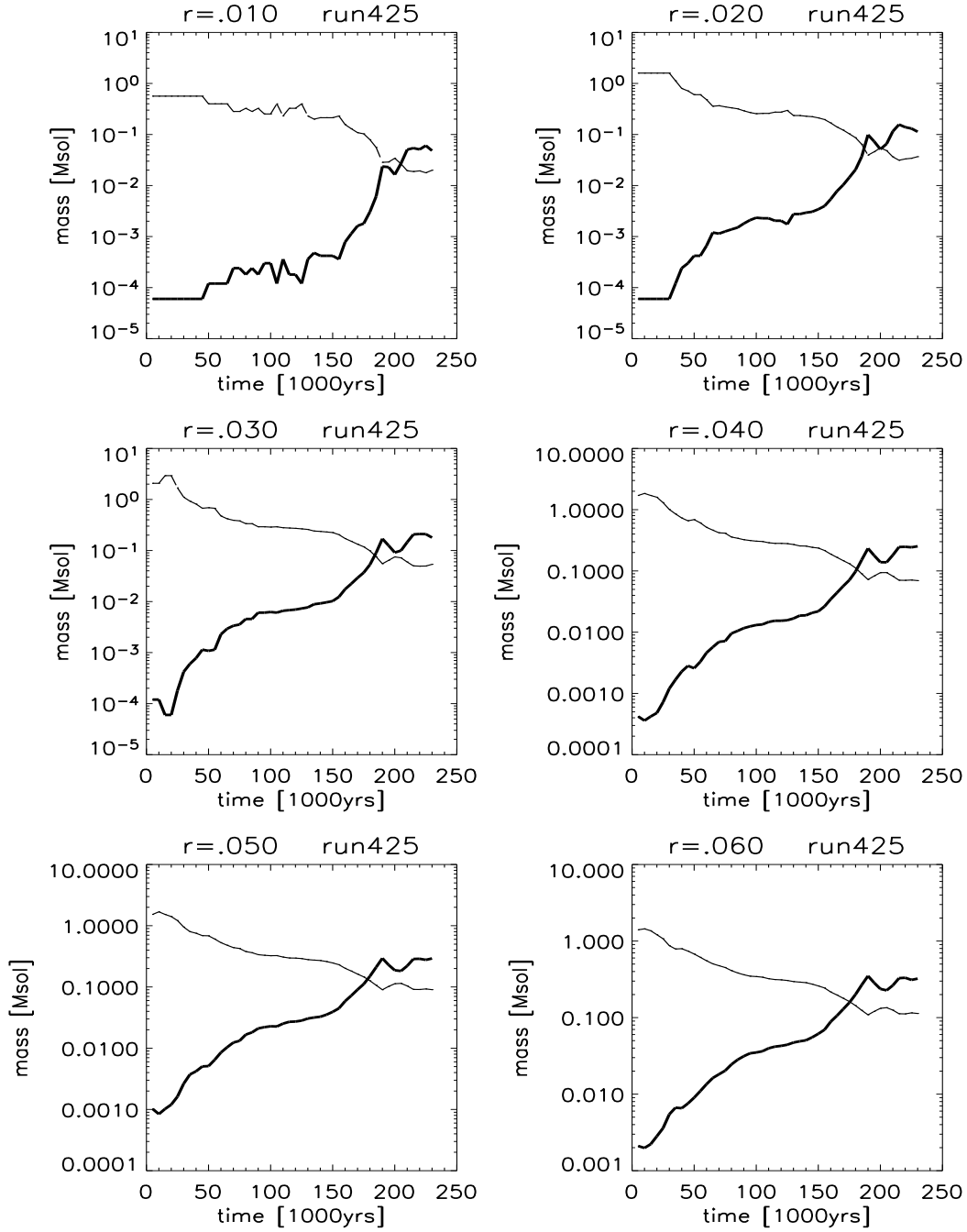
Figure 5.7: **Accumulated mass inside a sphere of radius r around the density maximum (thick line) and the corresponding local Jeans mass calculated from the mean density inside this sphere (thin line) as a function of time. Radius data is given in units of $0.1\,\mathrm{pc}$.**
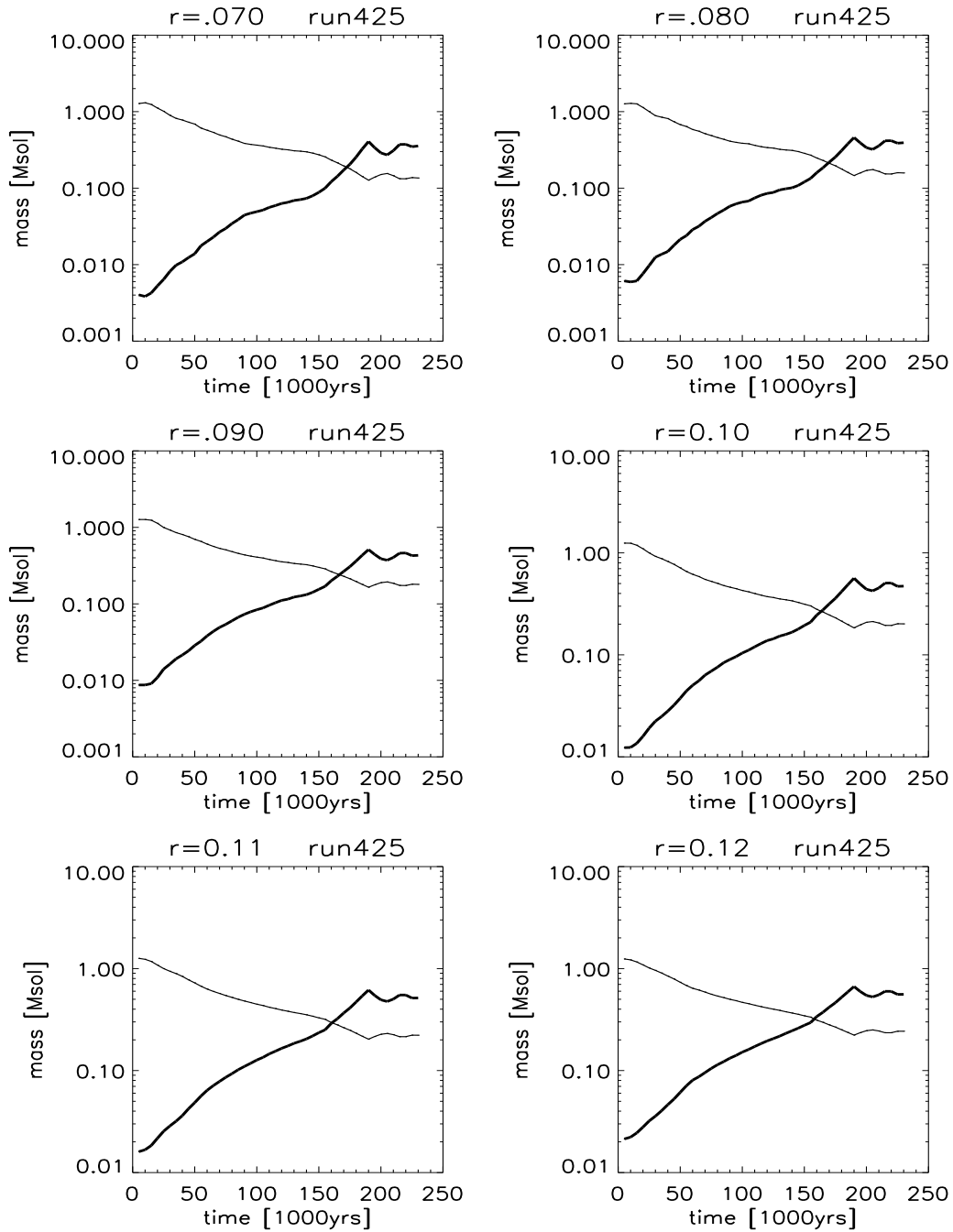
Figure 5.8: **Accumulated mass inside a sphere of radius r around the density maximum (thick line) and the corresponding local Jeans mass calculated from the mean density inside this sphere (thin line) as a function of time. Radius data is given in units of $0.1\,pc$.**
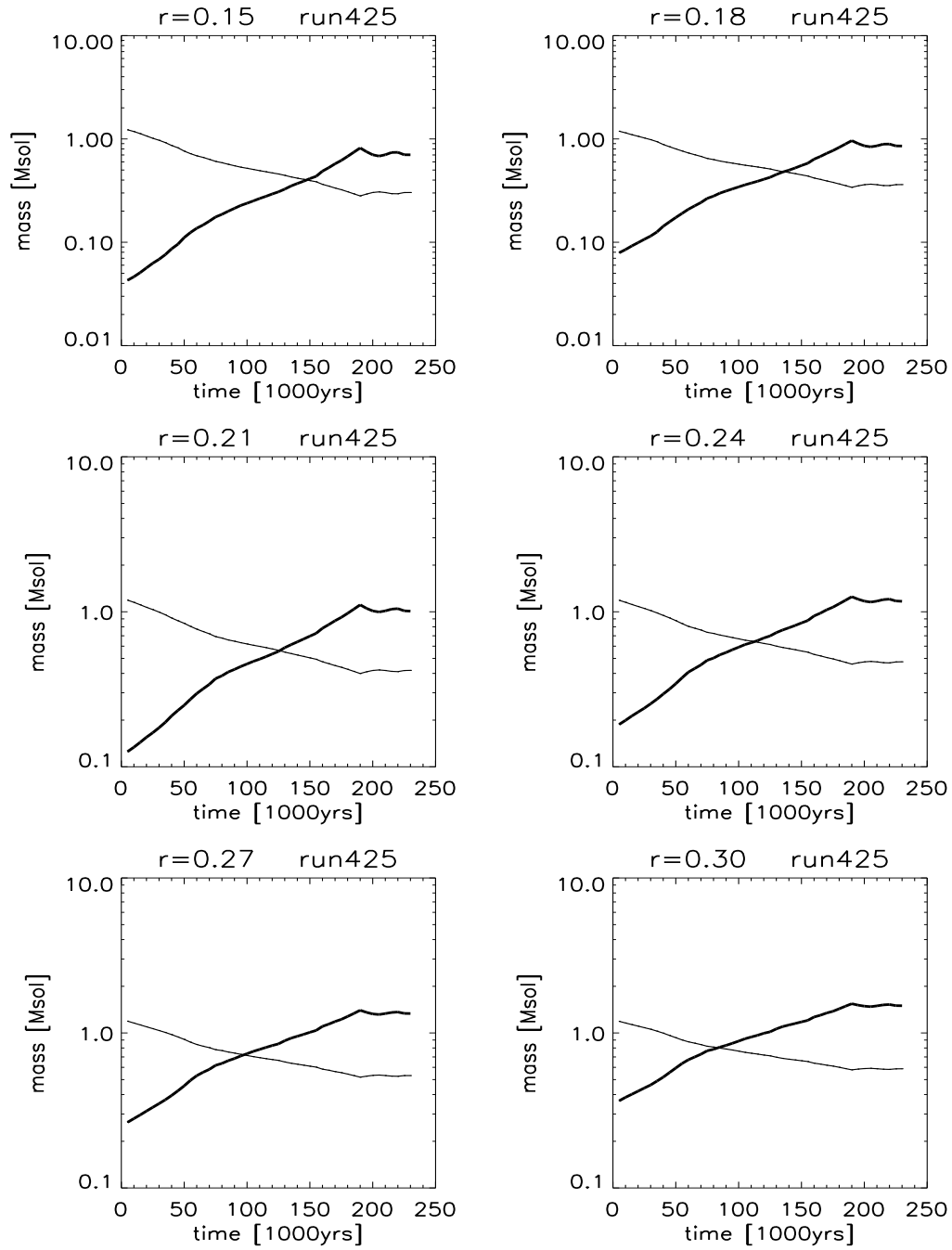
Figure 5.9: **Accumulated mass inside a sphere of radius r around the density maximum (thick line) and the corresponding local Jeans mass calculated from the mean density inside this sphere (thin line) as a function of time. Radius data is given in units of $0.1\,\mathrm{pc}$.**
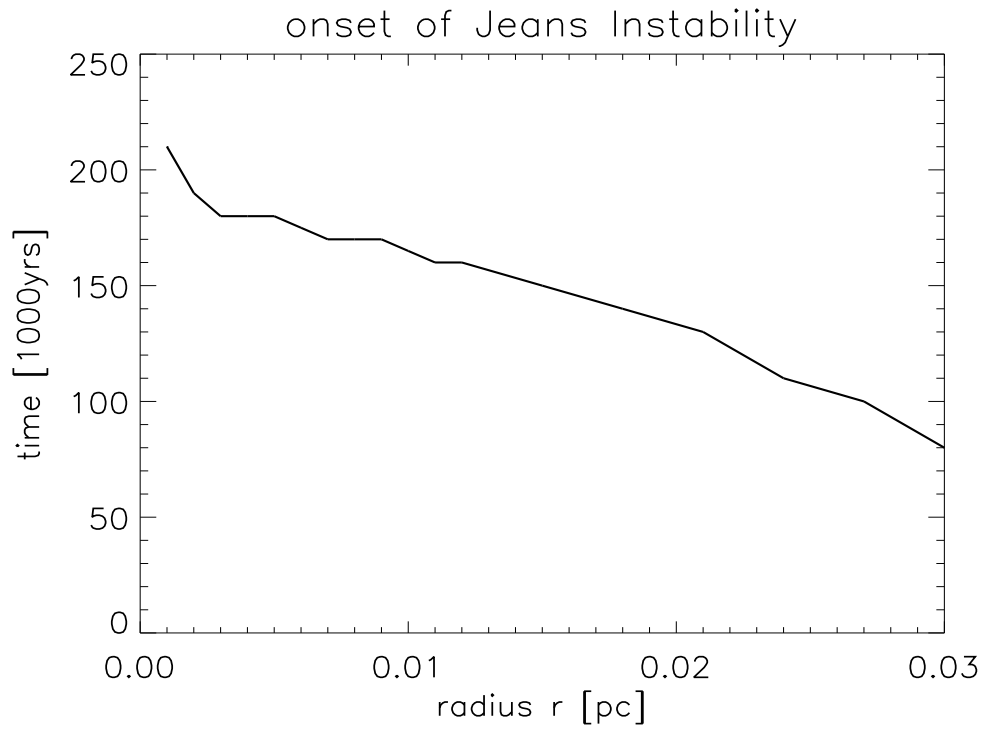
Figure 5.10: **For every sphere of radius r there is plotted the time at which the accumulated mass inside the sphere exceeds the local Jeans mass. The points are taken from the intersection points in the graphs of figure (5.7), (5.8) and (5.9). The Jeans instability evolves from outside in and is a result of the flat radial density distribution of the generated prestellar core.**
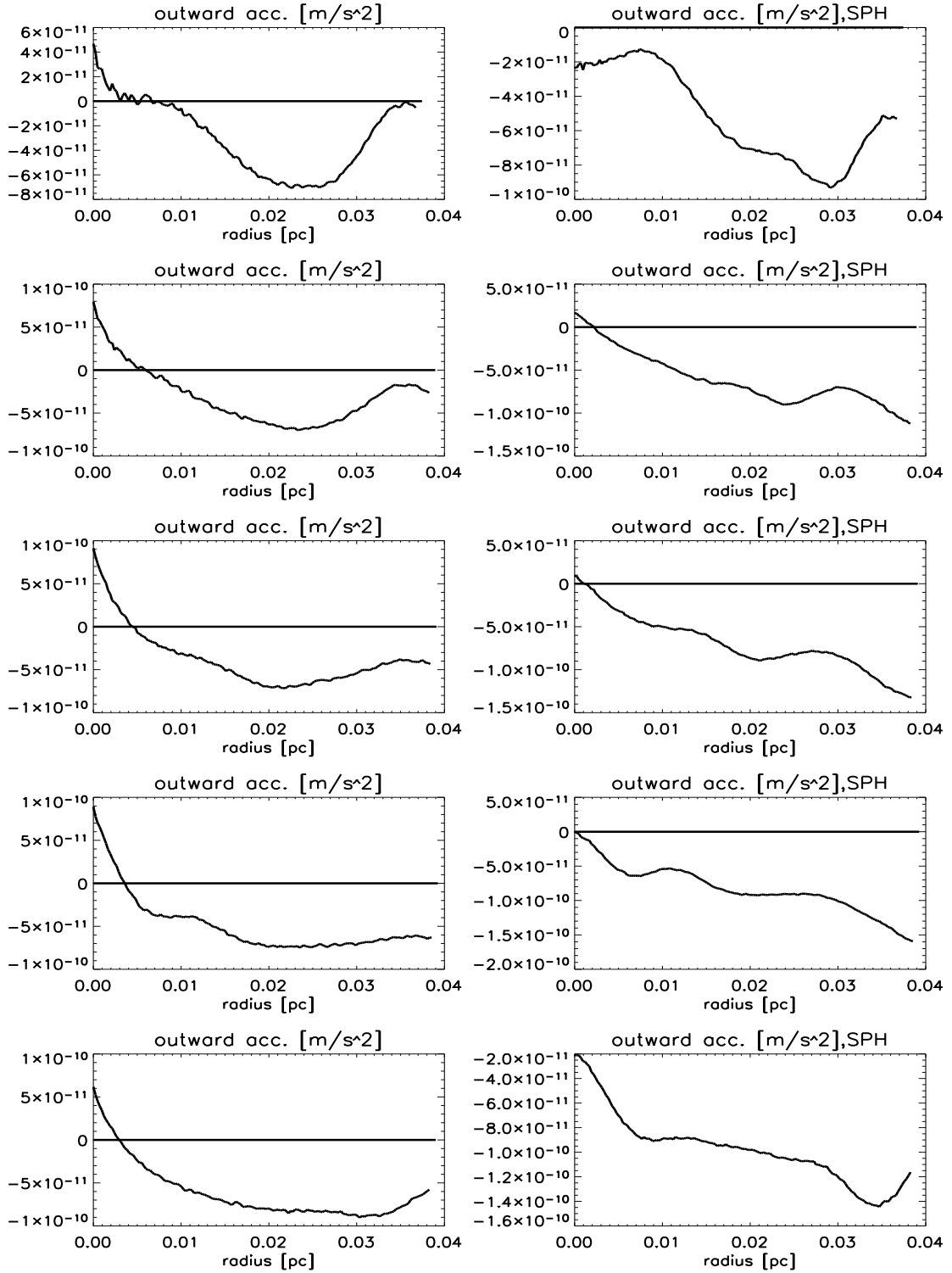
Figure 5.11: **Difference between the outward directed pressure gradient force and the inward directed gravitational force. Positive values correspond to an outward net acceleration. The horizontal line marks the zero point. 1st row: t=45000 yrs, 2nd row: t=60000 yrs, 3rd row: t=75000 yrs, 4th row: t=90000 yrs, 5th row: 105000 yrs after the initialization.**
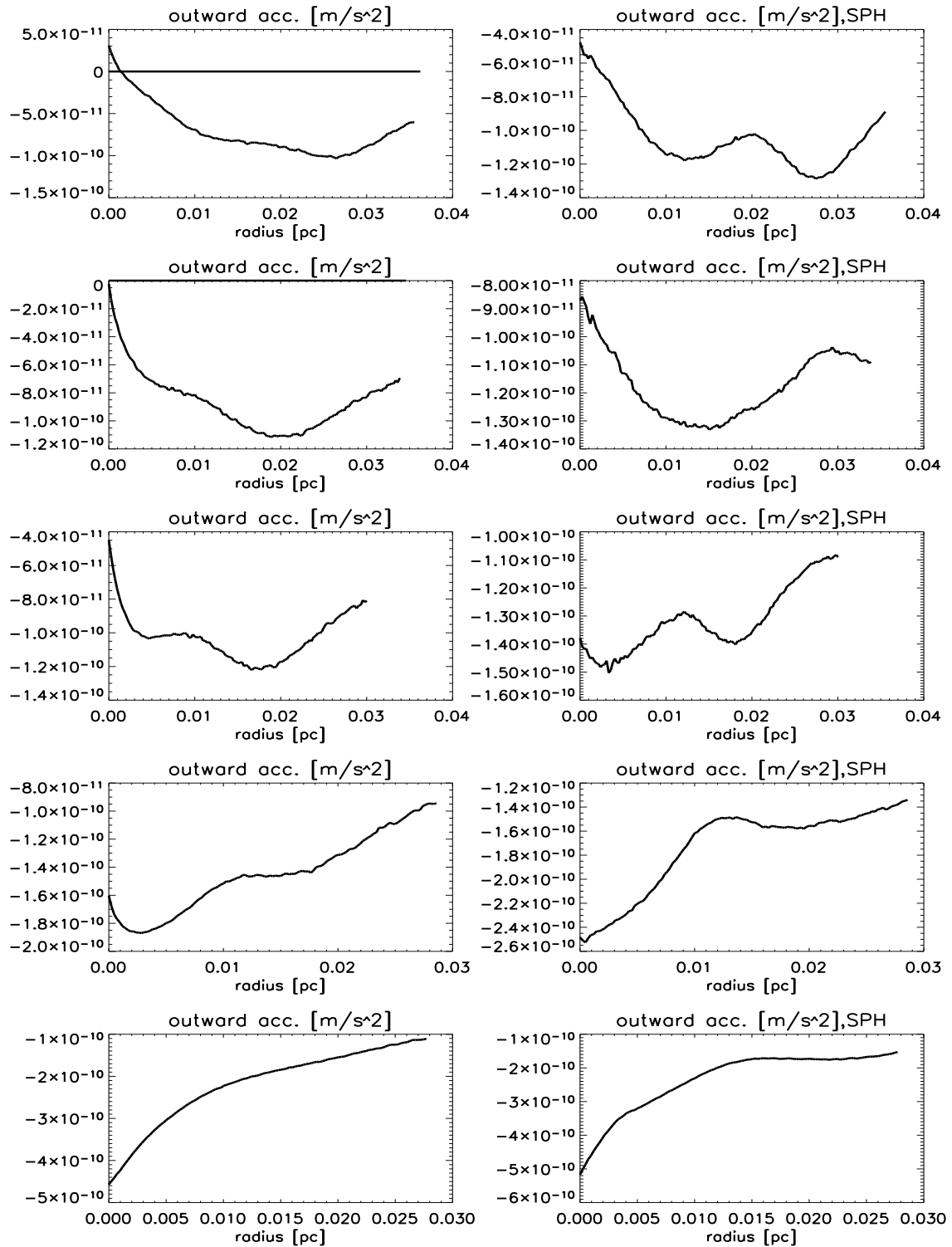
Figure 5.12: **Difference between the outward directed pressure gradient force and the inward directed gravitational force. Positive values correspond to an outward net acceleration. The horizontal line marks the zero point. 1st row: t=120000 yrs, 2nd row: t=135000 yrs, 3rd row: t=150000 yrs, 4th row: t=165000 yrs, 5th row: 180000 yrs after the initialization.**

5.2   Bonnor Ebert Spheres

In 1956 Bonnor analysed the stability of gaseous spheres against gravity. (Bonnor (1956)). In this section there is given a short introduction concerning the main idea standing behind the Bonnor-Ebert spheres and a summary of Bonnors results. In the second part we compare the density distributions of our prestellar core realizations to that of the Bonner-Ebert solutions. Think of a static isothermal spheric symmetric gas distribution compressed by its own gravity. At every distance r from the center the gas has to be in hydrostatic equilibrium. This means the pressure gradient force has to balance the force of gravity:

$$-\frac{dp}{dr} = \frac{4\pi G\rho}{r^2} \int_0^r \rho r'^2 dr' \tag{5.3}$$

or

$$\frac{1}{r^2}\frac{d}{dr} = \Big(\frac{r^2}{\rho}\frac{dp}{dr}\Big) = -4\pi G\rho \tag{5.4}$$

In addition at every point P the gas obeys the ideal equation of state

$$p = \frac{1}{m}k\rho T \tag{5.5}$$

where p, ρ and T are the pressure, density and temperature, and m is the molecular weight. Equation 5.4 and 5.5 can be combined to get an equation for the radial density distribution for an isothermal gas sphere:

$$\frac{1}{r^2}\frac{d}{dr} = \Big(\frac{r^2}{\rho}\frac{d\rho}{dr}\Big) = -\frac{4\pi G m\rho}{kT} \tag{5.6}$$

This is the well known Lane-Emden equation. It can be transformed into a dimensionless representation by using the following substitutions:

$$\rho = \lambda e^{-\Psi} \quad , \quad r = \beta^{1/2}\lambda^{-1/2}\xi \tag{5.7}$$

where λ is up to now an arbitrary constant and in β all the physical constants and variables independent of ρ and r are collected:

$$\beta = \frac{kT}{4\pi G m} \tag{5.8}$$

Equation 5.6 then becomes

$$\xi^{-2}\frac{d}{d\xi}\Big(\xi^2\frac{d\Psi}{d\xi}\Big) = e^{-\Psi} \tag{5.9}$$

We expect the density to reach a maximum at the center of the sphere which also implies a zero density gradient at this position. Therefore we can define the boundary conditions to be

$$\rho = \rho_c \quad , \quad \frac{d\rho}{dr} = 0 \tag{5.10}$$

where ρ_c is the central density of the sphere. In the following we the central density is assumed as a given parameter. If we choose now $\lambda = \rho_c$ then the boundary condition looks in the new variables:

$$\Psi = 0 \quad , \quad \frac{d\Psi}{d\xi} = 0 \quad \text{at} \quad \xi = 0 \tag{5.11}$$

This boundary condition completely fix the solution of the dimensionless Lane-Emden equation. All possible solutions given by the central density, temperature and molecular weight are called *Bonnor-Ebert spheres*. A stability analysis for Bonnor-Ebert spheres results in the fact that stability against gravitational collapse only depends on the density contrast between the center and the outer boundary respective the background density. If the density contrast exceeds a value of 13.5 the Bonnor-Ebert sphere solution becomes unstable and will collapse (figure 5.13). Transformed back to to the physical variables r and ρ_c this means that Bonnor-Ebert spheres with a critical density contrast are compact and light objects if the central density ρ_c is large and extended heavy objects if the central density is low. This is in direct analogy to the Jeans stability criterion, see section 3.2. This becomes clear if one compares the critical radius of a Bonnor-Ebert sphere with the Jeans length:

$$R_{BE,crit} = 0.49\sqrt{\frac{kT}{mG\rho_c}} = 0.76\sqrt{\frac{kT}{mG\rho_{mean}}} \quad ; \quad R_{Jeans} = 0.89\sqrt{\frac{kT}{mG\rho_0}} \qquad (5.12)$$

where ρ_{mean} is the mean density of the mass inside the critical radius and ρ_0 is the constant gas density used in Jeans's analysis. One sees there is besides the slightly different constants the same dependence on ρ and T. The same holds for the enclosed mass inside $r_{BE,crit}$ and the Jeans mass.

There are exist a lot of collapse calculations started with a Bonnor-Ebert sphere density distribution as initial condition. Because of that we looked, if our setups evolving through a Bonnor-Ebert sphere (BE sphere) like density distribution into the collapse. To do that we used 8 runs with setup Mach numbers 1.0, 1.5, 2.0, 2.5, 3.0, 4.0, 6.0, 10.0. For every run we tried to fit a BE sphere solution around the upcoming density maxima. This is done for the first 40 time steps of every run. One time step corresponds to $0.033t_{ff} = 5000$yrs. The algorithm works as follows. There is assumed a spherical symmetric density distribution around a density maximum. Then the gas density is estimated in n 'equal volume shells' around a density maximum. There is also one central sphere with the same volume as the shells. The estimated density of the central sphere is used as the central density for the BE solution. The free input parameter of the algorithm is the radius r of the BE sphere to be fitted. The appropriate number n of shells depends on the number of SPH-particles inside the radius r. The more SPH particles are found in one shell, the smaller is the scatter in the radial density curve. We use two criteria to decide if a SPH particle distribution is equivalent with a BE sphere. First we compare the density contrast between the outer shell and the central sphere with that of the BE solution. Second, we compare the accumulated mass inside the radius r with the mass of the BE sphere of same size. Altogether we looked up 2240 constellations in a 3 dimensional parameter cube:

- 8 runs with different initial Mach numbers

- the first 40 time steps of every run

- radii between 0.01 and 0.04 pc in steps of 0.005 pc.

First, there are no BE spheres with a critical density contrast of 13.5. We find BE like density distributions only with low density contrasts in the range of 1.5 ... 6. We don't find BE solutions before the dynamical equilibrium of density and velocity field is reached. After this point there is an epoch where we find stable subcritical BE solutions with density contrasts
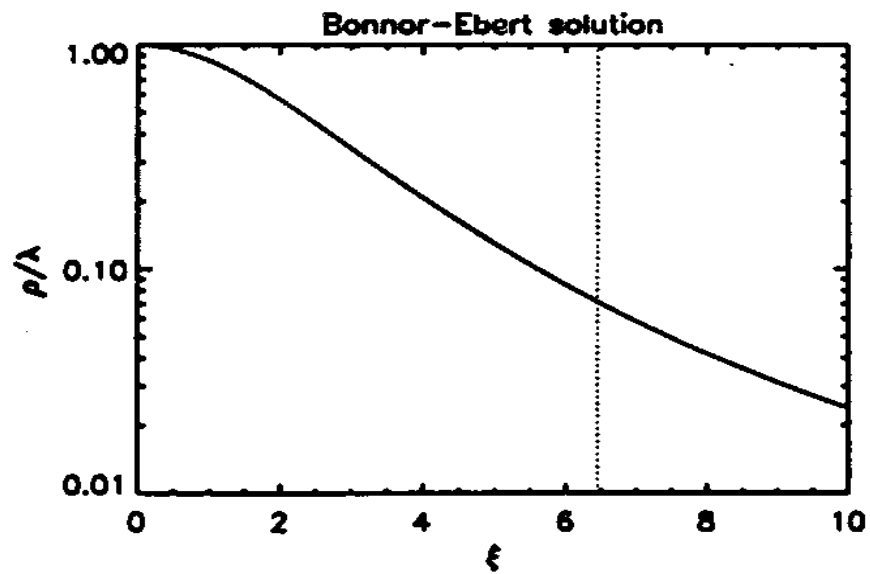
Figure 5.13: **Stability of the Bonnor-Ebert sphere solutions. All spheres extending beyond the dotted vertical line at $\xi = 6.5$ exceed the critical density contrast of 13.5 and are gravitational unstable. Plotted is the density in units of the central density against the dimensionless variable ξ which is proportional to r. In this dimensionless representation all Bonnor-Ebert sphere solutions look the same.**
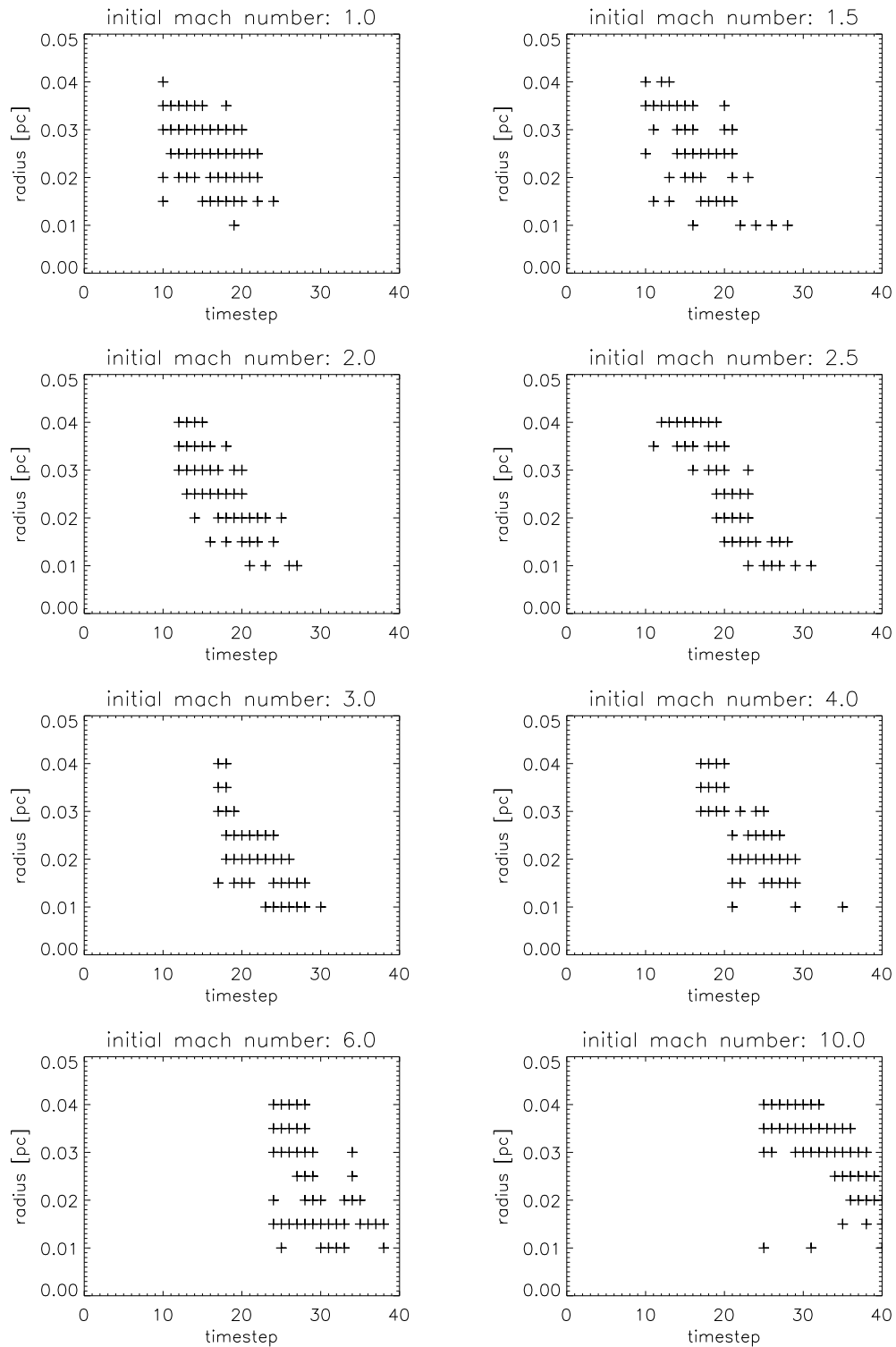
Figure 5.14: **Radius of the BE sphere like density distributions found in the collapse simulations.**
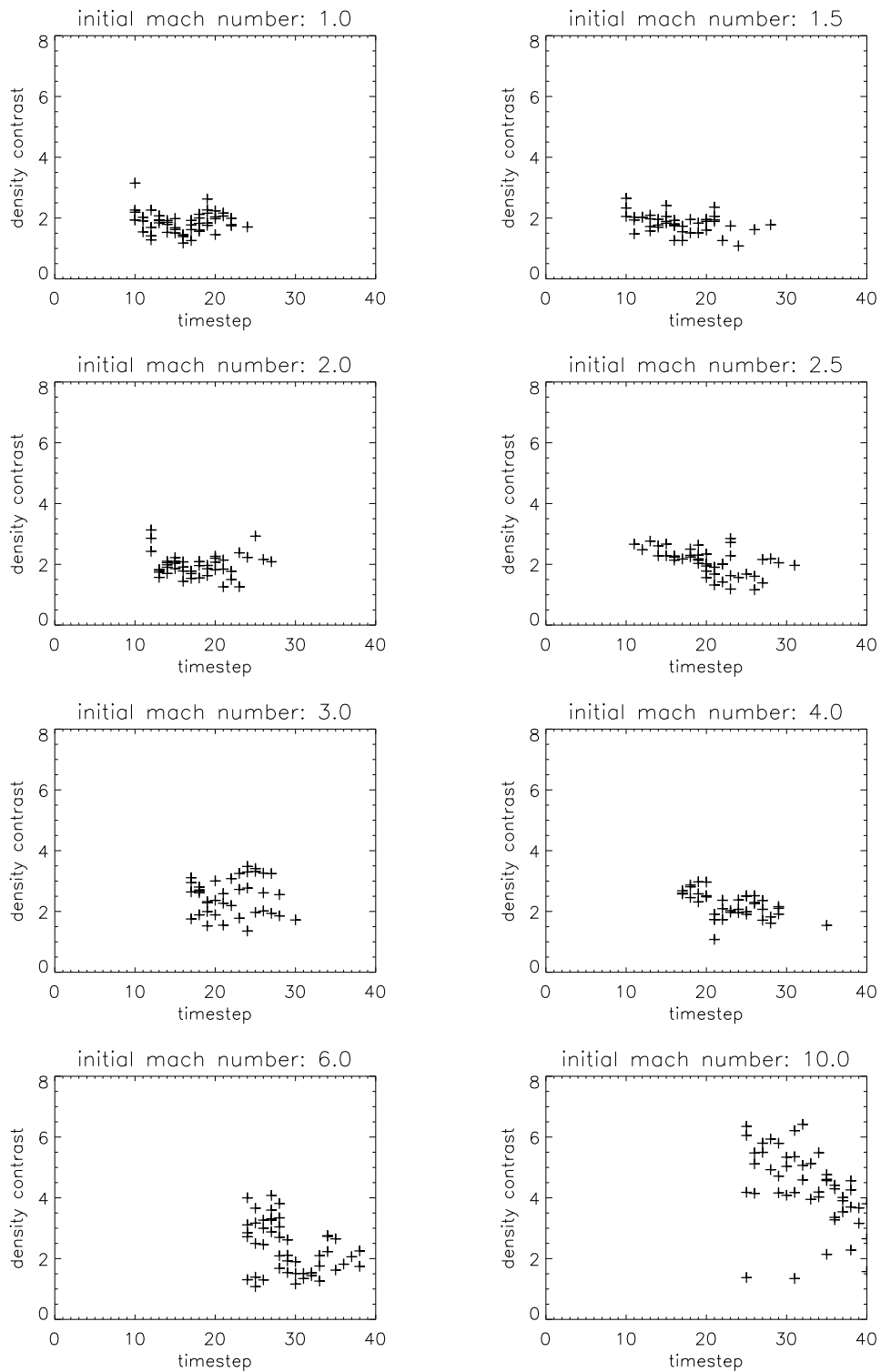
Figure 5.15: **Density contrasts of the BE sphere like density distributions found in the collapse simulations.**

less than 6 (figure 5.15). This epoch ends when the gas distribution starts to collapse. This is not surprising because the BE solution is based on a hydrostatic equilibrium. One sees, that in the case of a high Mach number this epoch is more extended because the system needs more time to dissipate enough kinetic energy to become unstable.

Altogether this means, that density structures built up primarily by turbulent velocities or primarily by gravity do not match the BE solution. It seems that it is a well balanced interplay of gravity and turbulence which yields the right conditions to evolve a BE sphere. There is a clear correlation between the initial Mach number and the density contrast of the BE solutions. The higher the initial Mach number the more pronounced is the density contrast of the BE like density distributions. Independent of the initial Mach number the BE solutions are wide and shallow at early times and become lighter and more compact at later times. Even though the prestellar core is still supported by the turbulence the central density is slowly growing. When the isothermal collapse phase starts dense regions will collapse faster than the others so that there evolves a density structure with a steep inner part which can't be matched by a BE sphere solution.

This analysis show, that marginal- or supercritical BE spheres as they are used as initial conditions do not evolve in a turbulent medium with Mach numbers not greater than 10. This result is supported by observations because the only critical BE sphere like density distributions found in nature are hosted in Bok globules. Bok globules are calm environments where the assumption of an equilibrium between thermal pressure and gravity approximately holds. Supercritical BE spheres may be created in extremely turbulent environments with Mach numbers far beyond 10. This is indicated by the increasing density contrast for large initial Mach numbers. We can't prove this yet, because in the case of extremely supersonic turbulence (Mach numbers greater than 10) our SPH algorithm start to smear out the shocks. A nice example is Barnard-68, where Alves et al. (2001) showed that it nicely fits to a Bonnor-Ebert sphere. After all one should keep in mind that prestellar cores and even Barnard-68 are not spheric symmetric. So the results presented here are not in contradiction to the previous sections.

5.3   Detailed velocity Structure

This section gives a detailed analysis on how density and velocity field interact with each other and how the first condensations are created by turbulence. Therefore we avoid any spherical symmetry in our analysis to take into account the spatial complexity of the evolving structures. Exemplary we present the whole analysis for run425, one of our 22 collapse simulations (section 6.5).

As an overview figure 5.16 shows the evolution of the density structure as seen from the z-axis. Plotted are the logarithmic density distributions at t=50000 yrs, t=75000 yrs, t=100000 yrs, 125000 yrs, t=150000 yrs and t=175000 yrs after the initialization. Densities range from 0.3 resp. 2×10^{-20} g/cm³ (black) to 600 4×10^{-17} g/cm³ (white).

In the figures 5.17, 5.18, 5.19, 5.20 and 5.21 we present a comprehensive visualisation for the spatial configuration of the mass flows. Therefore the velocity and density structure in 0.005 pc (1000 AU) thick slices through the density maximum is plotted. The direction of the flow is given by the arrows, their size indicates the absolute value of the velocities. The velocities are rest frame velocities in respect to the density maximum. The density distribution is indicated by small dots showing the distribution of the SPH particles inside a slice. Circles enclose a 1000 AU region around the density maximum. To get an optimum insight in the three dimensional flow pattern cuts along the y-z plane (upper row), along the x-z plane (middle row), and along the x-y plane (lower row) are shown.

At the first time shock fronts and strong subsonic velocity gradients create a network of differently extended filaments and sheets. The gas density is highest along this filaments and in particular at the intersection points of this filaments. These are the locations where prestellar cores predominantly form. In addition these intersection points are the preferential regions of converging flows (figure 5.17).

The visualization of the spatial velocity structure clearly shows that the creation of a star is far from being a spherical symmetric event. Even in the late stages ($t > 150000$ yrs) the action of the residual turbulence is visible. Nevertheless gravity starts to dominate the scene. To get more information about the action of the velocity field we calculated the local three dimensional velocity dispersion σ_{tot}, the velocity dispersion tangential to the gravitational force vector σ_{tan} and the ram pressure, see figures 5.22, 5.23, 5.24 and 5.25. The values are local mean values and where calculated as follows. A probe cylinder was separated in a stack of disks. Every disk has a thickness of 0.006 pc   (1200 AU) and a diameter of 0.012 pc. Inside the volume of these disks there was calculated a mean value of the physical variable of interest based on all SPH particles found inside the disks volume. This results in a spatial resolution of the plots of 600 AU.

Figure 5.22 (left column) shows that there is at all times a large negative velocity gradient around the position of the density maximum. A negative velocity gradient corresponds to a compression of the gas along the z-axis while positive slopes indicate a dilution of the gas. The maximum velocity gradient of -40 km/s $\cdot$ pc^{-1} is seen about 75000 yrs after initialization and extends over 0.02 pc. The density maximum emerges at the edge of a more extended over-dense region to the left (right column). Even though the region of negative velocity gradient is cited symmetric around the peak, the condensation gains mass predominantly from the left due to the larger densities there.

The inward moving gas streams are decelerated near the center and so the conveyed (advected) momentum is a source of ram pressure acting as an additional force compressing the

region around the density peak:

$$P_{ram} = (\rho v) \cdot v = \rho v^2 \tag{5.13}$$

The term (ρv) is the amount of gas streaming through a unit area per unit time. If this is multiplied by the velocity of the gas one gets the momentum flow per unit time which can be interpreted as a force acting per unit area if the flow is decelerated down to zero velocity. In the figures 5.23, 5.23 and 5.23 the ram pressure is shown along the x, y and z axis. The unsymmetric density distribution in z direction around the density peak induces a strong unsymmetric rampressure profile. There is a strong $12 - 14\,\text{nPa}$ rampressure peak left to the density peak for $t < 130000\,\text{yrs}$ while right to the peak there is only negligible rampressure due to the very low gas densities in this region.

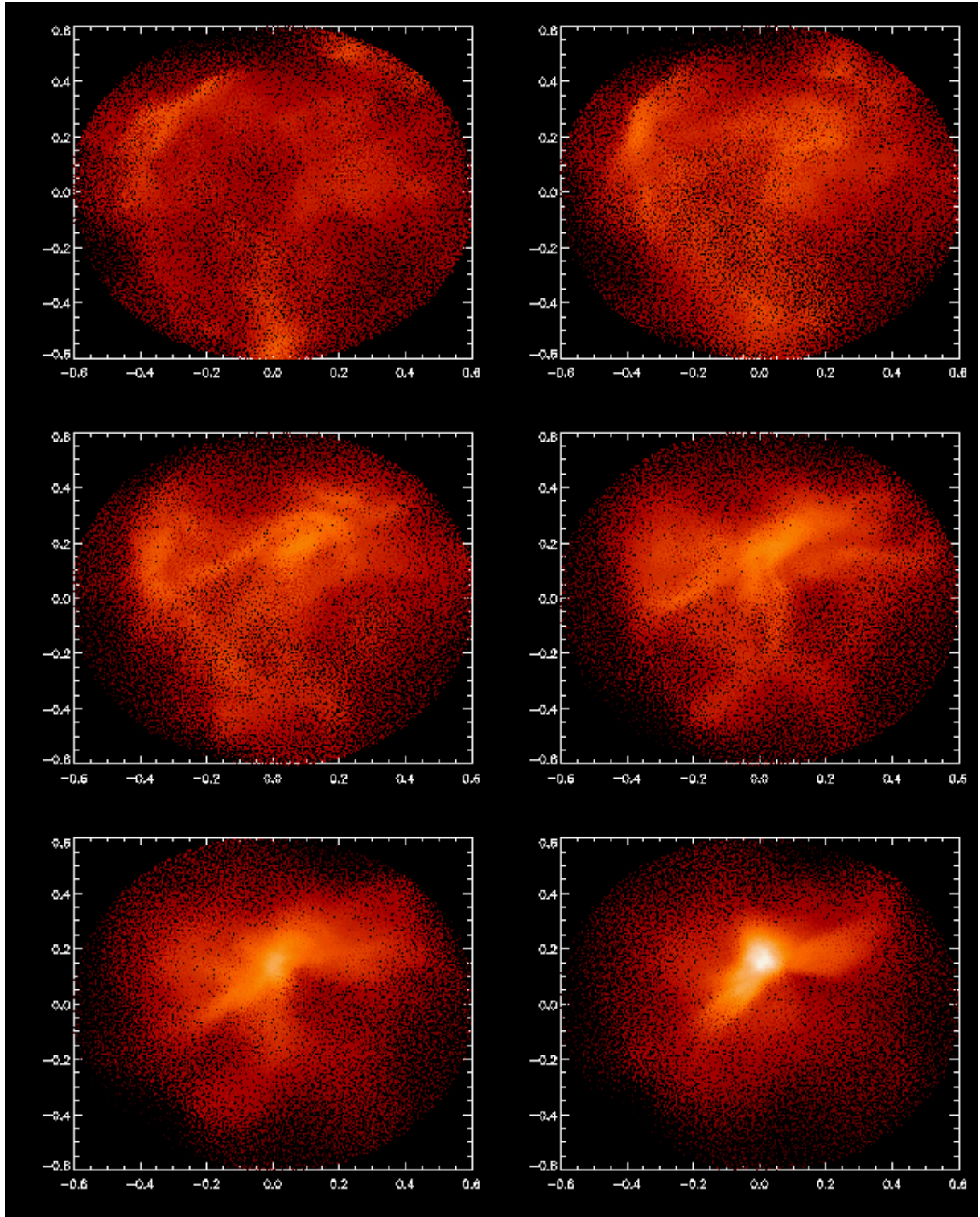Figure 5.16: **Logarithmic density distribution (color coded) for run425 at t=50000 yrs, t=75000 yrs, t=100000 yrs, 125000 yrs, t=150000 yrs and t=175000 yrs after the initialization. Densities range from 0.3 resp. $2 \cdot 10^{-20}$ g/cm^3 (black) to 600 $4 \cdot 10^{-17}$ g/cm^3 (white). Size scales are given in units of** 0.1 pc.

Figure 5.17: **Detailed velocity structure 70000 yrs (timestep 14, left column) and 75000 yrs (timestep 15, right column) after the initialization. The plots show the velocity and density structure in** $0.005\,\mathrm{pc}$ **(1000 AU) thick slices through the density maximum. The direction of the flow is given by the arrows, their size indicates the absolute value of the velocities. Small dots showing the distribution of the SPH particles. Upper row: cut along the y-z plane. Middle row: cut along the x-z plane. Lower row: cut along the x-y plane.**
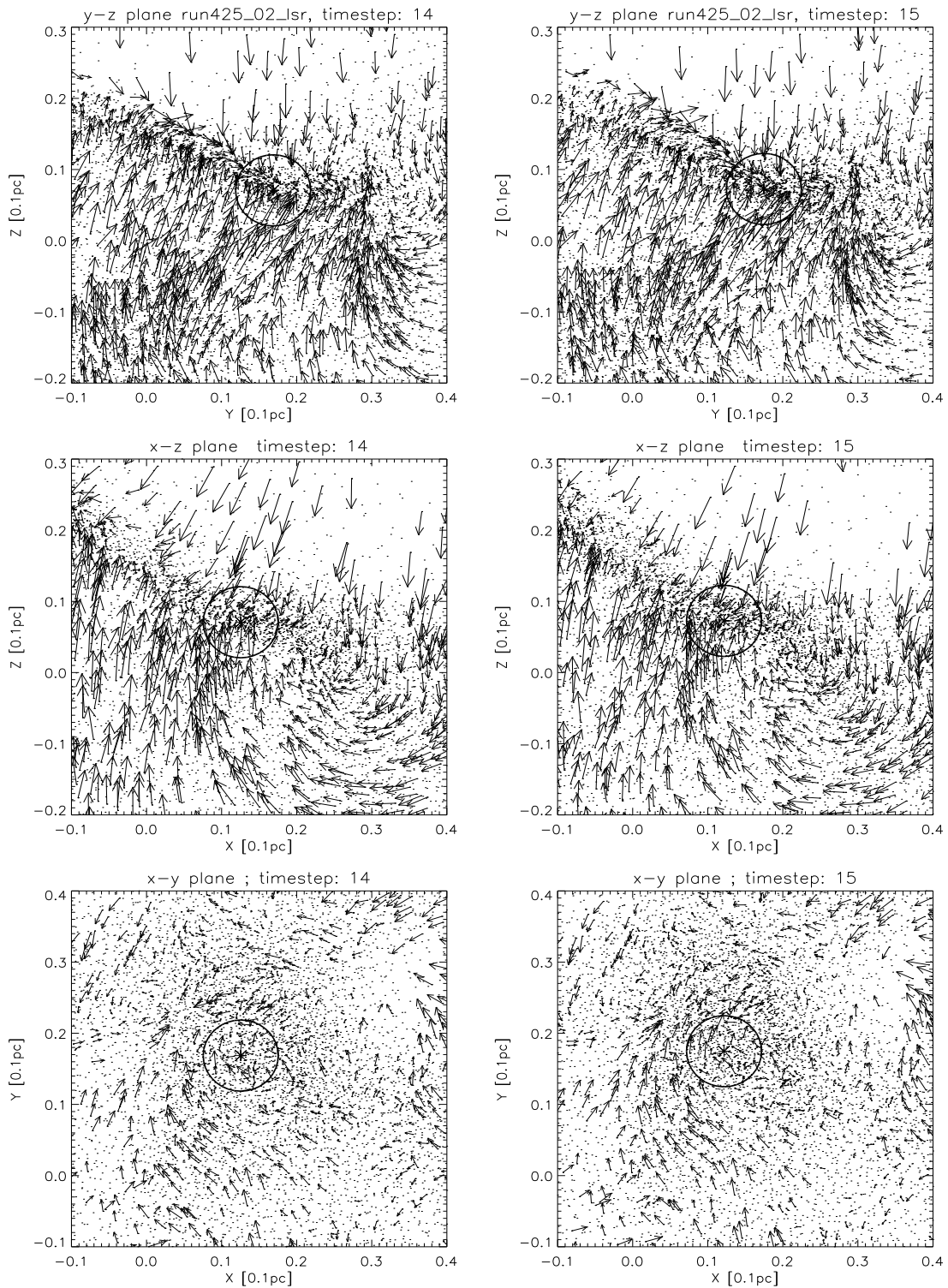
Figure 5.18: **Detailed velocity structure 100000 yrs (timestep 20, left column) and 105000 yrs (timestep 21, right column) after the initialization. The plots show the velocity and density structure in** $0.005\,\mathrm{pc}$ **(1000 AU) thick slices through the density maximum. The direction of the flow is given by the arrows, their size indicates the absolute value of the velocities. Small dots showing the distribution of the SPH particles. Upper row: cut along the y-z plane. Middle row: cut along the x-z plane. Lower row: cut along the x-y plane.**

Figure 5.19: **Detailed velocity structure 120000 yrs (timestep 24, left column) and 125000 yrs (timestep 25, right column) after the initialization. The plots show the velocity and density structure in** $0.005\,\mathrm{pc}$ **(1000 AU) thick slices through the density maximum. The direction of the flow is given by the arrows, their size indicates the absolute value of the velocities. Small dots showing the distribution of the SPH particles. Upper row: cut along the y-z plane. Middle row: cut along the x-z plane. Lower row: cut along the x-y plane.**
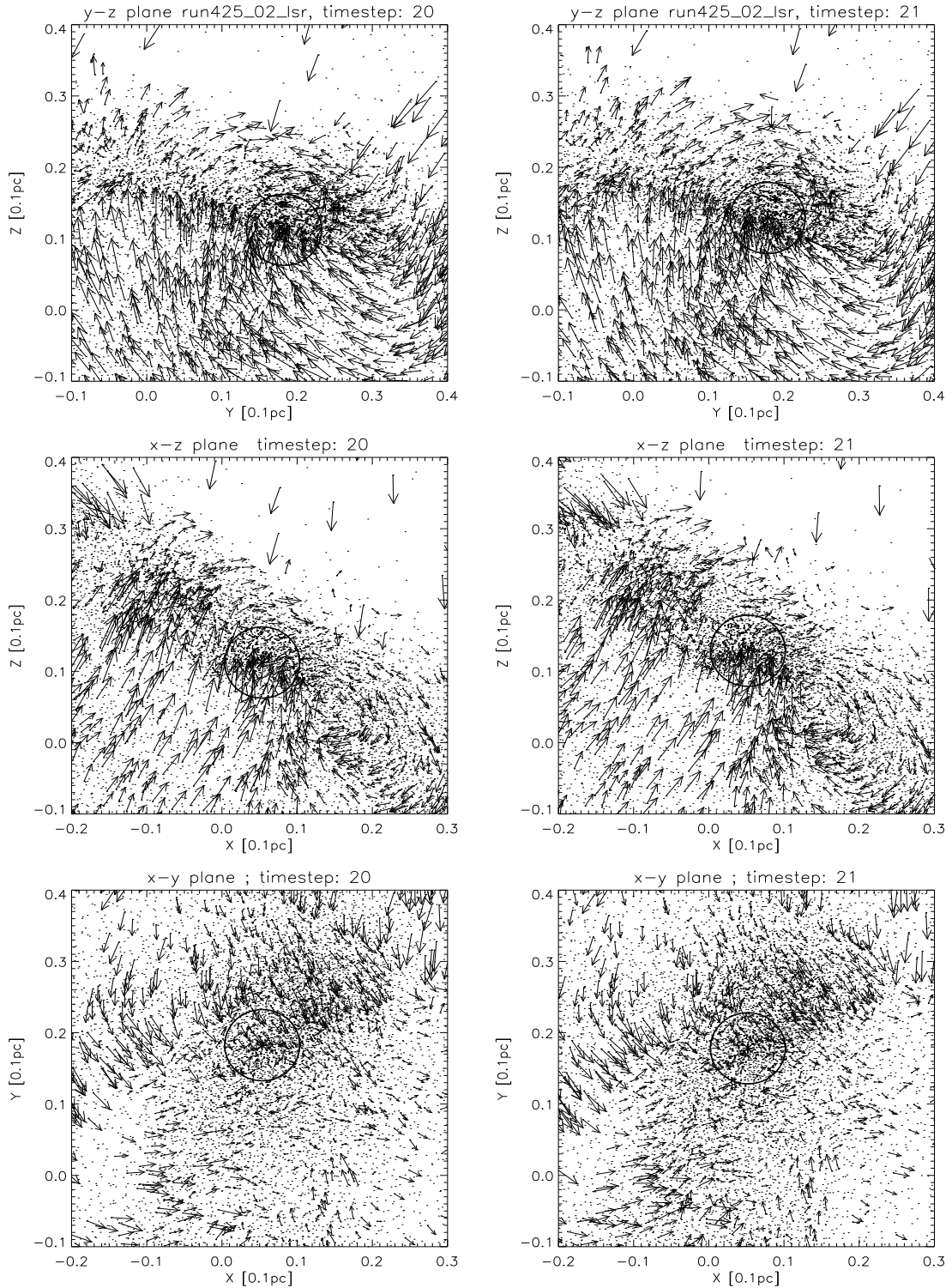
Figure 5.20: **Detailed velocity structure 150000 yrs (timestep 30, left column) and 155000 yrs (timestep 31, right column) after the initialization. The plots show the velocity and density structure in** $0.005\,\mathrm{pc}$ **** $(1000\,\mathrm{AU})$ **thick slices through the density maximum. The direction of the flow is given by the arrows, their size indicates the absolute value of the velocities. Small dots showing the distribution of the SPH particles. Upper row: cut along the y-z plane. Middle row: cut along the x-z plane. Lower row: cut along the x-y plane.**
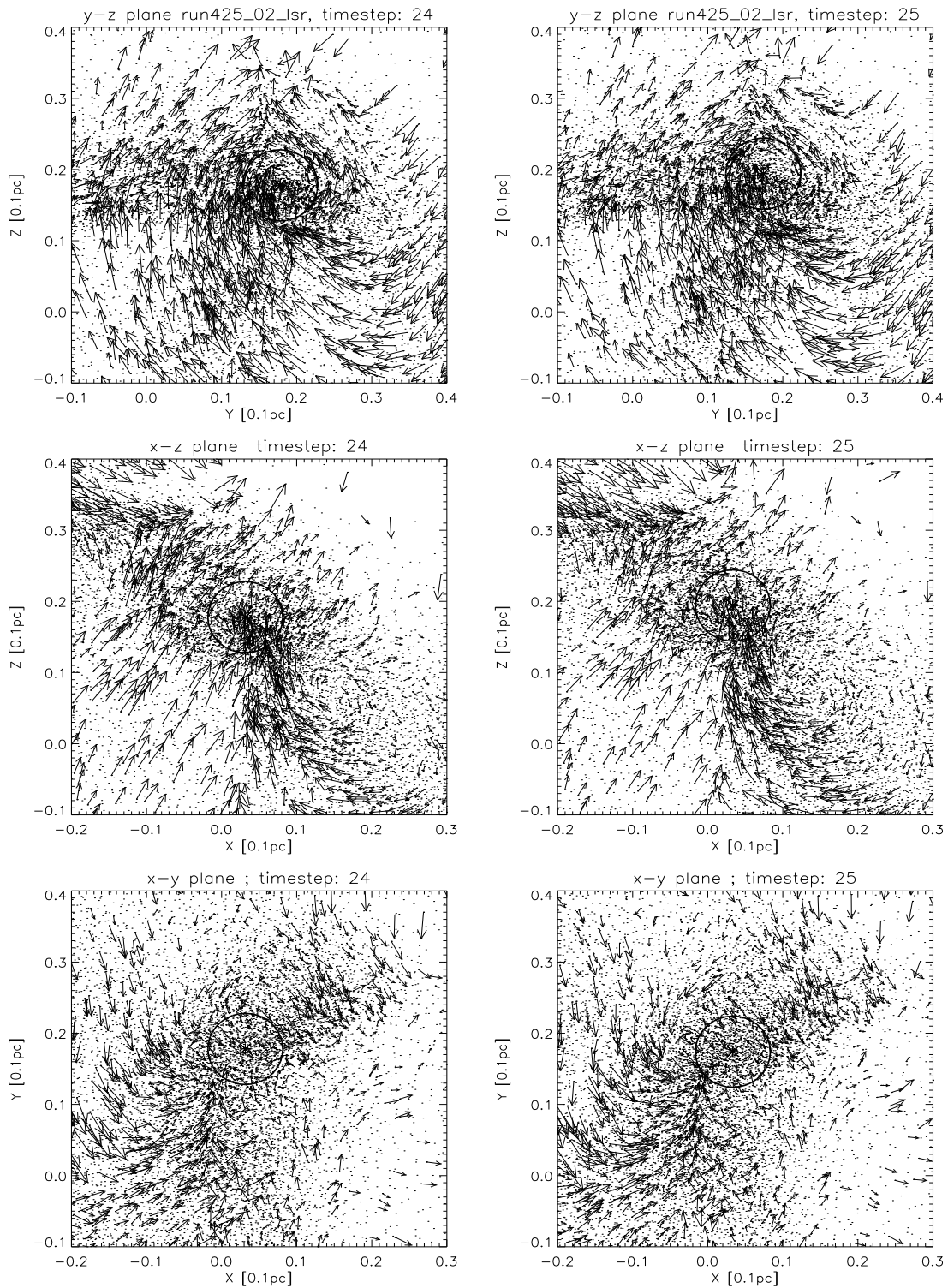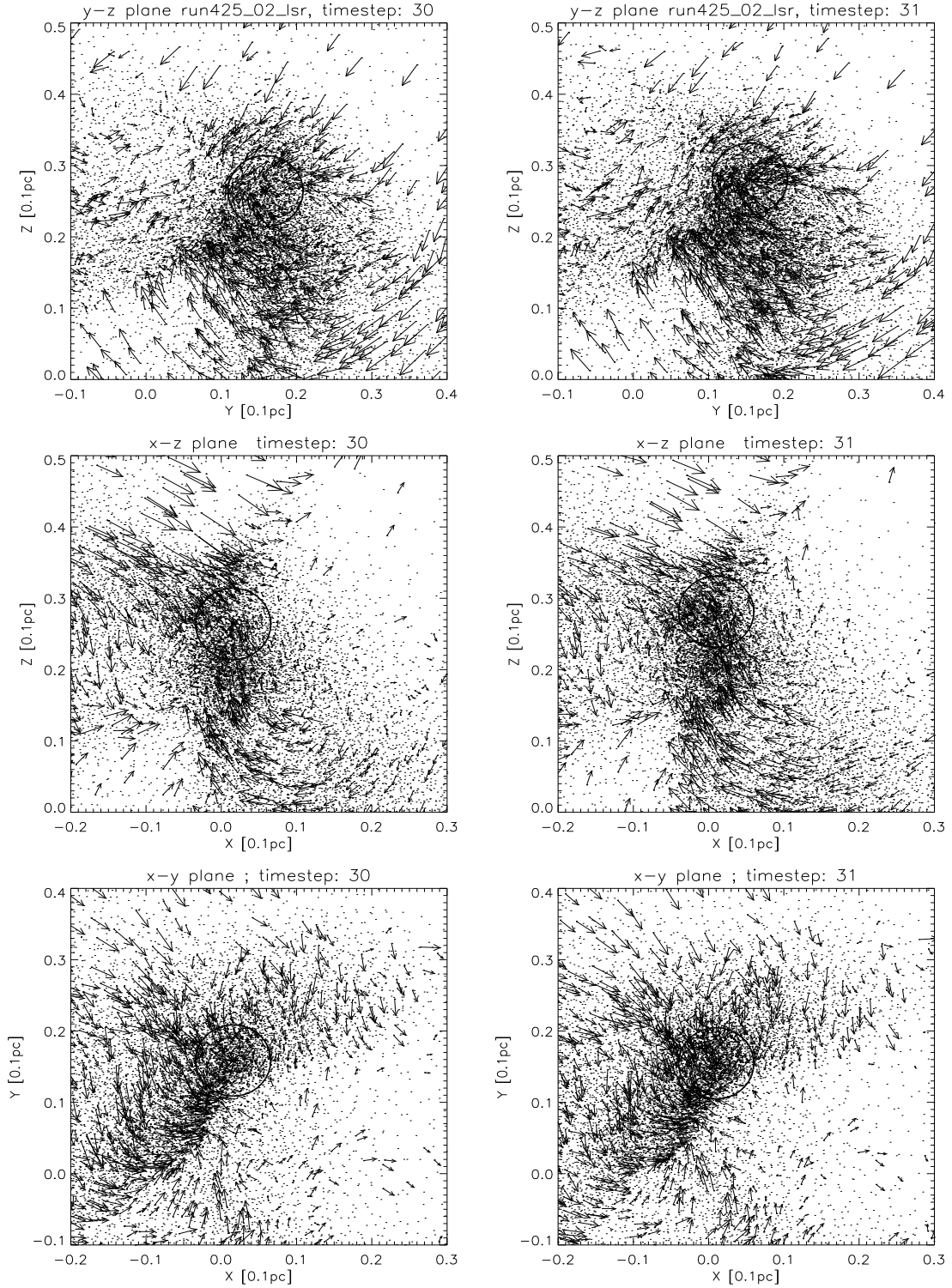
Figure 5.21: **Detailed velocity structure 170000 yrs (timestep 34, left column) and 175000 yrs (timestep 35, right column) after the initialization. The plots show the velocity and density structure in** $0.005\,\mathrm{pc}$ **(**$1000\,\mathrm{AU}$**) thick slices through the density maximum. The direction of the flow is given by the arrows, their size indicates the absolute value of the velocities. Small dots showing the distribution of the SPH particles. Circles enclose the** $1000\,\mathrm{AU}$ **region around the density maximum. Upper row: cut along the y-z plane. Middle row: cut along the x-z plane. Lower row: cut along the x-y plane.**

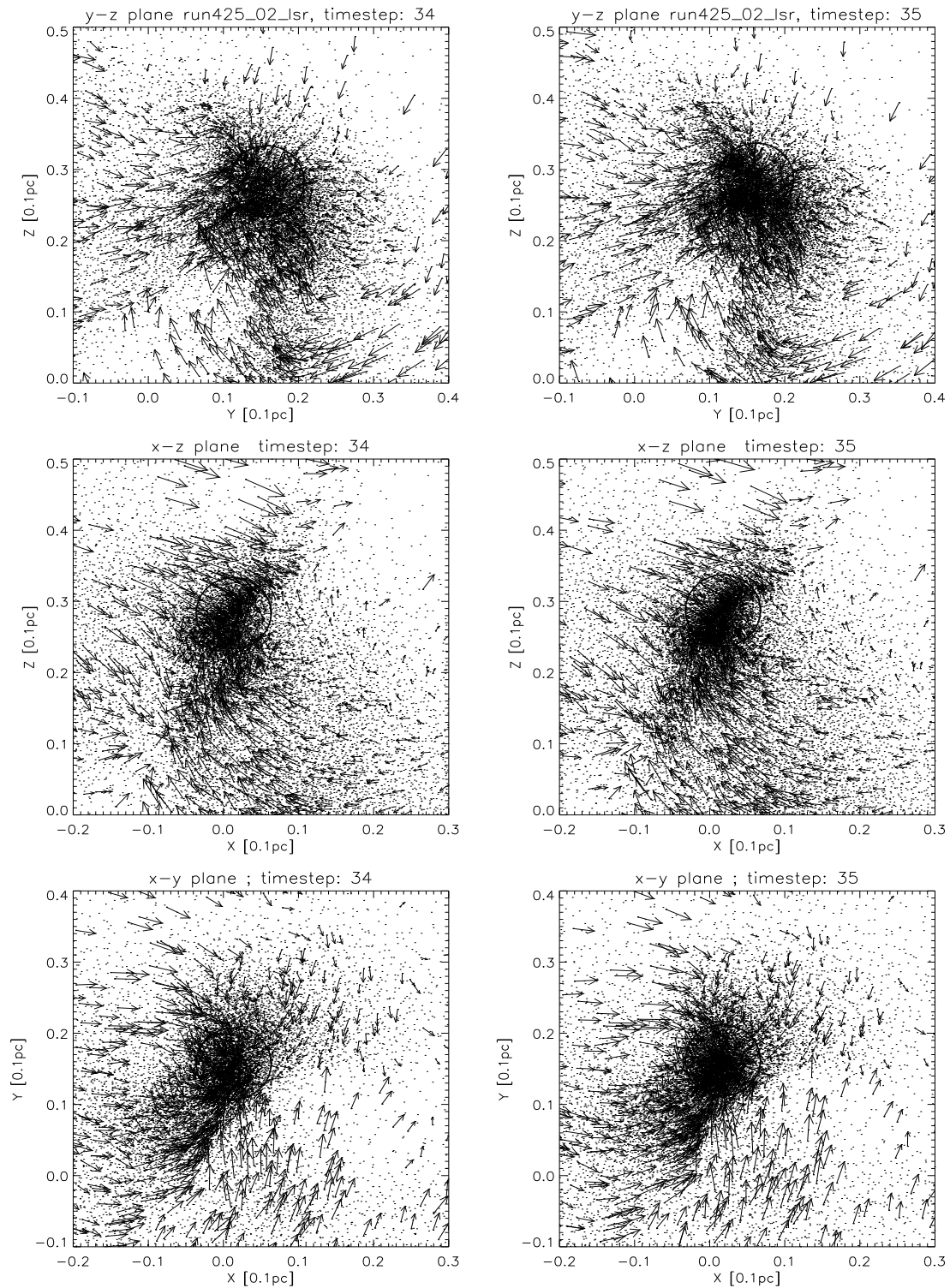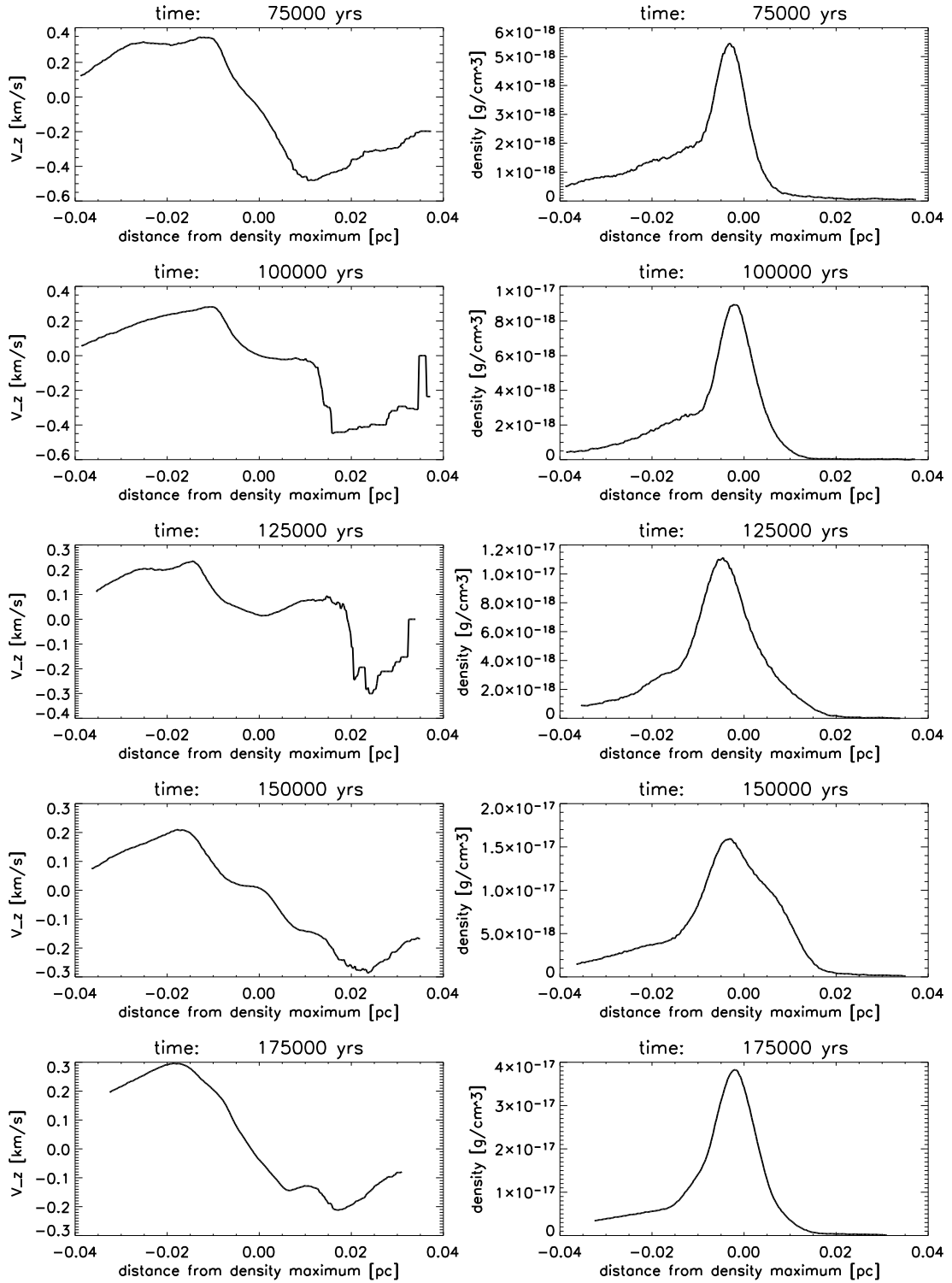Figure 5.22: **z component of the velocity (left column) and density (right column) along a 2400 AU diameter probe cylinder through the density maximum. The cylinder axis is aligned parallel to the z-axis. The initial mean density is 2×10^{-19} g/cm^3.**
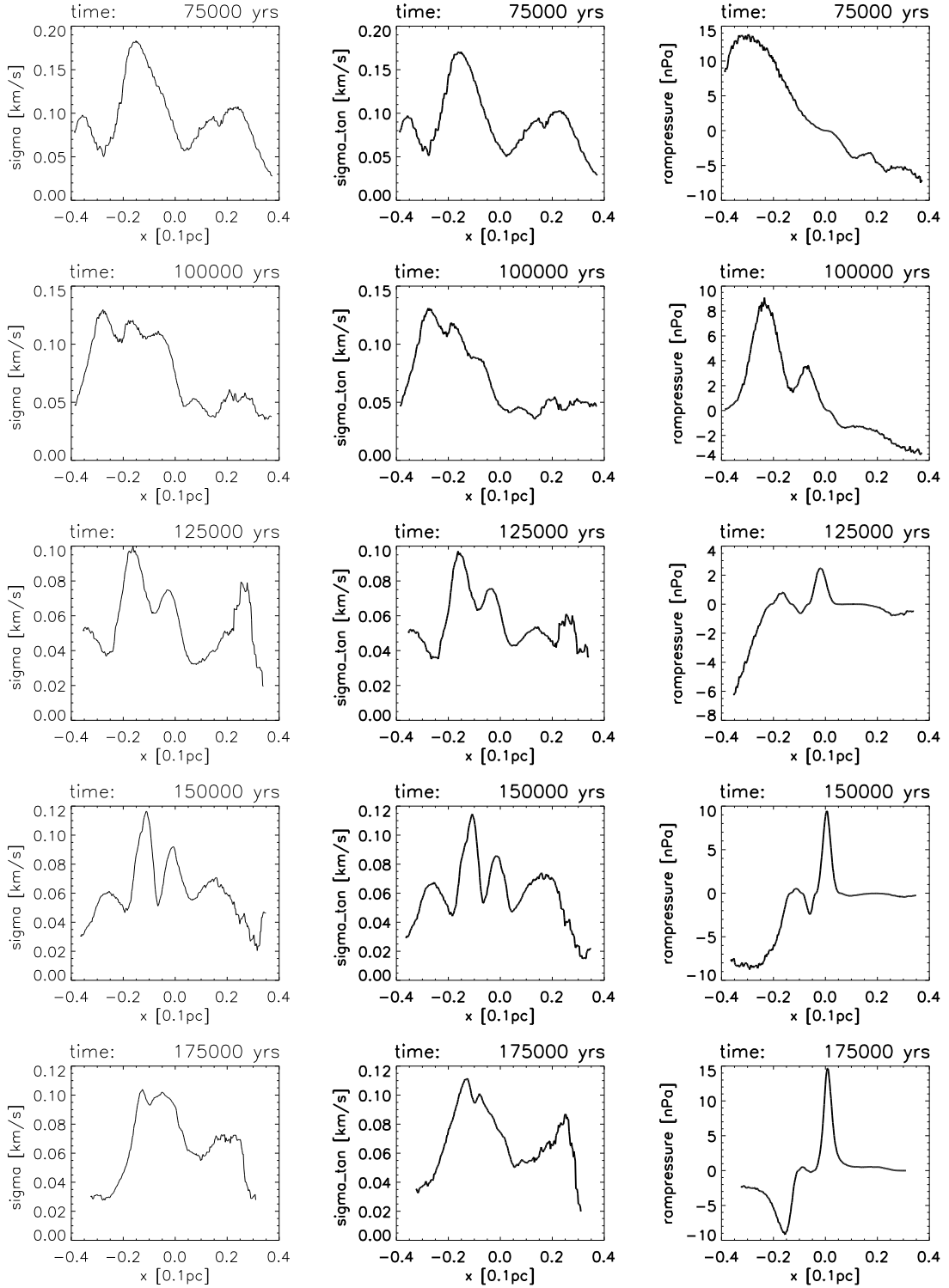
Figure 5.23: **Total velocity dispersion σ_{tot} (left column), velocity dispersion of the tangential velocity components σ_{tan} (middle column) and the resulting ram pressure p_{ram} along a $2000\,\mathrm{AU}$ diameter probe cylinder through the density maximum (right column). The cylinder axis is aligned parallel to the x-axis. The ram pressure is based on the relative velocities in respect to the density maximum.**

Figure 5.24: **Total velocity dispersion** σ_{tot} **(left column), velocity dispersion of the tangential velocity components** σ_{tan} **(middle column) and the resulting ram pressure** p_{ram} **along a 2000 AU diameter probe cylinder through the density maximum (right column). The cylinder axis is aligned parallel to the y-axis. The ram pressure is based on the relative velocities in respect to the density maximum.**

Figure 5.25: **Total velocity dispersion** σ_{tot} **(left column), velocity dispersion of the tangential velocity components** σ_{tan} **(middle column) and the resulting ram pressure** p_{ram} **along a 2000 AU diameter probe cylinder through the density maximum (right column). The cylinder axis is aligned parallel to the z-axis. The ram pressure is based on the the relative velocities in respect to the density maximum.**
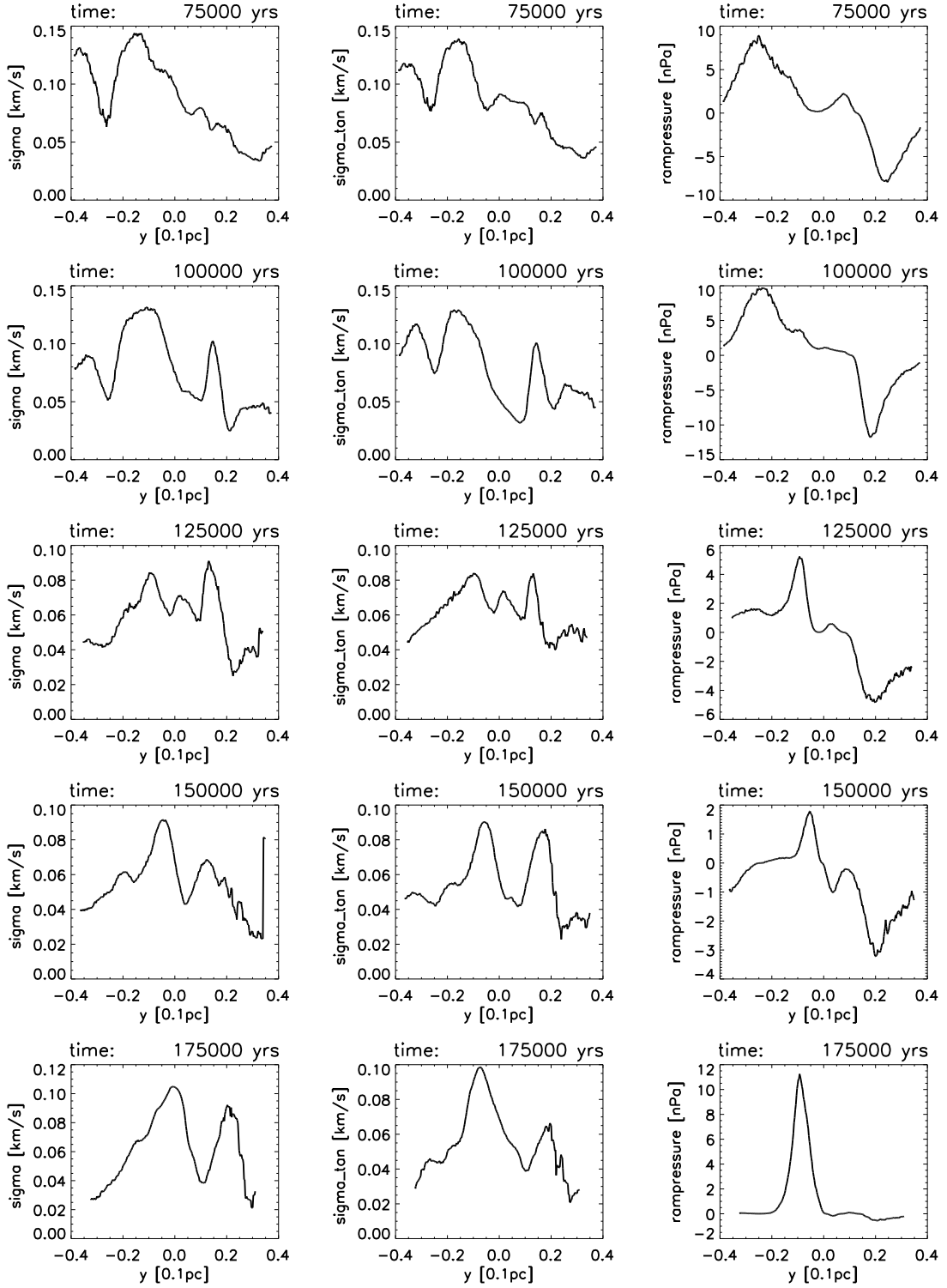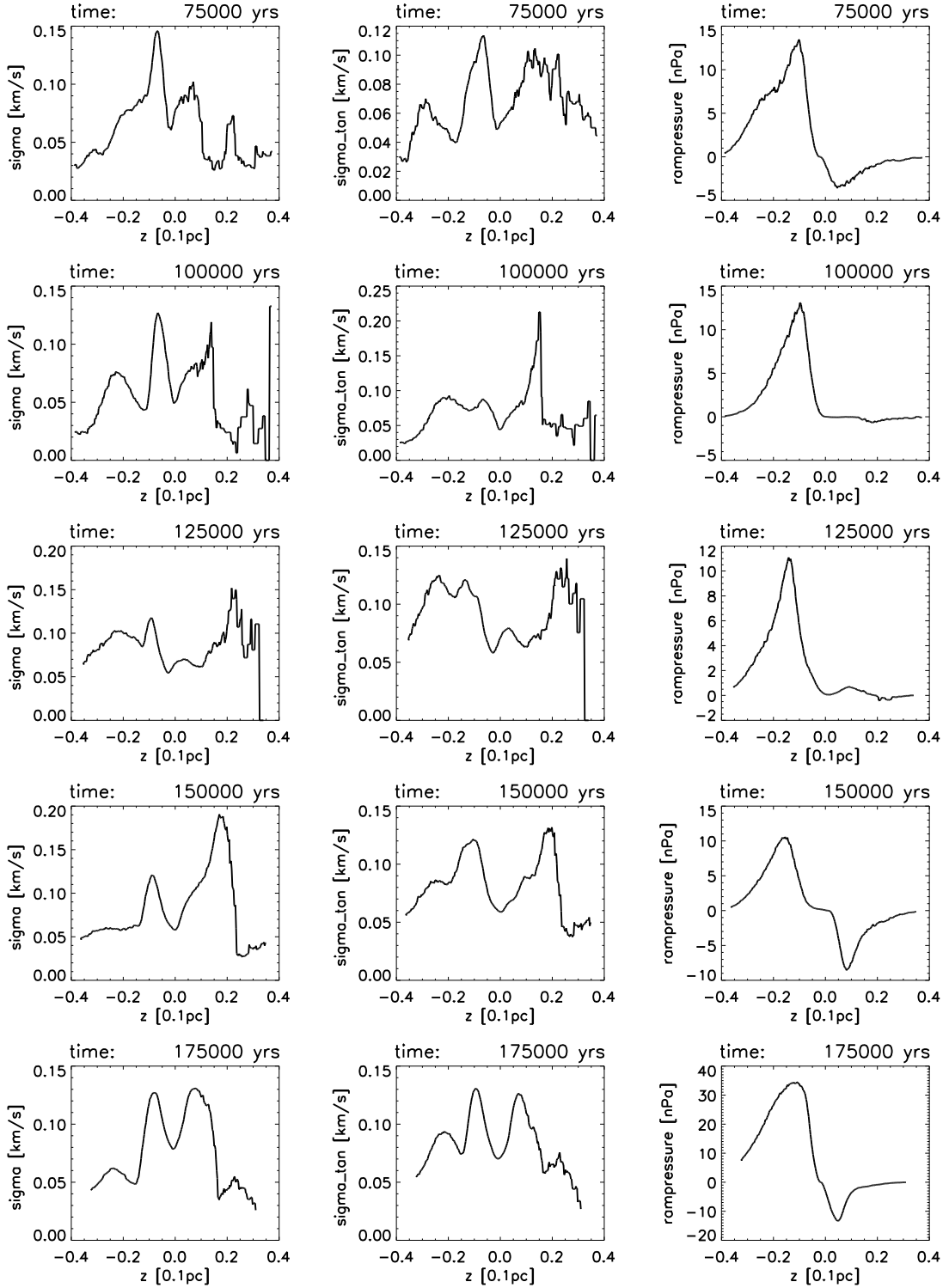
5.4 Velocity dispersion

The velocity dispersion is defined as the standard deviation around the mean velocity $\langle v \rangle$:

$$\sigma = \sqrt{\langle v^2 \rangle - \langle v \rangle^2} \tag{5.14}$$

In nature it is the the velocity dispersion of the individual gas molecules which causes the observed line broadening. As a result an observer always get an superposition of thermal line width and turbulent line width.

The kinetic energy stored in turbulent motions decays as a power law of the form

$$E_{kin} = E_0 \cdot t^\eta \tag{5.15}$$

where η is shown to be in the range of $\eta = -1.3 \quad \ldots - 1.6$ (Mac Low et al. (1998b), Stone et al. (1998), Smith et al. (2000), Pavlovski et al. (2002)) and E_0 is the amount of kinetic energy at the initialization of the run. The dissipation timescale for turbulence is of the order of a wave crossing time. In the case of non supersonic motions it is in the same order as the free fall time and scales as $\rho^{-1/2}$.

The onset of the isothermal collapse phase depends on the temperature, the density distribution and the amount of turbulent energy. The core need not to collapse exactly at M=0.7 as predicted by the extended Jeans criteria (section 4.3) because there we have implicitly assumed that matter is equally distributed. This is indeed not the case at the onset of the isothermal collapse phase. If there is by chance a single strong condensation, then it will collapse, even though the Mach number $M(t)$ still exceeds our critical value of $M_{crit} = 0.7$. If there are lots of small scale condensations, then the collapse is delayed longer. In the central regions of prestellar cores (as far as they can be resolved) the turbulent line widths seem to be constant and in the order of $\sigma = 0.7c_s$ (Goodman et al. (1998)). To compare this observational result with our simulations we calculated the velocity dispersion in shells of radius r around the density maximum. The exemplary result for run425 is given in figure 5.26. Shown is the velocity dispersion as a function of the distance r from the density maximum at t=100000 yrs (upper panel), t=150000 yrs (middle panel) and t=175000 yrs (lower panel) after the initialization. For $r > 0.01 \, \text{pc} \quad \sigma$ stays roughly constant around a value of $0.6 \ldots 0.7 c_s = 0.1 \ldots 0.13 \, \text{km/s}$ which is in good agreement with observations (Goodman et al. (1998)). At the center σ drops down. At this point it is not clear if its a real or an artificial effect because one expects σ to drop down significantly when the size of the shells reach the size scale of the SPH particles' smoothing length. The mean smoothing length at the initialization of our runs is $h_0 \simeq 0.003 \, \text{pc}$. The smoothing length scales as $h \sim \rho^{-1/3}$. Before the isothermal collapse phase sets in density contrasts range from 10:1 ... 50:1 resulting in a smoothing length of the order of 0.001 pc. A blind test has shown that for $\rho = \rho_0$ results for $r \leq 0.003 \, \text{pc}$ are significantly affected by the smoothing. We can conclude that the drop in σ in the range $0.003 < r < 0.01 \, \text{km/s}$ (middle and lower panel of figure 5.26) is real. This is consistent with the fact that turbulent motions are dissipated first in the densest regions. On the other hand the overall contraction increase the velocity dispersion. This effect becomes important especially during the rapid collapse phase and is most prominent in the innermost parts of the core.
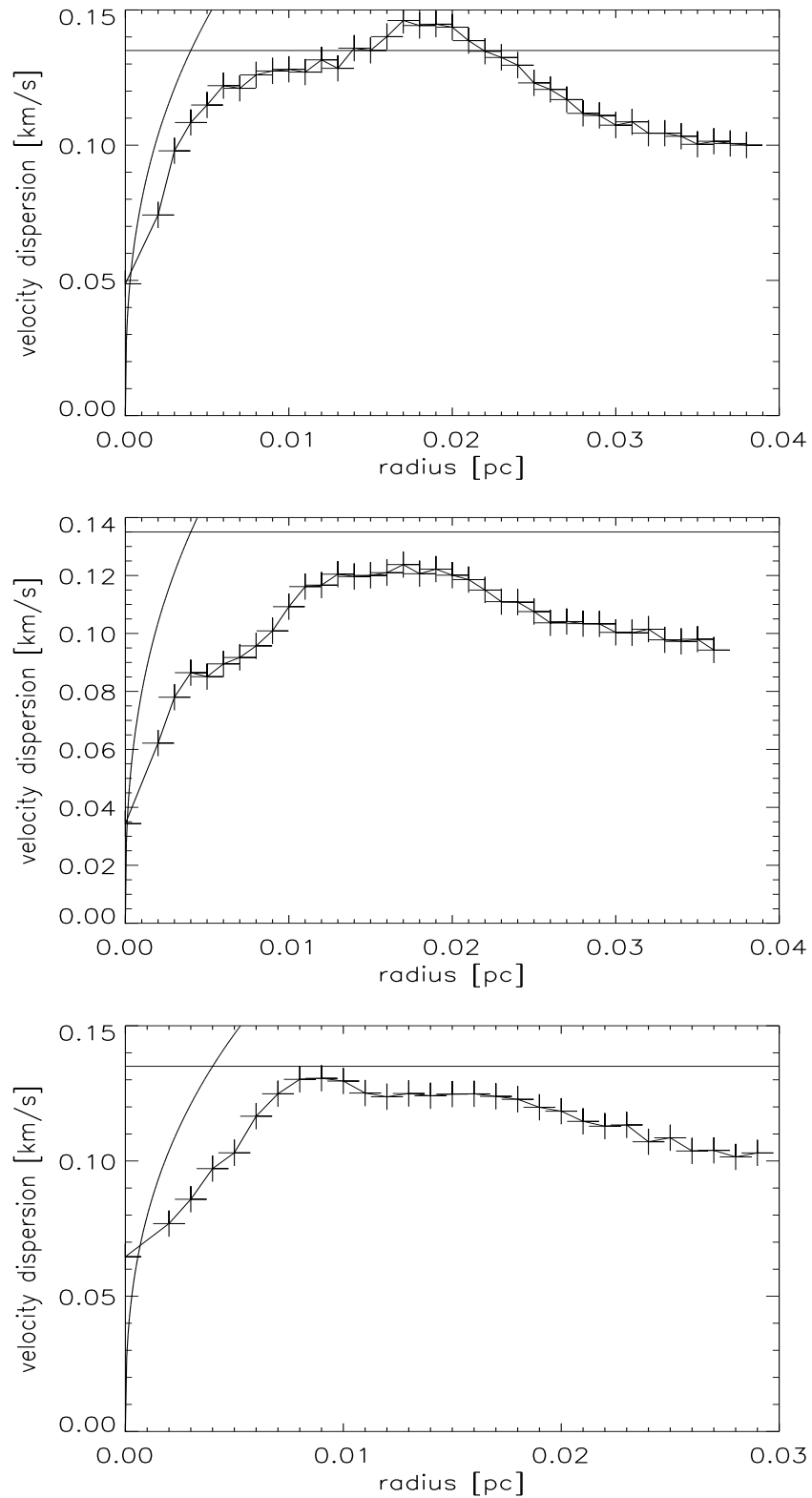
Figure 5.26: **Velocity dispersion in shells around the density maximum (run425) at t=100000 yrs (upper panel), t=150000 yrs (middle panel) and t=175000 yrs (lower panel) after the initialization. The horizontal line at** $\sigma = 0.75\,c_s$ **gives a typical observational value for the innermost parts of prestellar cores.**

Chapter 6

Collapse Calculations

6.1 The Opacity Limit

When a molecular cloud core begins to collapse from densities $\approx 2 \times 10^{-19}\,\mathrm{g/cm^3}$ the gravitational potential energy that is released can easily be radiated away so that the collapsing gas is approximately isothermal (e.g.Larson (1969)). Thus, the thermal pressure varies with density ρ as $p \propto \rho^{\eta}$ with the polytropic exponent

$$\eta \equiv \mathrm{d}\log(p)/\mathrm{d}\log(\rho) \approx 1 \qquad (6.1)$$

This allows subsequent fragmentation because the Jeans mass decreases with increasing density as long as $\eta < 4/3$.

The opacity limit for fragmentation occurs when the timescale on which energy is released by the collapse exceeds the one at which energy is radiated away (Rees (1976); Low and Lynden-Bell (1976); Masunaga and Inutsuka (1999)). The gas then heats up with $\eta > 4/3$ and the Jeans mass increases. As a result, a Jeans unstable collapsing clump transforms into a Jeans stable one and a pressure supported fragment is formed. The density at which this occurs depends on the opacity of the gas, hence the term 'opacity limit for fragmentation' and on the geometrical structure and size of the fragments. Via the opacity there are introduced further dependencies like the initial temperature and the gas to dust mass ratio (Masunaga and Inutsuka (1999)). For molecular gas at an initial temperature of about 10 K a typical sized fragment begins to heat significantly at a density of $\rho \approx 10^{-13}\,\mathrm{g/cm^3}$ (Larson (1969); Masunaga and Inutsuka (2000)).

A fragment reaching the opacity limit becomes pressure supported and initially contains several Jupiter-masses ($\mathrm{M_J}$). It's size scale is $\approx 5\,\mathrm{AU}$ (Larson (1969)). This results from a Jeans analysis for the gas density at the opacity limit. Because the fragment is embedded in a collapsing envelope it is expected to grow further in mass and density. The fragment transforms into a optically thick hydrostatic core and as a direct consequence the central temperature increases. When its central temperature reaches 2000 K, molecular hydrogen begins to dissociate. This provides a way to release gravitational energy without significantly increasing the temperature of the gas. Even though the temperature is roughly constant additional pressure emerges from the fact that the number of gas particles is increased. As a result, a second collapse occurs within the fragment (with a polytropic index of $\eta = 1.15$) that ultimately results in the formation of a stellar core with radius of approximately $1\,\mathrm{R_\odot}$ Larson (1969).

Several studies have investigated the possibility of fragmentation during this second collapse (Boss (1989); Bonnell and Bate (1994b); Bate (1998b)). Boss (1989) found that fragmentation was possible during this second collapse, but that the objects spiraled together and merged due to gravitational torques from a non-axisymmetric structure. Bate (1998b) performed the first three-dimensional calculations to follow up the entire collapse evolution starting from a molecular cloud core through fragmentation, the formation of the pressure supported fragment, the second collapse phase, and the formation of the stellar core and its surrounding disc. In these calculations he found that the second collapse is not a regime of further sub-fragmentation.

The existence of the opacity limit suppresses the fragmentation process if the density exceeds $\approx 10^{-13}$ g/cm^3. This results in a a minimum 'stellar' mass of ~ 10 Jupiter-masses (M$_J$) (Low and Lynden-Bell 1976; Silk 1977a, Boss 1988) and a minimum protobinary separation separation of ≈ 10 AU due to the sizes of the pressure-supported fragments. The exact value of the minimum mass is uncertain with theoretical values ranging from $1 - 10$ M$_J$ (Low and Lynden-Bell 1976; Silk 1977a; Boss 1988; Masunaga and Inutsuka 1999; Boss 2001). Surveys of young star clusters are beginning to probe masses down to this theoretical minimum mass (Zapatero Osorio et al. 1999; Lucas and Roche 2000; Béjar et al. 2001; Martín et al. 2001b; Lucas et al. 2001), with the masses of some objects estimated to be as low as 3 M$_J$ (Zapatero Osorio et al. 2002a; McCaughrean 2003). Up to now observational uncertainties are too large so that the predicted cutoff in the mass function is still no detected.

6.2   Variable Equation of State

To model the opacity limit (see section 3.5.3) without taking into account radiative transfer , we use a variable equation of state for the thermal pressure of the gas:

$$p \;=\; K\rho^{\eta} \tag{6.2}$$

The value of K is defined such that when the gas is isothermal $K = c_{\rm s}^2$. The resulting sound speed is then $c_{\rm s} = 1.84 \times 10^4$ cm/s. The value of the polytropic exponent η, is varied with density:

$$\eta = \left\{ \begin{array}{ll} 1, & \rho \leq 10^{-13} \text{ g cm}^{-3}, \\ 1.4, & \rho > 10^{-13} \text{ g cm}^{-3}. \end{array} \right. \tag{6.3}$$

Note, that the function $p(\rho)$ is still continuous in spite of the abrupt change in η .

This equation of state has been chosen to match closely the relationship between temperature and density during the spherically-symmetric collapse of molecular cloud cores as calculated with frequency-dependent radiative transfer (Masunaga, Miyama, & Inutsuka 1998; Masunaga & Inutsuka 2000). A comparison of our simple parameterization with Masunaga and Inutsuka's temperature-density relation is given in figure 3.1. Our parameterization reproduces the temperature-density relation to an accuracy of better than 20% in the non-isothermal regime up to densities of 10^{-8} g/cm^3. Test calculations of the spherically-symmetric collapse of a molecular cloud core using this equation of state have been performed (Bate 1998, 2002) and give excellent agreement with the results of Larson (1969) and Winkler Newman (1980a,b) for the mass and size of the pressure-supported fragment that forms. Thus, our equation of state should model collapsing regions well, but may not model the equation of state in protostellar discs particularly accurately due to the departure from spherical symmetry.

6.3 Sink Particles

The opacity limit for fragmentation results in a change of the pressure support of the fragments. Further fragmentation is suppressed and an accretion process sets in increasing the total mass and the central density of a fragment. At this stage it becomes computationally impractical and very time consuming to follow up the internal evolution. This is due to the short dynamical time-scales in the high density opaque regions. In addition, these regions (due to the adiabatic heating) evolve into roughly spherical objects with no interesting substructure worth to be resolved. Therefore, when the central density of a pressure supported fragment exceeds $\rho_{\mathrm{s}} = 10^{-11} \,\mathrm{g/cm^3}$, we insert a sink particle into the calculation (Bate et al. (1995)). More technically a sink particle is created if the density threshold is exceeded by at least 50 SPH particles. It is placed at the position of the densest gas particle of the pressure-supported fragment. It swallows all SPH particles contained within $r_{\mathrm{acc}} = 14 \,\mathrm{AU}$ around it and adopts their mass and momentum. Any gas that later falls within this radius is accreted by the point mass if it is bound and its specific angular momentum is less than that required to form a circular orbit at radius r_{acc} from the sink particle. Thus, gaseous discs around sink particles can only be resolved if they have radii of at least $\geq 20 \,\mathrm{AU}$. Sink particles interact with the gas only via gravity and accretion.

Since all sink particles are created from pressure-supported fragments, their initial masses are $\approx 10 \,\mathrm{M_J}$, as given by the opacity limit for fragmentation (section 6.1). Subsequently, they may accrete large amounts of material to become higher-mass brown dwarfs ($m \leq 75 \,\mathrm{M_J}$) or stars ($m \geq 75 \,\mathrm{M_J}$), but *all* the stars and brown dwarfs begin as these low-mass pressure-supported fragments. Sink particles are not permitted to merge in this calculation.

The high density contrasts occurring in our simulations result in a wide range of integration timesteps for the individual SPH particles. If a large fraction of the SPH particles are accumulated in high density regions the global integration speed breaks down. This is the case when hydrostatic cores start to form. But the hydrostatic cores are not expected to host interesting substructure due to their pressure supported nature and are in this sense 'boring, roughly spherical objects' not worth to be resolved in detail. Therefore, the creation of sink particles is a skillful method to avoid the extremely time consuming calculation of the detailed dynamics in the hydrostatic cores.

This is not without an element of risk. If it were possible to follow the fragments all the way to stellar densities (as done by Bate 1998) while continuing to follow the evolution of the large-scale cloud over its dynamical time-scale, we might find that a few of the objects that we replace with sink particles merge together or are disrupted by dynamical interactions. We have tried to minimize the degree to which this might occur by insisting that the central density of the pressure-supported fragments is at least two orders of magnitude higher than the opacity limit before a sink particle is created. This ensures that the fragment is adiabatically heated up to 60K, self-gravitating, centrally-condensed and roughly spherical before it is replaced by a sink particle. Furthermore, each pressure-supported fragment must undergo a period of accretion before its central density exceeds ρ_{s} and it is replaced by a sink particle. In principal there is the possibility for a very filamentary collapsing fragment to exceed this density over a large distance, thus making the creation of one or more sink particles ambiguous. However, the structure of the collapsing fragments resulting from our turbulent initial condition does not evolve into long, roughly uniform-density filaments with $\rho \approx \rho_{\mathrm{s}}$.

6.4   Resolution

The local Jeans mass must be resolved throughout the calculation to model fragmentation correctly (Bate & Burkert 1997; Truelove et al. 1997; Whitworth 1998; Boss et al. 2000). Bate and Burkert (1997) found that this requires at least $\geq 2N_{\text{neigh}}$ SPH particles per Jeans mass.

Bate found in more detailed tests with calculations using different numbers of particles that $1.5 N_{\text{neigh}} = 75$ particles are also sufficient to resolve the local Jeans mass, see section 3.4.2 The minimum Jeans mass in our calculations occurs at the maximum density during the isothermal collapse phase ($\rho = 10^{-13} \, \text{g/cm}^3$), and is $M_{Jeans,min} \approx 0.003 M_\odot$. Thus 0.75×10^5 particles are needed to model the collapse of $3 M_\odot$ prestellar cores down to the opacity limit.

6.5   Ensemble Runs

We have performed an ensemble of 22 independent collapse simulations. Besides the structure of the initial velocity field the setup conditions are identical for all runs:

geometry	homogeneous density sphere
mass	$m = 3 \, \text{M}_\odot$
size	$R = 0.0616 \, \text{pc}$
density	$2.1 \times 10^{-19} \, \text{g/cm}^3 \ (5.3 \times 10^4 \, 1/\text{cm}^3)$
mean molecular weight	$\mu = 2.36 \, \text{g/mol}$
temperature	$T = 10 \, \text{K}$
initial Mach number	$M_0 = 2.0$

The velocities of the SPH particles are generated by the method of Gaussian Random Fields as described in detail in chapter 4.3.2. A power spectrum $P(k) \sim k^{-4}$ is used which is consistent with most of the observed line width-size relations, see section 4.3.1. The largest mode has the same size as the setup spheres' diameter ($k_{min} = 1$). The smalest resolvable mode for the velocity fluctuations is 1/21 of the spheres' diameter ($k_{max} = 21$).

Due to the individual density structures and flows the time of the first formation of a sink particle varies significantly. The earliest formation takes place $1.16 \, t_{\text{ff}}$ (run595), the latest one $1.84 \, t_{\text{ff}}$. The following table gives a summary of all 22 runs. Shown is the time step at which the first sink particle is formed (second column), the final time step of the calculation (third column), how many sink particles where created up to the end of the calculation (fourth column) and the total amound of mass accreted by all sink particles at the end of the calculation (fifth column). One free fall time corresponds to 31 timesteps.

run	first sink particle	last timestep	final number of sink particles	accreted mass
run310	37	150	13	2.45 (81.6%)
run315	57	103	9	1.56 (52.1%)
run320	49	56	9	1.11 (36.9%)
run325	35	454	9	1.58 (52.8%)
run360	42	137	8	2.24 (74.6%)
run365	50	467	15	1.77 (58.9%)
run370	39	70	9	1.59 (53.1%)
run375	40	191	9	1.96 (65.3%)
run410	40	96	1	1.87 (62.5%)
run415	40	301	12	2.32 (77.3%)
run420	39	54	7	1.47 (49.0%)
run425	38	65	11	1.73 (57.8%)
run475	48	99	9	2.27 (75.8%)
run510	38	177	18	1.82 (60.8%)
run580	37	67	10	1.73 (57.6%)
run585	37	78	11	1.61 (53.7%)
run590	49	72	3	1.29 (43.0%)
run595	36	66	10	1.29 (43.0%)
run610	51	64	9	2.00 (66.8%)
run615	34	42	1	1.60 (53.4%)
run620	36	44	10	1.66 (55.4%)
run625	44	51	1	0.43 (14.3%)

As expected due to the large fraction of binary and multiple systems seen in observations there is a large scatter in the number of objects created from the individual prestellar cores of our simulations. It comes out, that there are two distinct formation mechanisms forming primarily stars respective brown dwarfs:

- The formation of objects directly from collapsing fragments contracting beyond the opacity limit. In our simulations these objects nearly always exceed the hydrogen burning limit and become stars. The mean mass of these stars is $0.47\,M_\odot$.

- The formation of objects from a massive accretion disk as it evolves into an instability. These objects are on average significantly smaller in mass than the ones formed directly from fragments. About 60 percent of these objects do not exceed the hydrogen burning limit. So that we can predict that this formation scenario is typical for the formation of brown dwarfs. The mean mass of the objects formed by this mechanism is $0.1\,M_\odot$.

The most simple example for the first formation mechanism is the creation of a single star. This is shown in figure 6.1. In run410 (upper panel) a single star accretes mass from a stable disk. The accretion phase has been followed over one free fall time (150000 yrs). The single object is formed 200000 yrs after the initialization. During the first 50000 yrs after its creation it accretes rapidly about 80 percent of its final mass. Later on the gas reservoir becomes exhausted and the accretion rate decreases. One should keep in mind, that our

simulations do not take into account feedback mechanisms like outflows and heating of the
surrounding disk and envelope. So that our accretion rates and final masses have to be
interpreted as upper limits. In our ensemble the first scenario is dominated by the formation
of single stars. However, the majority of objects formed by this scenario is initially in binary
or multiple systems. The following table shows the number of stars formed directly from
collapsing fragments:

one single star	12	runs	
two stars	6	runs	4 binaries
			2 unbound systems
multiple systems	4	runs	

If two objects are formed by collapsing fragments they are often close together in space and
time. In this case the second component forms not more than 5000 years after the first one.
Figure (6.3) shows a competitive accreting binary system. Over 70000 yrs the binary system
is not perturbed by formation of other objects or interaction with other objects. In this case
the orbital parameters converging towards an elliptical orbit with a semi-mayor axis of 21 AU
and an eccentricity of 0.64. During the first 20000 yrs the stars migrate together and their
orbit is circularized. Accretion rates are in the order of 10^{-5} M$_\odot$/yr, see figure (6.3). Later on
the inward migration stops and the orbital parameters are roughly constant besides a slowly
increasing eccentricity. During the whole accretion phase the binary masses are equalized
(lower panel of figure 6.3). At the end of the calculation the accretion rate has decayed down
to 5×10^{-7} M$_\odot$/yr. The total accreted mass end up with 1.05 M$_\odot$ and a mass ratio of 1.5. The
period has converged against 120 yrs which is typical for binaries and just at the maximum
of the observed period distribution (Duquennoy and Mayor (1991)).
A more typical star formation scenario of our ensemble is shown in figure 6.5. It consists
of both, the formation of one or more objects from collapsing fragments *and* the subsequent
formation of objects from an unstable massive accretion disk. About 2500 yrs before the disk
instability occurs the accretion rate starts to increase again reaching values of 10^{-4} M$_\odot$/yr.
Once the small objects have formed in the disk the accretion on the massive object decreases
significantly and is comparable to the accretion rates of the other new born objects in the
disk. Two of the disk born objects are ejected out of the dense gas regions soon after there
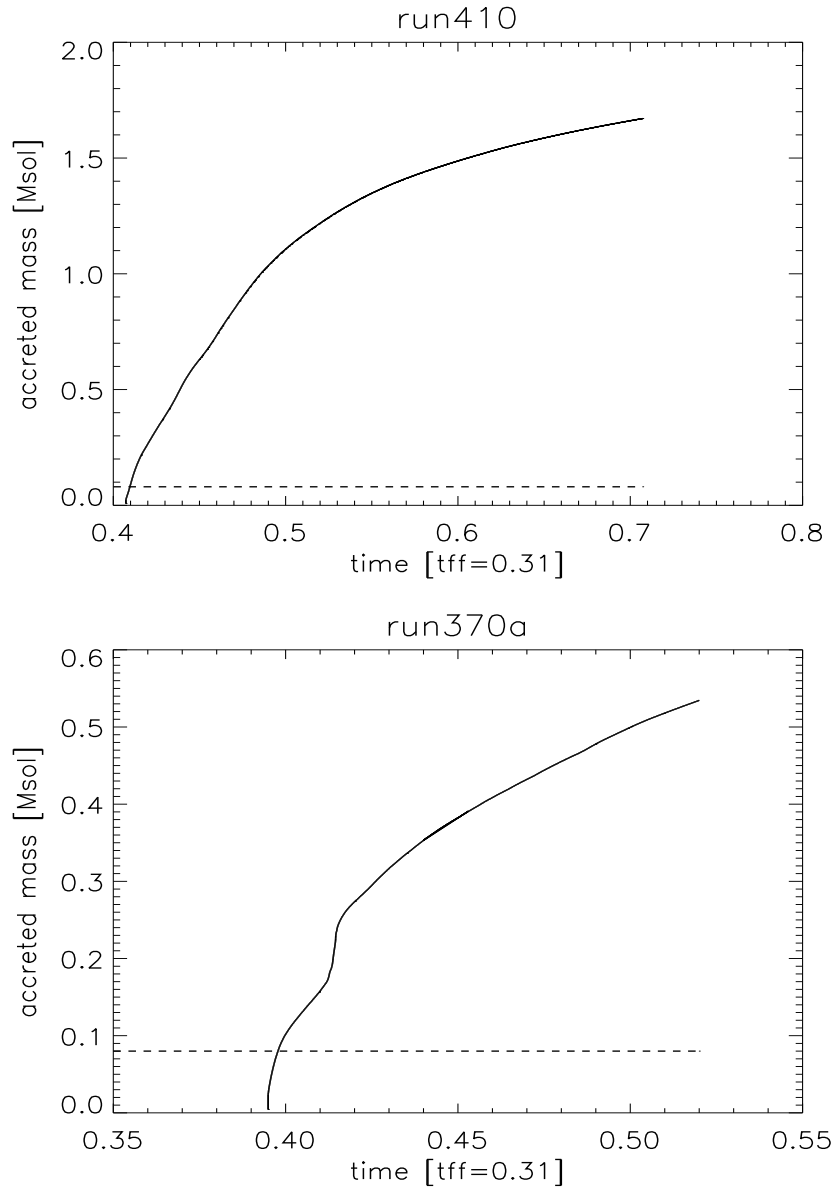creation and do not accrete any more.

Figure 6.1: **Two example runs showing an extended calm accretion phase after the creation of a single sink particle. Plotted is the mass accreted by the sink particle in units of $M_\odot$ as a function of time. The dashed horizontal marks the hydrogen burning limit of $0.08\,M_\odot$. Objects above the dashed line are stars, objects below are brown dwarfs. The time axis is scaled in code units: $0.31\,CU = t_{ff} = 150000\,\mathrm{yrs}$.**

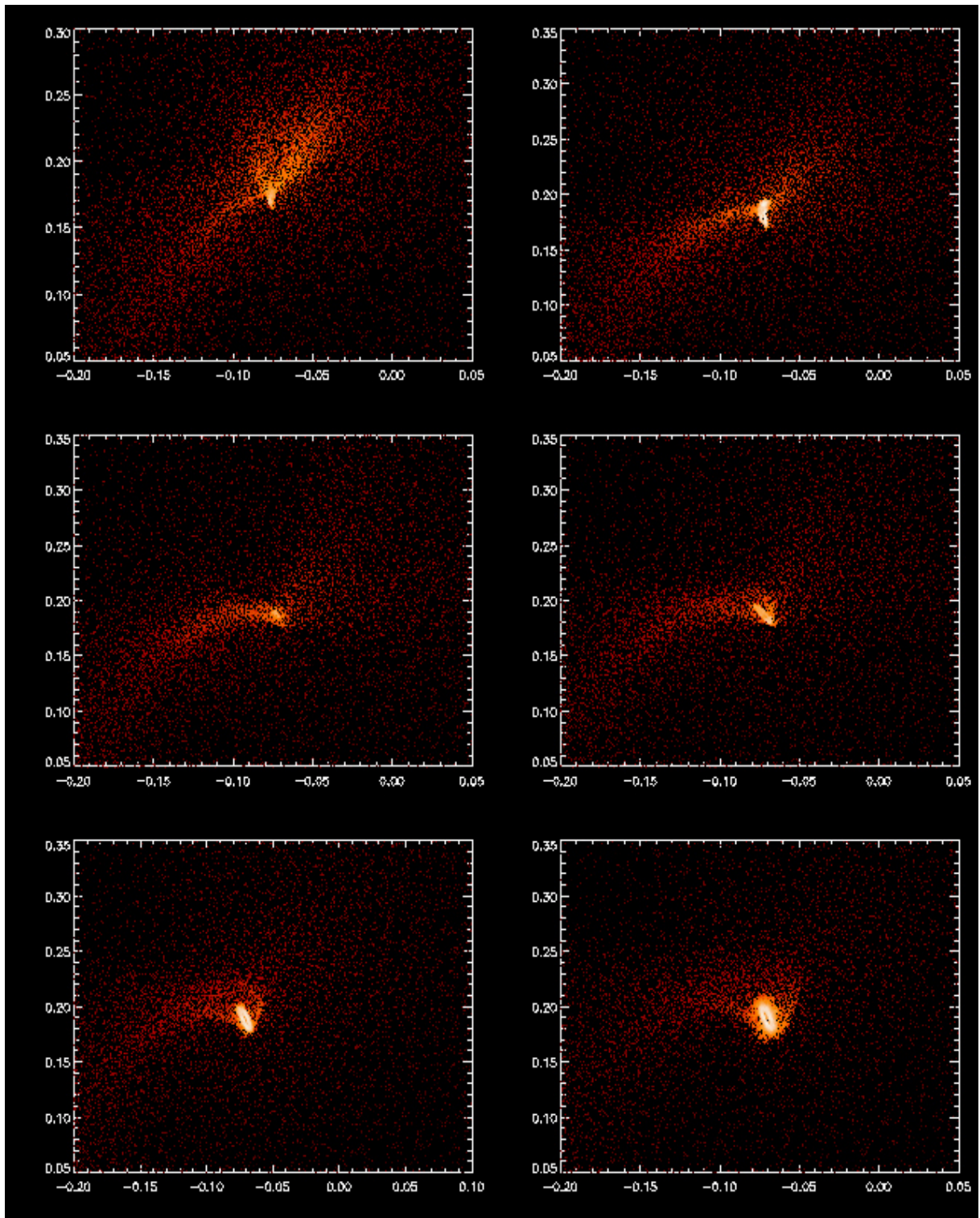Figure 6.2: **Logarithmic density distribution (color coded) for a stable circumstellar disk (run410) from 200000 yrs (upper left) to 225000 yrs (lower right) after the initialization (upper left) in steps of 5000 yrs. Densities range from 0.3 resp. 2×10^{-20} g/cm^3 (black) to 2.5×10^7 resp. 1.6×10^{-12} g/cm^3 (white). Size scales are given in units of 0.1 pc.**
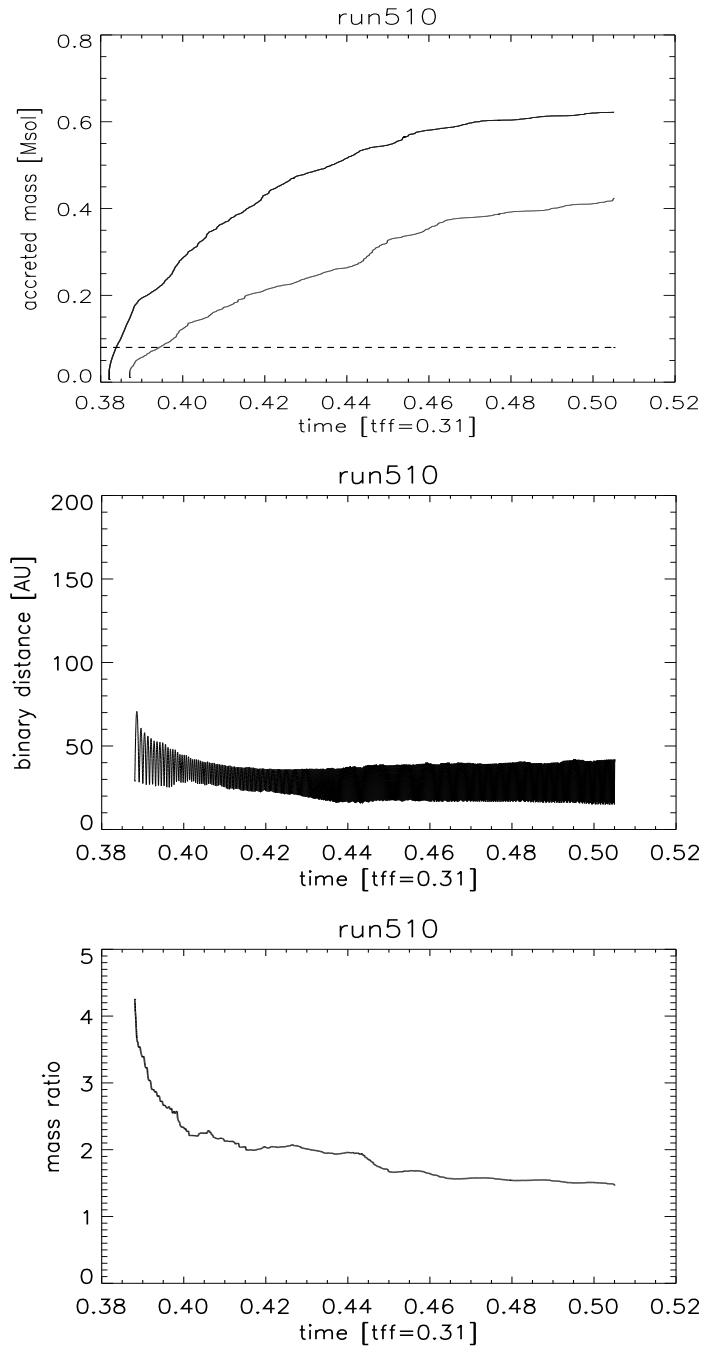
Figure 6.3: **Competitive accretion in a binary system (upper panel), distance of the binary objects (middle panel) and the mass ratio of the objects (lower panel). The time axis is scaled in code units:** $t_{ff} = 0.31\,CU = 150000\,yrs$.
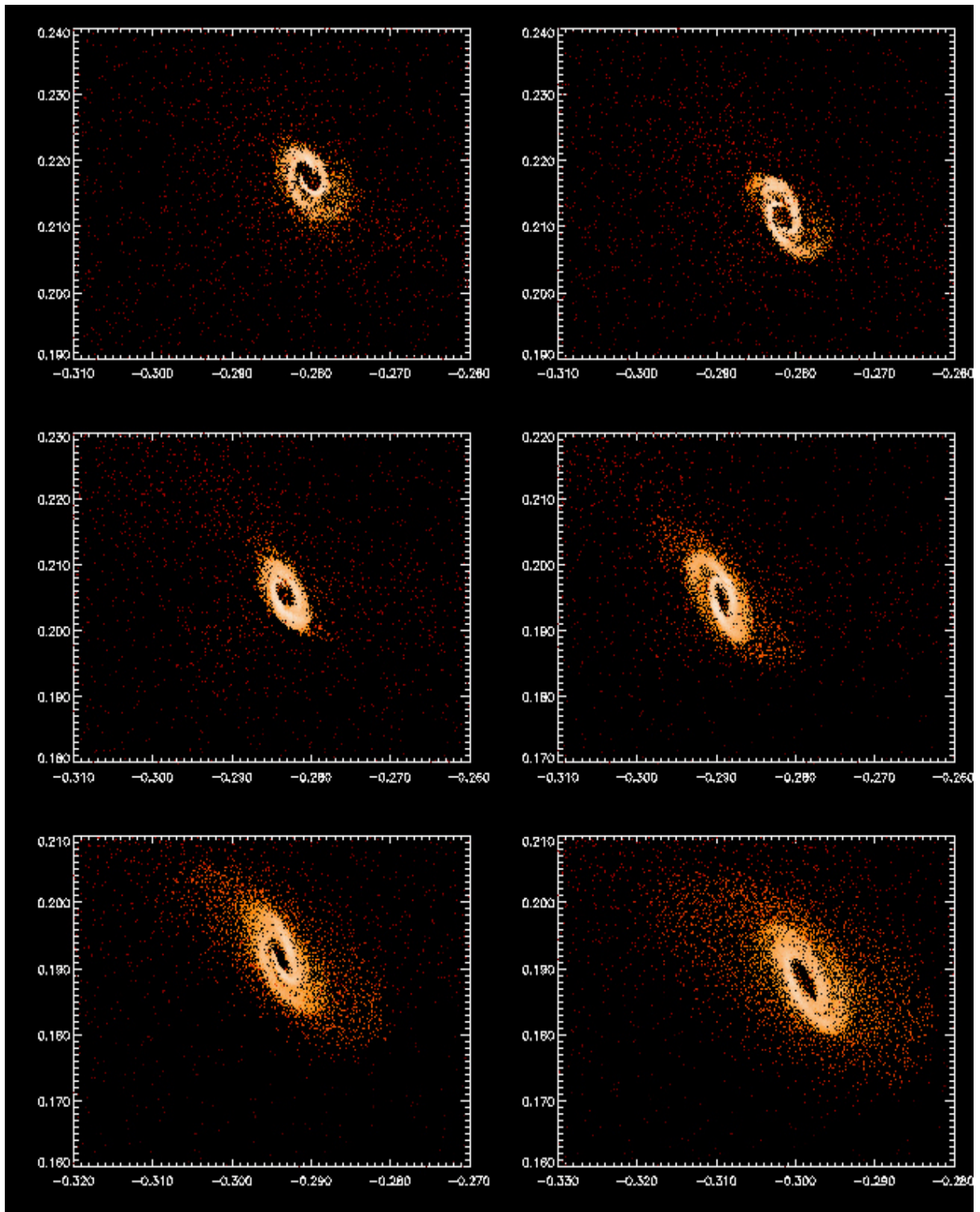
Figure 6.4: **Logarithmic density distribution (color coded) of a circumbinary disk (run510) 200000 yrs (upper left) to 225000 yrs (lower right) after the initialization in steps of 5000 yrs. The binary is located in the low density hole at the disk's center. Densities range from 0.3 resp. 2×10^{-20} g/cm^3 (black) to 2.5×10^7 resp. 1.6×10^{-12} g/cm^3 (white). Size scales are given in units of 0.1 pc.**
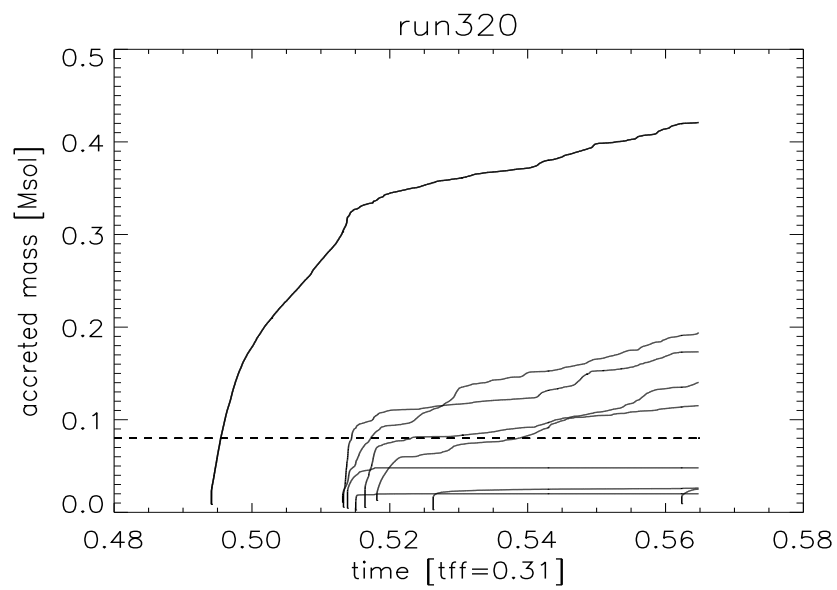
Figure 6.5: **Fast accretion of a single object from a massive disk. A disk instability occurs at** $t = 0.51$ **resulting in a star formation burst 10000 yrs after the formation of the first stellar object. The time axis is scaled in code units:** $0.31CU = t_{ff} = 150000\,\mathrm{yrs}.$
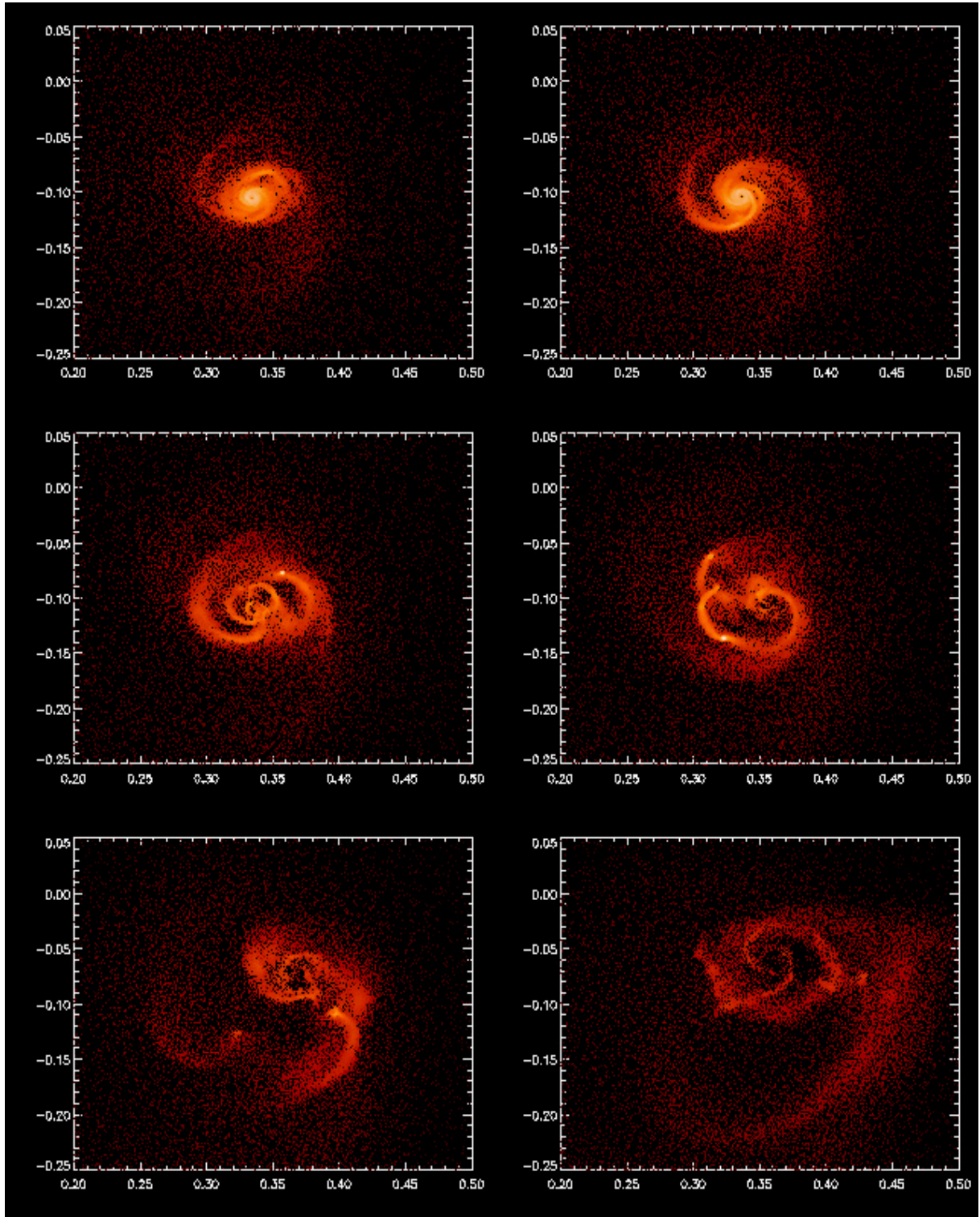
Figure 6.6: **Logarithmic density distribution (color coded) for an circumstellar disk evolving into an instability which results in the creation of 4 low mass stars and 4 brown dwarfs. The time sequence range from 200000 yrs (upper left) to 225000 yrs (lower right) after the initialization in steps of 5000 yrs. Densities range from 0.3 resp. 2×10^{-20} g/cm^3 (black) to 2.5×10^7 resp. 1.6×10^{-12} g/cm^3 (white). Size scales are given in units of 0.1 pc.**

6.6 Binary Stars

The majority of stars are binary or multiple systems, but yet multiple star formation is only partly understood. Multiple star formation is a fundamental feature of the star formation process itself. Duquennoy and Mayor (1991) have presented a survey with all known F7-G9 stars within a 22 pc sphere around the sun. This survey provides a relatively unbiased sample of main-sequence stars.

- *Frequency:* In the sample of Duquennoy and Mayor (1991) the ratio of the number of single:binary:triple:quadruple systems is 57:38:4:1. That applies for companions with a mass ratio $q = M_2/M_1 > 0.1$. This means that only about 40 percent of the stars are single stars. The binary frequency among pre-main-sequence stars is about twice as large as for the main-sequence stars of the Duquennoy and Mayor (1991) sample.

- *Period Distribution* The period distribution of the sample of Duquennoy and Mayor (1991) is Gaussian like as a function of $logP$ with a median of $P \approx 6 \times 10^4$ days. The periods range from less than a day to 10^9 days. Multiple systems are ordered hierarchically. Short period systems are part of larger long period system etc. Mathieu (1994) showed the periods to be similar distributed for pre-main-sequence stars.

- *Mass Ratios:* The Duquennoy and Mayor (1991) sample shows a Gaussian distribution of the mass ratios with a maximum at $q = 0.23$. A similar distribution was found by a survey of field stars Kroupa et al. (1990).

- *Orbital Eccentricities:* Binaries with periods $P < 11$ days have circular orbits. Orbits with periods $10 < P < 1000$ days show eccentricities essentially below $e = 0.6$. Orbits with periods $P > 1000$ days eccentricities are scattered between $e \approx 0.1$ and $e \approx 0.9$. These results are taken again from the Duquennoy and Mayor (1991) sample. A sample of pre-main-sequence stars Mathieu (1994) shows that the eccentricity distribution (as a function of P) is similar to that of main-sequence stars except for short periods. Circular orbits are only seen for periods below $P = 5$ days.

6.6.1   Formation Theories for Binary Systems

There are essentially four general models for the formation of binary star systems.

- *Caption:* The mechanism of caption was suggested for the first time by Stoney (see Aitken 1935). Two independently formed and initially unbound stars form a binary system due to some dissipative process e.g. tidal dissipation during a close encounter. Another possibility is the formation of a binary system in the presence of a third object which absorbs the excess energy.

- *Fission:* Binary formation by fission occurs when a hydrostatic core or protostar during its quasi-static contraction phase run into an rotational instability and disrupts into two distinct objects. In such a process spin angular momentum is converted into orbital angular momentum. If this process will occur after the second collapse phase it will be a source of close binaries. There are numerous objections against this theory (e.g. Tassoul (1978), Bodenheimer et al. 1993). Numerical simulations do not show binary formation by this process.

- *Fragmentation during Protostellar Collapse:* Originally proposed by Hoyle (1953) fragmentation during the protostellar collapse phase can produce binaries with a wide range of periods. The fragmentation mechanism was tested in a large number of numerical simulation. A wide variety of initial conditions has been employed.

- *Disk Fragmentation* Disk fragmentation can occur in an equilibrium circumstellar disk if the minimum value for the Toomre Parameter Q approaches 1.

In our ensemble we have found 17 binary stars and 6 hierarchical triple systems consisting of a close binary system with distant companion star. Two of the binary systems are brown dwarf binaries. The following table gives a summary of all bound objects found in our sample.

run	major component [$M_\odot$]	minor companion [$M_\odot$]	major axis[AU]	minor axis [AU]	period [yrs]
run310					
run315	$m_1 = 0.4122$	$m_2 = 0.1790$	29	14	70.53 p
	$m_1 + m_2 = 0.5910$	$m_0 = 0.5798$	295	260	2978 p
run320	$m_0 = 0.4209$	$m_1 = 0.1733$	25	10	78 im
run325	$m_0 = 0.7270$	$m_2 = 0.2624$	66	37	256.5 p
	$m_1 = 0.1748$	$m_6 = 0.1016$	1540	30	26450 v
	$m_0 + m_2 = 0.9894$	$m_5 = 0.05364$	1100	800	19749 v
run360					
run365	$m_{11} = 0.2444$	$m_{13} = 0.1007$	80	10	352.7 p
	$m_0 = 0.4606$	$m_1 = 0.1277$	550...1200	25...30	4702...14106 o
run370	$m_0 = 0.6373$	$m_1 = 0.2064$	29...38	6...12	56.4...78.4 v
	$m_0 = 0.6373$	$m_2 = 0.2195$	41	17	110 p
	$m_0 + m_2 = 0.8567$	$m_1 = 0.2064$	400...600	100	2821 d
run375	$m_0 = 0.4819$	$m_1 = 0.3424$	49	17	145.5 d
	$m_0 + m_1 = 0.8243$	$m_5 = 0.3770$	400...600	175	3582 i
run410					
run415	$m_4 = 0.1440$	$m_7 = 0.0654$	550...800	10...15	8041...11400 v
run420	$m_0 = 0.8324$	$m_1 = 0.3067$	33...35	11...15	70 p
run425	$m_0 = 0.6922$	$m_2 = 0.1978$	28...30	10...12	65 v
	$m_1 = 0.2572$	$m_5 = 0.4307$	120...150	8...15	562 d
	$m_0 + m_2 = 0.89$	$m_5 = 0.4307$	270...325	80...105	1840 v
run475	$m_8 = 0.6812$	$m_{12} = 0.2441$	19...23	8...10	437 i
	$m_0 = 0.3276$	$m_2 = 0.0933$	170...200	8...10	1051 i
run510	$m_0 = 0.6220$	$m_1 = 0.4245$	42	15	120 p
run580					
run585	$m_3 = 0.3106$	$m_1 = 0.2003$	105...125	15...45	526 v
	$m_7 = 0.2424$	$m_6 = 0.2330$	128...135	30...40	728 i
run590					
run595	$m_3 = 0.07824$	$m_7 = 0.03248$	95	35	111 i
	$m_6 = 0.0342$	$m_8 = 0.0271$	950	100	35477 p
run610	$m_0 = 0.6133$	$m_1 = 0.4136$	63...70	20...45	208 v
	$m_6 = 0.0884$	$m_7 = 0.0514$	15...25	5...10	368 c
run615					
run620	$m_2 = 0.2144$	$m_1 = 0.1094$	20...24	10...17	195 mt,c
	$m_0 = 0.409$	$m_1 + m_2 = 0.3238$	130...170	80...90	1242 mt,c
run625					

The small letters behind the period numbers indicate the evolutionary character of the orbit: (p)=periodic ; (c)=chaotic ; (i)=inward migration ; (o)=outward migration ; (d)=decaying orbit ; (im)=intermitency=binary jumps between periodic and chaotic epochs

6.6.2   Period Distribution

The period distribution resulting from our ensemble calculations is consistent with distributions measured among solar type stars (e.g. Duquennoy and Mayor (1991)). If one looks at the distribution for the pre-main sequence stars (figure 6.8) the concordance is even better except for periods $< 10^3$ days.

On the low end of the period distribution we are restricted by the accretion radii of our sink particles. This introduces a minimum initial distance for the binaries of $2r_{\mathrm{acc}} = 28\,\mathrm{AU}$. If we assume an initial mass for both objects of $0.25\,\mathrm{M_\odot}$ we get a lower limit of 200 yrs for the initial period. On the other hand there is a minimum size for fragments at the opacity limit of about $10\,\mathrm{AU}$. This introduces a physical minimum initial distance of roughly $20\,\mathrm{AU}$. This is nicely confirmed by high resolution simulations of Bate et al. (2002b) and references there. Once created sink particles are able to migrate together which is a common scenario during the accretion phase so that we find about 30% of the periods to be below 200 yrs at the end of the calculation. Nevertheless we have to keep in mind that we can't expect correct number counts for the period distribution far below 100 yrs because the accretion disks are not resolved beyond $20\,\mathrm{AU}$. On the high end of the period distribution we are naturally restricted by the size of our simulation area. We can't expect a binary system to be created with an initial distance of more than $0.06\,\mathrm{pc}$. This results in period of the order of 10^8 days. But this restriction also holds in nature because stellar objects can only form inside prestellar cores and these have sizes in the order of our simulation area. Even though our sink particles are not restricted to the simulation area of the SPH particles and a significant part has left this area at the end of the calculation the longest period we found in our calculations is 1.3×10^7 days.
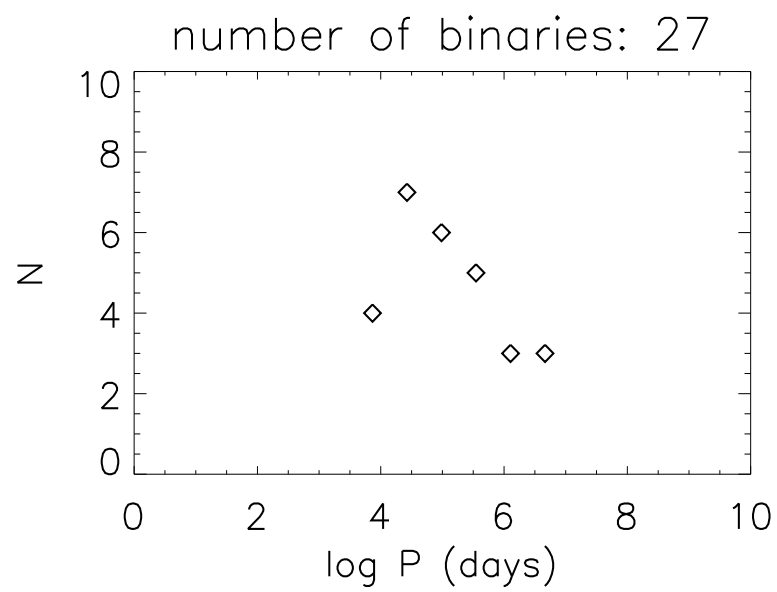
Figure 6.7: **Period distribution for 17 binary and 6 hierarchical triple systems (counted double) resulting from our ensemble calculation. The maximum fits well the period distribution of solar neigbourhood stars, compare with figure 6.8**
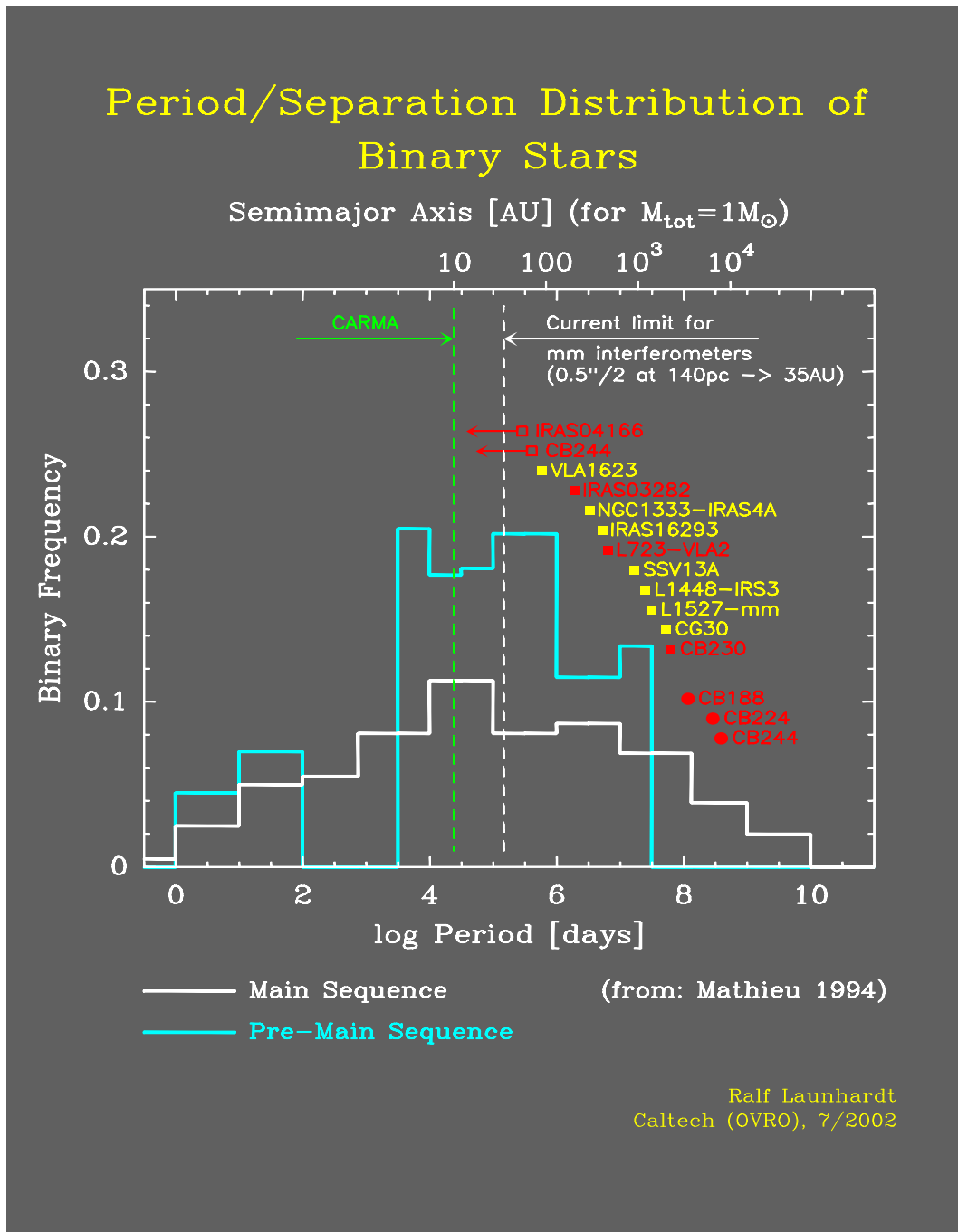
Figure 6.8: **Comparison of the period distributions of Main Sequence stars (grey), Pre-Main-Sequence stars (blue) and class 0 binary objects observed in submm (red and yellow dots). The figure was provided by Ralf Launhardt.**

6.6.3 Eccentricities

Observations show that main-sequence binaries with periods $P < 11$ days have circular orbits. In the period range $10 < P < 1000$ days eccentricities are measured to be below $e = 0.6$ and there is a significant correlation between revolution period and eccentricity. For orbits with periods $P > 1000$ days eccentricities are independent of P and scattered between $e \approx 0.1$ and $e \approx 0.9$ (Duquennoy and Mayor (1991)).

In samples of pre-main-sequence binaries eccentricities tend to be larger compared to main-sequence samples for periods $P < 1000$ days . In particular the period range in which orbits are found to be circular is much smaller and extends not beyond $P = 5$ days (Mathieu (1994)).

The fact that old binary systems have statistically more circular orbits than young systems can be explained by tidal interactions. In the course of time rotational angular momentum of the stars is transfered to the orbital angular momentum resulting in a circularisation of the corresponding orbits.

The amount of transfered angular momentum per time depends on the strength of the tidal interaction, the rotation periods of the stars and the period of revolution. The timscale on which orbits are circularized is shortest for close binaries because of strong tidal interactions and short revolution periods. For periods beyond 10^5 days respective distances $d > 50\,\mathrm{AU}$ the effect of circularization is not seen any more in the sample of Duquennoy and Mayor (1991) (figure 6.9 , lower panel). For this systems the timescale for circularisation is in the order of 5×10^9 yrs or more and/or the amount of rotational angular momentum of the stars is insufficient to circularize the stellar orbits significantly.

In our ensemble eccentricities become independent of the revolution period for periods $P > 1000$ days. As expected we don't find completely circularised orbits because the shortest period of our sample ($P = 70$ days) is far beyond the regime where orbits are expected to be circularized.
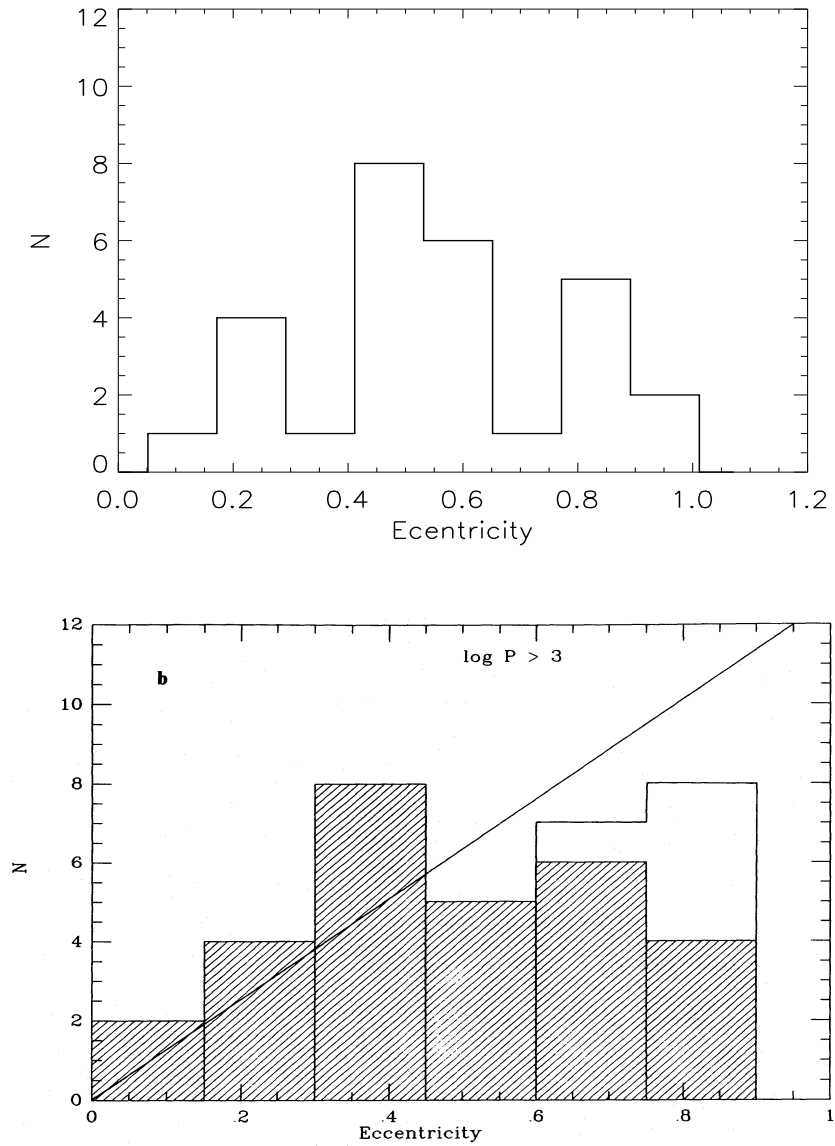
Figure 6.9: **Comparison of the Eccentricity Distribution resulting from our ensemble runs with the Eccentricity Distribution of solar neigbourhood stars, taken from Duquennoy and Mayor (1991)**
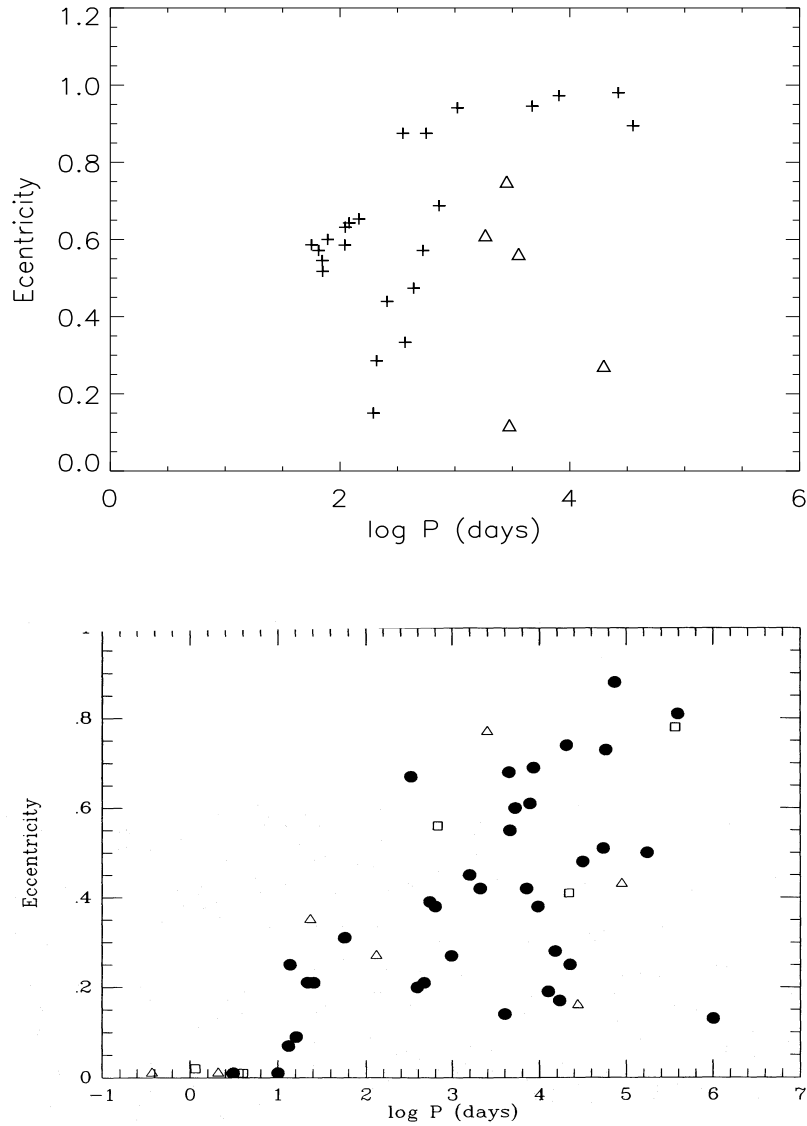
Figure 6.10: **Comparison of the Eccentricity-Period relation resulting from our ensemble runs (upper panel) with the Eccentricity-Period relation of solar neighbourhood stars (lower panel), taken from Duquennoy and Mayor (1991). Crosses and black disks are binary systems, triangles are triple systems and Squares are quadruple systems. Note the different ranges on the horizontal axis. Due to our resolution limits we have no binary periods below 100 days.**

6.7   Brown Dwarfs

The existence of brown dwarfs was convincingly demonstrated the first time in 1995 by the discovery of Gliese 229 which is the companion of a M dwarf star (Nakajima et al. (1995). Later on also free floating and binary brown dwarf were observed (Rebolo et al. (1995)). More current observations tend to show that brown dwarfs are as common as stars even though their mass fraction is very low compared to the stars (Reid et al. (1999). Much more difficult is the estimation of the binary frequency among brown dwarfs. Reid et al. (2001) found that about 20 percent of the brown dwarf primaries have a companion star in a sample of 20 objects. None of these binary systems have projected separations of more than 10 AU. One should keep in mind that this sample is magnitude-limited rather than volume-limited. Therefore its likely that the binary fraction is overestimated.

Brown dwarfs form in high condensed gas regions as normal stars. But they are ejected out of the dens region before they have accreted enough mass to become stars. Or the dens gas region itself is disrupted by an interaction or instability. In our ensemble 80 percent of the brown dwarfs form in gravitationally unstable circumstellar disks and 20 percent form directly in collapsing fragments in good agreement with results from Bate et al. (2002a). Disks have been shown to become unstable due to rapid accretion(Bonnell (1994), Bonnell and Bate (1994a), Whitworth et al. (1995), Burkert et al. (1997)) and/or tidal perturbations or interaction in the case of stellar encounters (Boffin et al. (1998), Watkins et al. (1998b), Watkins et al. (1998a)). Our simulations clearly show that an dynamically unstable multi object environment is an essential condition for the formation of brown dwarfs. All 63 substellar objects resulting from our ensemble calculation have formed in such chaotic multi systems. This is not surprising because this instability avoids efficiently an extended stable accretion phase which is necessary for the formation of stellar mass objects.

6.8 The Initial Mass Function (IMF)

The initial stellar mass function (IMF) is one of the most important features of the star formation process. A detailed knowledge about this distribution of the resulting stellar masses is a necessary ingredient for understanding many processes involved in star formation. It is controlled by the structure and turbulent dynamic of the interstellar medium, the feedback of new born stars itself and the chemical evolution of the galaxy a whole. Unfortunately, the current theory of star formation remains unable to derive the IMF from first principles. Because the formation of stars is a highly chaotic and indeterministic process it is very unlikely that an analytical formula for the IMF exists. Realistic models need to be found in the framework of a probabilistic theory of the star formation process.

6.8.1 The Observed Initial Mass Function

Gravitationally bound gas spheres as considered to be stars in a classical sense exist only in a finite mass range. Objects with masses less than $0.08 \, M_\odot$ cannot produce the central temperature and density conditions needed for the fusion of hydrogen. These objects are called Brown Dwarfs. A sub fraction of these objects with masses $m > 0.013 \, M_\odot$ is able to burn deuterium for a short time. For an object exceeding the hydrogen burning limit the luminosity increases rapidly with its mass:

$$L \sim m^a \tag{6.4}$$

where L is the luminosity of the star, m its mass and the exponent a ranges from 3 $\ldots 3.5$. Due to the increasing radiation pressure stars with masses greater than about $100 \, M_\odot$ are unstable (Howarth (1994)). Hence, stars are confined to the mass range

$$0.08 \, M_\odot < m < 100 \, M_\odot \tag{6.5}$$

The first trial to determine the IMF was done by Salpeter (1955). He showed that the number $f(m)$ of stars in the mass range m to $m + dm$ can be approximated by a power-law relation

$$f(m)dm \sim m^{-\alpha}dm \tag{6.6}$$

with the index $\alpha \approx 2.35$ for stars in the mass range $0.4 \, M_\odot < m < 10 \, M_\odot$. However, the approximation of the IMF with one single power-law was over simplified. Miller and Scalo (1979) found for the first time a maximum around $m \approx 0.3 \, M_\odot$ and tried to fit the IMF with a log-normal distribution:

$$log_{10} f(log_{10} m) = A - \frac{1}{2(log_{10} \sigma)^2} \Big[log_{10} \Big(\frac{m}{m_0} \Big) \Big]^2 \tag{6.7}$$

Their work has been reinvestigated and improved in a variety of aspects by many authors as described in the review of Scalo (1998). Neglecting the effects of binary and multiple systems, Kroupa et al. (1990) derive the following parameters for the log-normal fit:

$$
\begin{aligned}
m_0 &= 0.23 \\
\sigma &= 0.42 \\
A &= 0.1
\end{aligned}
\tag{6.8}
$$

$$\tag{6.9}$$

Studies before the mid 1990's have not taken into account the contamination of star counts by binary and multiple systems. Binary stars are falsely counted as single stars if they are not resolved by the telescope.

Lada & Lada 2003 extended their survey into the brown dwarf regime down to masses of $m \approx 0.01 \, \mathrm{M_\odot}$ and found a second peak in the IMF around $m = 0.02 \, \mathrm{M_\odot}$ (figure 6.11).

In most of our ensemble runs we evolved the system about 150000 yrs (roughly one free fall time) beyond the formation of the first stellar object respective the first sink particle. In this time $50 \ldots 60$ percent of the total mass has been accreted onto the sink particles. After this epoch the accretion rate significantly fades away and the local mass distribution becomes dominated by the sink particles. In total our 22 collapsing prestellar cores form 127 sink particles. 64 of these objects form stars and 63 do not exceed the hydrogen burning limit ending up as brown dwarfs. 52 objects are bound in binary or multiple systems while only 7 of these bound objects are brown dwarfs. We find a bimodal initial mass distribution with maxima at $m \approx 0.03 \, \mathrm{M_\odot}$ and $m \approx 0.3 \, \mathrm{M_\odot}$ (figure 6.11). The two maxima are the direct consequence of the fact that objects are formed by two distinct mechanisms:

- The formation of objects directly from collapsing fragments contracting beyond the opacity limit. In our simulations these objects nearly always form stars. The mean mass of these objects is $0.47 \, \mathrm{M_\odot}$.

- The formation of objects from a massive accretion disk evolving into an instability. These objects are on average significantly smaller in mass. About 60 percent of these objects do not exceed the hydrogen burning limit. So that we can predict that this formation scenario is typical for the formation of brown dwarfs. The mean mass of these objects is $0.1 \, \mathrm{M_\odot}$. In the ensemble simulations presented here the majority of objects is created by this mechanism.

The initial mass distributions are plotted separately in , figure 6.12 for objects resulting directly from fragments (upper panel) and for objects resulting from disk fragmentation (lower panel). It comes out that the median of this two initial mass distributions differs about one order of magnitude in mass.
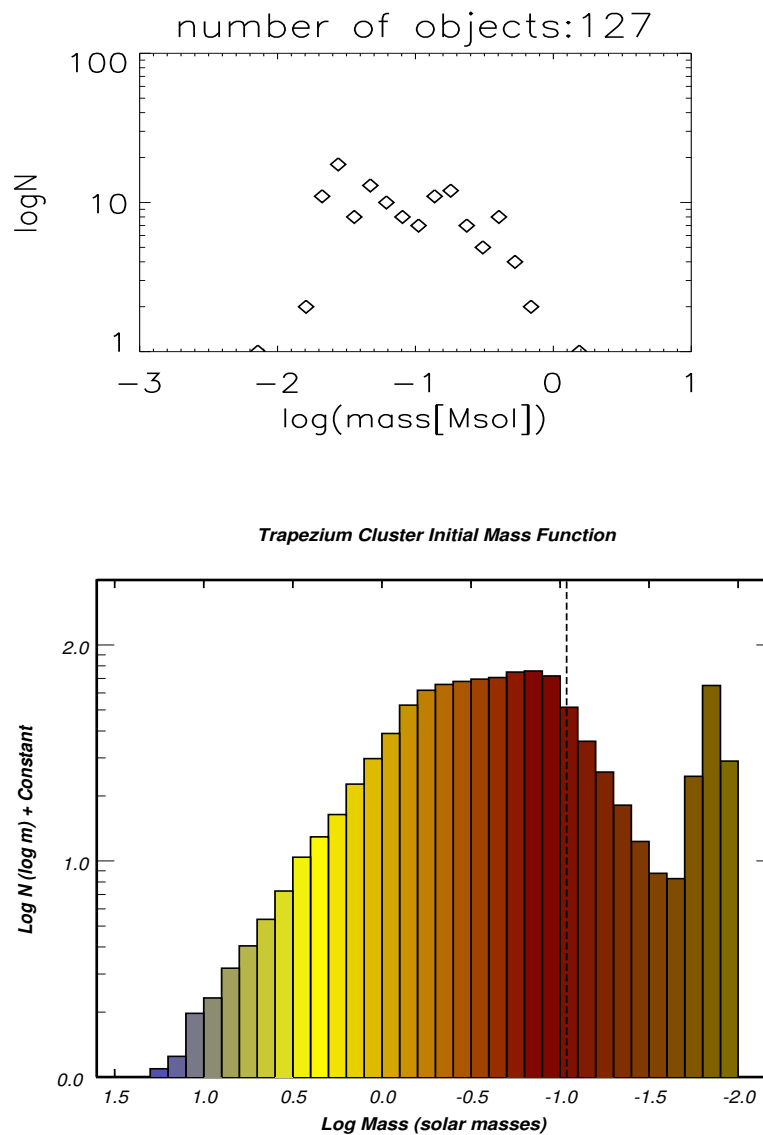
Figure 6.11: **Upper panel: Initial Mass Function (IMF) consisting of all 127 objects created in our ensemble. The low mass end is on the left hand side. Lower panel: IMF taken from Lada & Lada 2003. Be careful with the horizontal axis - the low mass end is to the right!**
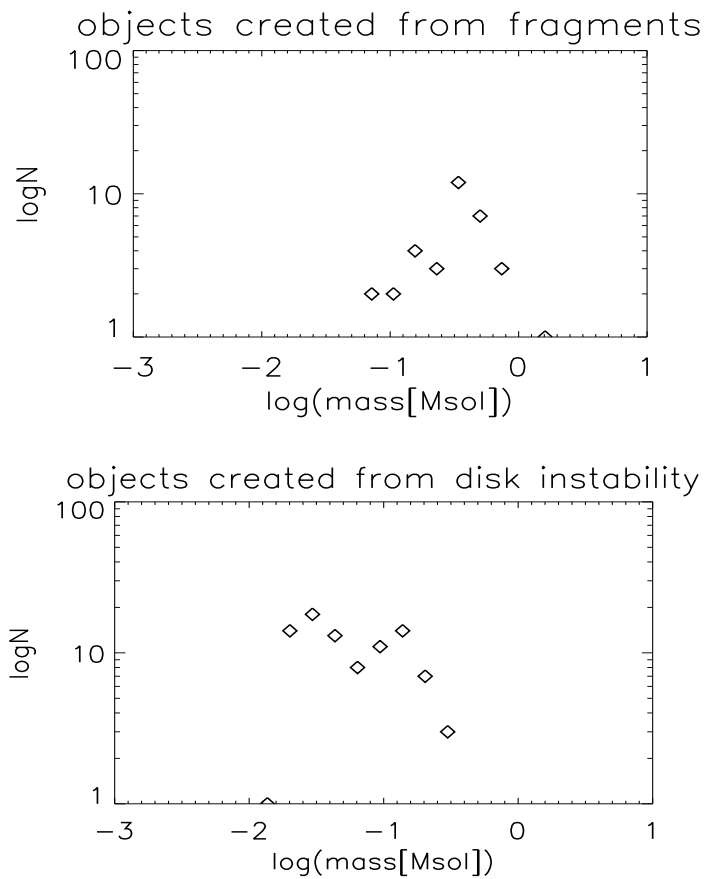
Figure 6.12: **Comparison of the IMF for objects created directly from fragments (upper panel) and objects created from disk instabilities (lower panel).   The majority of the objects emerging from disk instabilities are brown dwarfs**

Chapter 7

Summary and Future Prospects

In this dissertation we discussed the creation of prestellar cores out of turbulent molecular cloud environment, their collapse and fragmentation down to the creation of protostellar objects and the subsequent accretion and interaction history of these objects. We studied the interplay between gravity, thermal pressure and turbulence and showed that a turbulent velocity field can be used in an isothermal model of selfgravitating gas to build up objects which match many of the observed features of prestellar cores. For the subsequent collapse calculations a variable equation of state was used to model the effects of radiative transfer, in particular the heating of the gas beyond the opacity limit. Hydrostatic cores reaching a threshold density were replaced by sink particles taking over the gas and its angular momentum and were able to accrete gas later on. Within the framework of this model we have identified two distinct formation processes of hydrostatic cores. One results in intermediate mass stellar objects, the other leads to low mass stars and brown dwarfs. We sumarize our results in section 7.1 and, starting from the current paradigm, in section 7.2 we suggest further steps to deepen our knowledge of the star formation process.

7.1 Summary

Our simulations show that, in general, the formation of a prestellar core is extremely complex and show a large variety of realizations. The dynamical evolution of a prestellar core into collapse is determined by the interplay between selfgravity, thermal pressure and turbulence. First, turbulence creates several low mass Jeans stable condensations. Even though the condensations are strongly subcritical gravity influences significantly their evolution. They are growing essentially in mass but only weakly in density. Initially separated condensations merge together. At the end a large massive and Jeans unstable condensation has formed. This process of contraction is significantly slower than the isothermal collapse. In some sense it is similar to an adiabatic compression. In both cases there is a pressure supported core like structure on small scales which increases only slowly its density while significantly growing in mass.

- I have developed a method to built up selfconsistent initial conditions for collapse calculations which match most of the common features of prestellar cores. Unlike in the commonly used case of a symmetric initial condition, every core produced by this method is unique in its shape and velocity structure.

113

- It was shown that the turbulent velocity field at its own is not be able to drive the system into a supercritical state. This means, even if the system is strongly subcritical, gravity influences significantly the growth of density structures.

- During the subcritical phase, overdense regions grow strongly in mass and size whereas the density maximum is only weakly enhanced. This explains the extended flat inner part of prestellar cores.

- The collapse starting from a calm Bonnor-Ebert sphere as often used as an initial condition is very unlikely occur in a turbulent molecular cloud. However we find subcritical Bonnor-Ebert spheres with density contrasts ranging from 2 to 6 depending on the initial Mach number but far below the critical density contrast of 13.5.

- The second peak of the initial mass function at the low mass end (e.g. Lada and Lada 2003) can be naturally explained by the two distinct formation mechanisms for hydrostatic cores we have found in our simulations. They can form directly from collapsing fragments resulting in predominantly intermediate mass stellar objects or they form during a disk instability resulting in predominantly low mass stars and brown dwarfs. The second mechanism is responsible for the second peak in the initial mass function around $0.02 M_\odot$

- The period distribution of the resulting binary and triple systems coincides well with the distribution of pre main sequence stars even though we can't resolve the short period end of the distribution.

- The eccentricities of the resulting binary and triple systems are consistent with the distribution found in the solar neighbourhood population.

7.2   Outlook

7.2.1   Memory Effects

Even though our prestellar cores were designed to become supercritical only if the turbulent pressure drops below some critical value, there seems to exist a memory of the initial condition due to the density structures built up before. This can be seen e.g. in the different Bonnor-Ebert sphere density contrasts which depend on the initial Mach number M_0. The history of the turbulent energy content seems to play a role even in the subcritical phase. It would be interesting to analyse how (at the onset of collapse) the specific angular momentum and the density contrast of prestellar cores are affected by the initial amount of turbulent energy and how the turbulent energy is distributed on different scales.

7.2.2   Introduction of Stellar Feedback

As discussed extensively in this dissertation, our selfgravitating gas model in combination with a variable equation of state and the creation of sink particles is able to treat the most dominant physical phenomena of the formation of protostars correctly. However, in the late stages of accretion, feedback processes from the young stellar objects become important, since bipolar outflows, stellar winds and radiation finally will blow away parts of the protostellar

envelope as the star evolves towards the main sequence. This is an important effect deter-
mining the star formation efficiency. Famous and well-studied examples of star formation
regions in which these effects are important are the Trapezium Cluster in Orion (see e.g.
http://antwrp.gsfc.nasa.gov/apod/ap030302.html) and the region around the star η-Carinae,
see figure 1.1. Therefore, to improve the current model of the star formation process feedback
effects and energy input from young stars need to be taken into account.

7.2.3 Radiative Transfer

At the opacity limit the fragmentation starts to be sensitive to radiative transfer. Our vari-
able equation of state is adjusted to the results of a one dimensional radiative transfer model
(Masunaga and Inutsuka (2000)). But it is questionable if this holds also in three dimen-
sions. In three dimensions the cooling process will also depend significantly on the degree of
fragmentation and the shape of the fragments. Filamentary structures will cool much faster
than compact ones. As a result there will be no unique relation between ρ and T as it was
assumed in our calculations. So the implementation of a simple blackbody radiative trans-
fer model in the SPH code would be a great step to check for the variability of the opacity
limit. The point at which the collapsing fragments become opaque fixes the initial mass of
the hydrostatic cores and may also influence the number of objects which are created.

Bibliography

Aikawa, Y., Ohashi, N., Inutsuka, S., Herbst, E., and Takakuwa, S. (2001). Molecular Evolution in Collapsing Prestellar Cores. *Astrophysical Journal*, 552:639–653.

Alves, J. ., Lada, C. J., and Lada, E. A. (2001). Internal structure of a cold dark molecular cloud inferred from the extinction of background starlight. *Nature*, 409:159–161.

André, P., Motte, F., and Bacmann, A. (1999). The Initial Conditions of Star Formation: Observations of Prestellar Cores and Young Protostars. In *Star Formation 1999, Proceedings of Star Formation 1999, held in Nagoya, Japan, June 21 - 25, 1999, Editor: T. Nakamoto, Nobeyama Radio Observatory, p. 145-152*, pages 145–152.

Andre, P. and Montmerle, T. (1994). From T Tauri stars to protostars: Circumstellar material and young stellar objects in the rho Ophiuchi cloud. *Astrophysical Journal*, 420:837–862.

Bacmann, A., Andre, P., Abergel, A., Bernard, J. P., Puget, J. L., Bontemps, S., and Ward-Thompson, D. (1998). An ISOCAM Absorption Study of Dense Cloud Cores. In *ASP Conf. Ser. 132: Star Formation with the Infrared Space Observatory*, pages 307–+.

Barranco, J. A. and Goodman, A. A. (1998). Coherent Dense Cores. I. NH 3 Observations. *Astrophysical Journal*, 504:207–+.

Bate, M. R. (1998a). Collapse of a Molecular Cloud Core to Stellar Densities: The First Three-dimensional Calculations. *Astrophysical Journal Letters*, 508:L95–L98.

Bate, M. R. (1998b). Collapse of a Molecular Cloud Core to Stellar Densities: The First Three-dimensional Calculations. *Astrophysical Journal Letters*, 508:L95–L98.

Bate, M. R., Bonnell, I. A., and Bromm, V. (2002a). The formation mechanism of brown dwarfs. *Monthly Notices of the Royal Astronomical Society*, 332:L65–L68.

Bate, M. R., Bonnell, I. A., and Bromm, V. (2002b). The formation of close binary systems by dynamical interactions and orbital decay. *Monthly Notices of the Royal Astronomical Society*, 336:705–713.

Bate, M. R., Bonnell, I. A., and Price, N. M. (1995). Modelling accretion in protobinary systems. *Monthly Notices of the Royal Astronomical Society*, 277:362–376.

Bate, M. R. and Burkert, A. (1997). Resolution requirements for smoothed particle hydrodynamics calculations with self-gravity. *Monthly Notices of the Royal Astronomical Society*, 288:1060–1072.

Benz, W. (1990). Smooth Particle Hydrodynamics - a Review. In *Numerical Modelling of Nonlinear Stellar Pulsations Problems and Prospects*, pages 269–+.

Benz, W. (1991). An Introduction to Computational Methods in Hydrodynamics. In *LNP Vol. 373: Late Stages of Stellar Evolution. Computational Methods in Astrophysical Hydrodynamics*, pages 259–+.

Bergin, E. A., Plume, R., Williams, J. P., and Myers, P. C. (1999). The Ionization Fraction in Dense Molecular Gas. II. Massive Cores. *Astrophysical Journal*, 512:724–739.

Bodenheimer, P. and Burkert, A. (2001). Formation of Wide Binaries by Fragmentation. In *IAU Symposium*, volume 200, pages 13–+.

Bodenheimer, P., Burkert, A., Klein, R. I., and Boss, A. P. (2000). Multiple Fragmentation of Protostars. *Protostars and Planets IV*, pages 675–+.

Boffin, H. M. J., Watkins, S. J., Bhattal, A. S., Francis, N., and Whitworth, A. P. (1998). Numerical simulations of protostellar encounters - I. Star-disc encounters. *Monthly Notices of the Royal Astronomical Society*, 300:1189–1204.

Bonnell, I. A. (1994). A New Binary Formation Mechanism. *Monthly Notices of the Royal Astronomical Society*, 269:837–848.

Bonnell, I. A. and Bate, M. R. (1994a). Massive Circumbinary Discs and the Formation of Multiple Systems. *Monthly Notices of the Royal Astronomical Society*, 269:L45–L48.

Bonnell, I. A. and Bate, M. R. (1994b). The Formation of Close Binary Systems. *Monthly Notices of the Royal Astronomical Society*, 271:999–1004.

Bonnor, W. B. (1956). Boyle's Law and gravitational instability. *Monthly Notices of the Royal Astronomical Society*, 116:351–+.

Bonnor, W. B. (1957). Jeans' formula for gravitational instability. *Monthly Notices of the Royal Astronomical Society*, 117:104–+.

Bonnor, W. B. (1958). Stability of polytropic gas spheres. *Monthly Notices of the Royal Astronomical Society*, 118:523–+.

Boss, A. P. (1989). Protostellar formation in rotating interstellar clouds. VIII - Inner core formation. *Astrophysical Journal*, 346:336–349.

Burkert, A., Bate, M. R., and Bodenheimer, P. (1997). Protostellar fragmentation in a power-law density distribution. *Monthly Notices of the Royal Astronomical Society*, 289:497–504.

Burkert, A. and Bodenheimer, P. (2000). Turbulent Molecular Cloud Cores: Rotational Properties. *Astrophysical Journal*, 543:822–830.

Burkert, A. and Bodenheimer, P. (2001). Turbulence and Cloud Angular Momentum. In *IAU Symposium*, volume 200, pages 122–+.

Duquennoy, A. and Mayor, M. (1991). Multiplicity among solar-type stars in the solar neighbourhood. II - Distribution of the orbital elements in an unbiased sample. *Astronomy and Astrophysics*, 248:485–524.

Dwek, E. and Scalo, J. M. (1979). Interstellar depletions and the filling factor of the hot interstellar medium. *Astrophysical Journal Letters*, 233:L81–L85.

Evans, N. J. (1999). Physical Conditions in Regions of Star Formation. *Annual Review of Astronomy and Astrophysics*, 37:311–362.

Evrard, A. E. (1988). Beyond N-body - 3D cosmological gas dynamics. *Monthly Notices of the Royal Astronomical Society*, 235:911–934.

Goodman, A. A. and Barranco, J. A. (1994). Velocity Structure in Dense Cores. In *ASP Conf. Ser. 65: Clouds, Cores, and Low Mass Stars*, pages 57–+.

Goodman, A. A., Barranco, J. A., Wilner, D. J., and Heyer, M. H. (1998). Coherence in Dense Cores. II. The Transition to Coherence. *Astrophysical Journal*, 504:223–+.

Goodman, A. A., Benson, P. J., Fuller, G. A., and Myers, P. C. (1993). Dense cores in dark clouds. VIII - Velocity gradients. *Astrophysical Journal*, 406:528–547.

Hennebelle, P., Whitworth, A. P., Gladwin, P. P., and Andre, P. (2002). Protostellar Collapse Induced by Compression. *To be published in MNRAS*.

Hernquist, L. and Katz, N. (1989). TREESPH - A unification of SPH with the hierarchical tree method. *Astrophysical Journal Supplement Series*, 70:419–446.

Howarth, I. (1994). Book Review: The physics of stars / John Wiley , 1993. *Journal of the British Astronomical Association*, 104:140–+.

Huard, T. L., Sandell, G. ., and Weintraub, D. A. (1999). Submillimeter Maps of Bok Globule Cores: Evidence for Multiple Epoch Star Formation. *Astrophysical Journal*, 526:833–844.

Hujeirat, A., Myers, P., Camenzind, M., and Burkert, A. (2000). Collapse of weakly ionized rotating turbulent Cloud Cores. *New Astronomy*, 4:601–613.

Jijina, J., Myers, P. C., and Adams, F. C. (1999). Dense Cores Mapped in Ammonia: A Database. *Astrophysical Journal Supplement Series*, 125:161–236.

Kessel-Deynet, O. and Burkert, A. (2000). Ionizing radiation in smoothed particle hydrodynamics. *Monthly Notices of the Royal Astronomical Society*, 315:713–721.

Klessen, R. S. and Burkert, A. (2000). The Formation of Stellar Clusters: Gaussian Cloud Conditions. I. *Astrophysical Journal Supplement Series*, 128:287–319.

Klessen, R. S. and Burkert, A. (2001a). Fragmentation of Molecular Clouds: The Initial Phase of a Stellar Cluster. In *New horizons of computational science*, pages 239–+.

Klessen, R. S. and Burkert, A. (2001b). The Formation of Stellar Clusters: Gaussian Cloud Conditions. II. *Astrophysical Journal*, 549:386–401.

Klessen, R. S., Heitsch, F., and Mac Low, M. (2000). Gravitational Collapse in Turbulent Molecular Clouds. I. Gasdynamical Turbulence. *Astrophysical Journal*, 535:887–906.

Kolmogorov, A.-N. (1941). On the degeneration of isotropic turbulence in an incompressible viscous liquid. *Dokl. Akad. Nauk SSSR*, 31:538–541.

Kroupa, P., Tout, C. A., and Gilmore, G. (1990). The low-luminosity stellar mass function. *Monthly Notices of the Royal Astronomical Society*, 244:76–85.

Larson, R. B. (1969). Numerical calculations of the dynamics of collapsing proto-star. *Monthly Notices of the Royal Astronomical Society*, 145:271–+.

Larson, R. B. (1981). Turbulence and star formation in molecular clouds. *Monthly Notices of the Royal Astronomical Society*, 194:809–826.

Lattanzio, J. C., Monaghan, J. J., Pongracic, H., and Schwarz, M. P. (1985). Interstellar Cloud Collisions. *Monthly Notices of the Royal Astronomical Society*, 215:125–+.

Low, C. and Lynden-Bell, D. (1976). The minimum Jeans mass or when fragmentation must stop. *Monthly Notices of the Royal Astronomical Society*, 176:367–390.

Mac Low, M., Klessen, R. S., Burkert, A., and Smith, M. D. (1998a). Kinetic Energy Decay Rates of Supersonic and Super-Alfvénic Turbulence in Star-Forming Clouds. *Physical Review Letters*, 80:2754–2757.

Mac Low, M., Klessen, R. S., Burkert, A., and Smith, M. D. (1998b). Kinetic Energy Decay Rates of Supersonic and Super-Alfvénic Turbulence in Star-Forming Clouds. *Physical Review Letters*, 80:2754–2757.

Mac Low, M.-M., Klessen, R., Burkert, A., Smith, M. D., and Kessel, O. (1997). Simulations of MHD Turbulence in Molecular Clouds: Decay Timescales and Spatial Structure. *Bulletin of the American Astronomical Society*, 29:1244–+.

Mac Low, M.-M. and Ossenkopf, V. (2000). Characterizing the structure of interstellar turbulence. *Astronomy and Astrophysics*, 353:339–348.

Masunaga, H. and Inutsuka, S. (1999). Does "tau~1" Terminate the Isothermal Evolution of Collapsing Clouds? *Astrophysical Journal*, 510:822–827.

Masunaga, H. and Inutsuka, S. (2000). A Radiation Hydrodynamic Model for Protostellar Collapse. II. The Second Collapse and the Birth of a Protostar. *Astrophysical Journal*, 531:350–365.

Mathieu, R. D. (1994). Pre-Main-Sequence Binary Stars. *Annual Review of Astronomy and Astrophysics*, 32:465–530.

Miller, G. E. and Scalo, J. M. (1979). The initial mass function and stellar birthrate in the solar neighborhood. *Astrophysical Journal Supplement Series*, 41:513–547.

Monaghan, J. J. and Lattanzio, J. C. (1985). A refined particle method for astrophysical problems. *Astronomy and Astrophysics*, 149:135–143.

Motte, F., Andre, P., and Neri, R. (1998). The initial conditions of star formation in the rho Ophiuchi main cloud: wide-field millimeter continuum mapping. *Astronomy and Astrophysics*, 336:150–172.

Myers, P. C. and Gammie, C. F. (1999a). On the Turbulent Velocity Dispersion in Molecular Clouds. *Astrophysical Journal Letters*, 522:L141–L144.

Myers, P. C. and Gammie, C. F. (1999b). On the Turbulent Velocity Dispersion in Molecular Clouds. *Astrophysical Journal Letters*, 522:L141–LL144.

Nakajima, T., Oppenheimer, B. R., Kulkarni, S. R., Golimowski, D. A., Matthews, K., and Durrance, S. T. (1995). Discovery of a Cool Brown Dwarf. *Nature*, 378:463–+.

Ohashi, N. (1999). Interferometric Imagings of Protostellar and Pre-Protostellar Envelopes. In *Star Formation 1999, Proceedings of Star Formation 1999, held in Nagoya, Japan, June 21 - 25, 1999, Editor: T. Nakamoto, Nobeyama Radio Observatory, p. 129-135*, pages 129–135.

Ossenkopf, V. and Mac Low, M.-M. (2002). Turbulent velocity structure in molecular clouds. *Astronomy and Astrophysics*, 390:307–326.

Padoan, P., Juvela, M., Goodman, A. A., and Nordlund, Å. (2001). The Turbulent Shock Origin of Proto-Stellar Cores. *Astrophysical Journal*, 553:227–234.

Pavlovski, G., Smith, M. D., Mac Low, M., and Rosen, A. (2002). Hydrodynamical simulations of the decay of high-speed molecular turbulence - I. Dense molecular regions. *Monthly Notices of the Royal Astronomical Society*, 337:477–487.

Pringle, J. E., Allen, R. J., and Lubow, S. H. (2001). The formation of molecular clouds. *Monthly Notices of the Royal Astronomical Society*, 327:663–668.

Rebolo, R., Zapatero-Osorio, M. R., and Martin, E. L. (1995). Discovery of a Brown Dwarf in the Pleiades Star Cluster. *Nature*, 377:129–+.

Rees, M. J. (1976). Opacity-limited hierarchical fragmentation and the masses of protostars. *Monthly Notices of the Royal Astronomical Society*, 176:483–486.

Reid, I. N., Gizis, J. E., Kirkpatrick, J. D., and Koerner, D. W. (2001). A Search for L Dwarf Binary Systems. *Astronomical Journal*, 121:489–502.

Reid, I. N., Kirkpatrick, J. D., Liebert, J., Burrows, A., Gizis, J. E., Burgasser, A., Dahn, C. C., Monet, D., Cutri, R., Beichman, C. A., and Skrutskie, M. (1999). L Dwarfs and the Substellar Mass Function. *Astrophysical Journal*, 521:613–629.

Salpeter, E. E. (1955). The Luminosity Function and Stellar Evolution. *Astrophysical Journal*, 121:161–+.

Scalo, J. (1998). The IMF Revisited: A Case for Variations. In *ASP Conf. Ser. 142: The Stellar Initial Mass Function (38th Herstmonceux Conference)*, pages 201–+.

Scalo, J. M. (1986). The stellar initial mass function. *Fundamentals of Cosmic Physics*, 11:1–278.

Shu, F. H. (1977). Self-similar collapse of isothermal spheres and star formation. *Astrophysical Journal*, 214:488–497.

Smith, M. D., Mac Low, M.-M., and Zuev, J. M. (2000). The shock waves in decaying supersonic turbulence. *Astronomy and Astrophysics*, 356:287–300.

Stone, J. M., Ostriker, E. C., and Gammie, C. F. (1998). Dissipation in Compressible Magnetohydrodynamic Turbulence. *Astrophysical Journal Letters*, 508:L99–L102.

Tohline, J. E. (1982). Hydrodynamic collapse. *Fundamentals of Cosmic Physics*, 8:1–81.

Watkins, S. J., Bhattal, A. S., Boffin, H. M. J., Francis, N., and Whitworth, A. P. (1998a). Numerical simulations of protostellar encounters - II. Coplanar disc-disc encounters. *Monthly Notices of the Royal Astronomical Society*, 300:1205–1213.

Watkins, S. J., Bhattal, A. S., Boffin, H. M. J., Francis, N., and Whitworth, A. P. (1998b). Numerical simulations of protostellar encounters - III. Non-coplanar disc-disc encounters. *Monthly Notices of the Royal Astronomical Society*, 300:1214–1224.

Whitworth, A. P., Chapman, S. J., Bhattal, A. S., Disney, M. J., Pongracic, H., and Turner, J. A. (1995). Binary star formation: accretion-induced rotational fragmentation. *Monthly Notices of the Royal Astronomical Society*, 277:727–746.

Williams, J. P., Blitz, L., and McKee, C. F. (2000). The Structure and Evolution of Molecular Clouds: from Clumps to Cores to the IMF. *Protostars and Planets IV*, pages 97–+.

Zucconi, A., Walmsley, C. M., and Galli, D. (2001). The dust temperature distribution in prestellar cores. *Astronomy and Astrophysics*, 376:650–662.

Danksagung

Ich danke...

an erster Stelle dem Betreuer meiner Arbeit, Dr. Andreas Burkert, für seine kreativen Ideen, seine immerwährende Geduld und seine Unterstützung. Es war mir eine Freude, mit ihm zusammenzuarbeiten.

Prof. Dr. Immo Appenzeller und Prof. Dr. Hans-Walter Rix, die mir die Möglichkeit gaben, am MPIA zu promovieren und sich im besonderen der Belange der Promotionsstudenten am Institut angenommen haben.

Prof. Dr. Immo Appenzeller für die Bereitschaft, diese Arbeit zu begutachten.

Dr. Olaf Kessel-Deynet für die Einfürung in SPH.

Dr. Mathew Bate und Dr. Ralf S. Klessen fuer viele Tips und Tricks rund um SPH.

den Mitgliedern der Theoriegruppe für interessante wissenschaftliche Diskussionen.

Martina Kleinheinrich, Michael Bertschik, Andrea Stolte und Angela Hempel für die Unterstützung bei der Korrektur dieser Arbeit.

insbesondere Martina Keinheinrich, die mir die Zeit als Promotionsstudent am MPIA in vielerlei Hinsicht versuesst hat.

Steffi, Thorsten, Markus, Markus, Michael und Sabine für die motivierenden SpatzBiergänge.

Mein allergrößter Dank gilt meiner lieben Frau Martina, meinen Eltern und meinen Freunden mit deren Unterstützung ich es schaffen konnte, meine Doktorarbeit erfolgreich zu vollenden.